

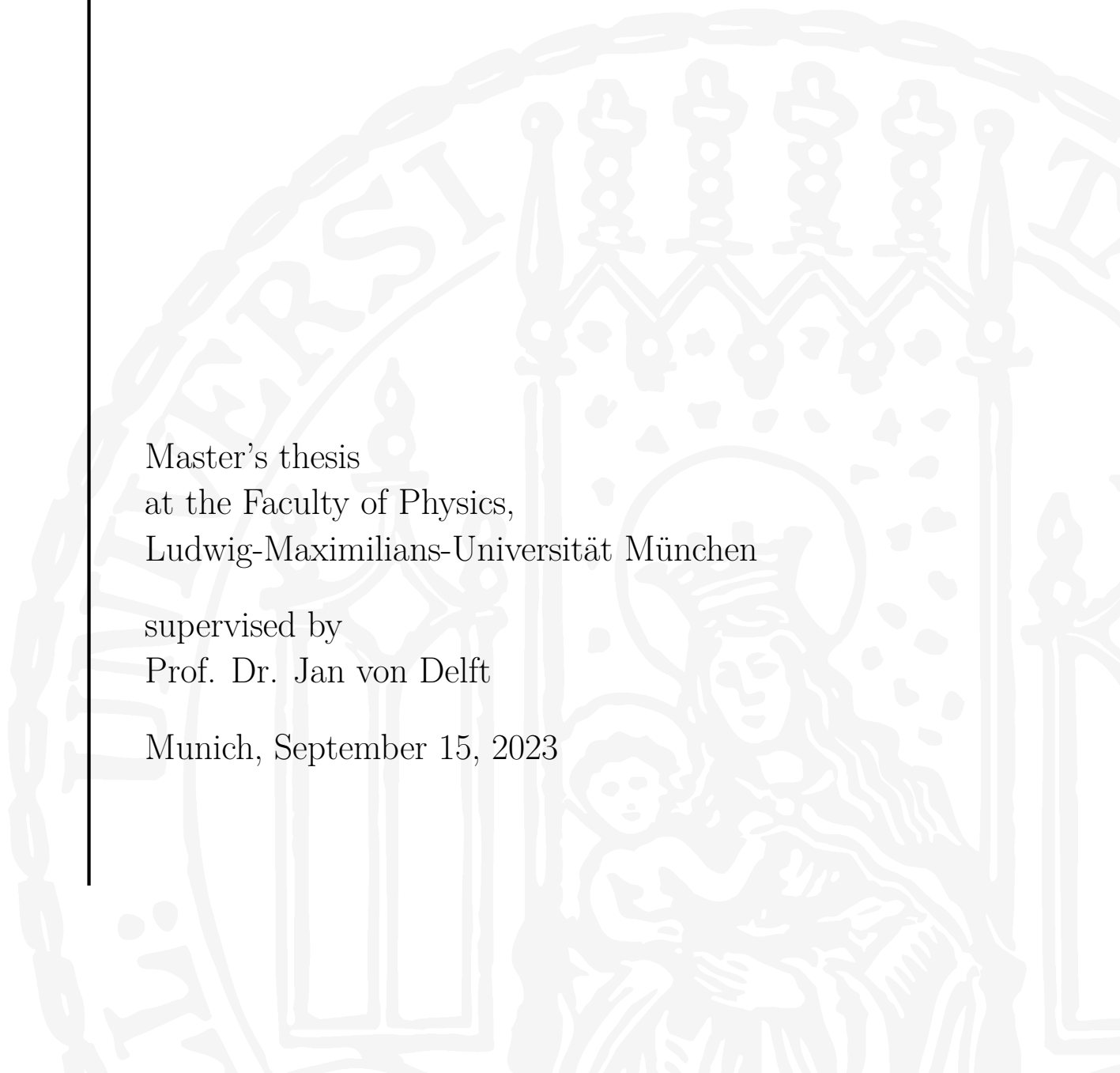
Density Matrix Renormalization Group
Study of
one-dimensional Kondo Lattice Model

Ming Huang

Master's thesis
at the Faculty of Physics,
Ludwig-Maximilians-Universität München

supervised by
Prof. Dr. Jan von Delft

Munich, September 15, 2023



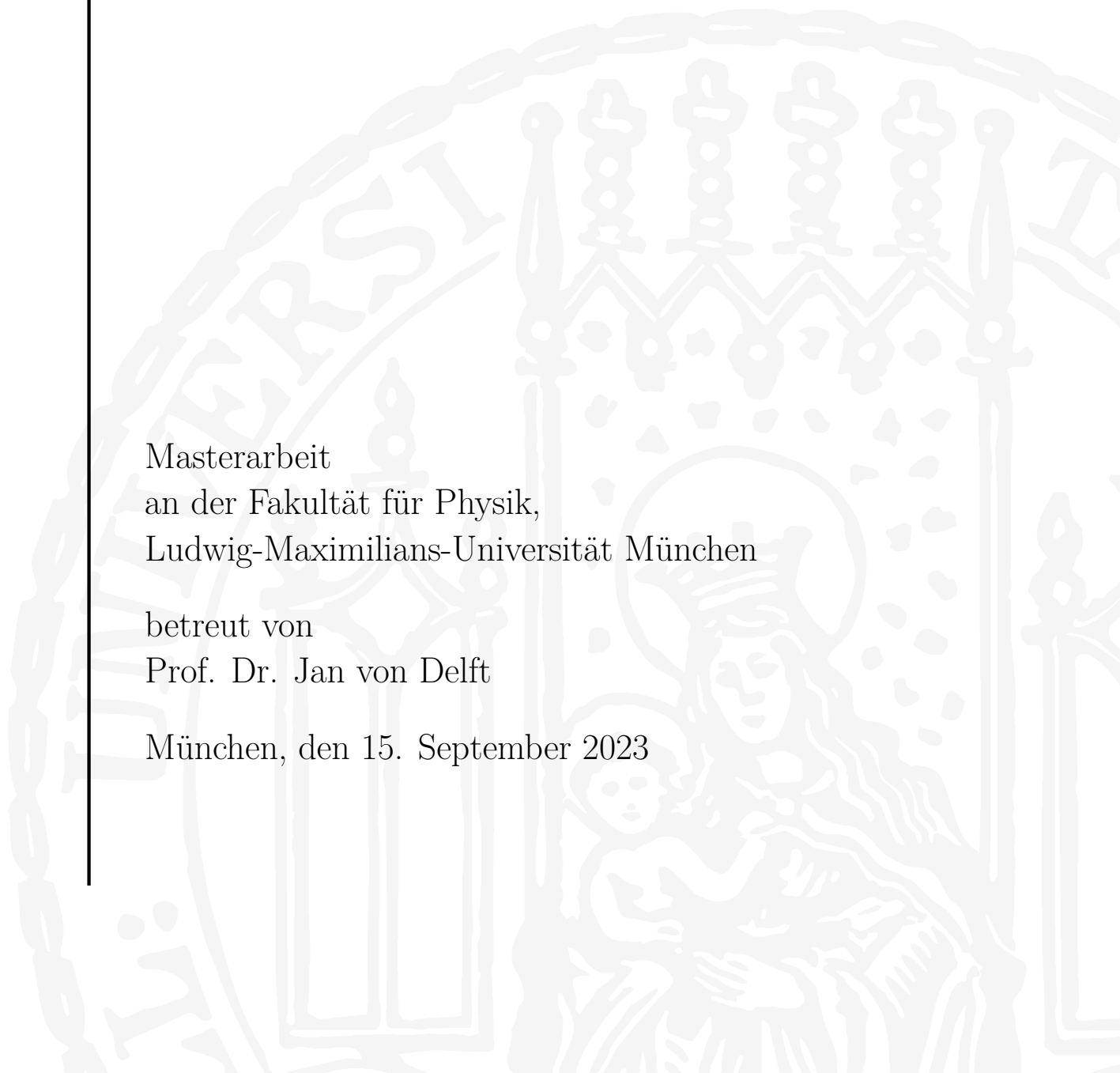
Dichte-Matrix-
Renormierungsgruppenstudie
des eindimensionalen
Kondo-Gittermodells

Ming Huang

Masterarbeit
an der Fakultät für Physik,
Ludwig-Maximilians-Universität München

betreut von
Prof. Dr. Jan von Delft

München, den 15. September 2023



Abstract

The Luttinger's theorem [1, 2], a fundamental principle in condensed matter physics, establishes a link between the electron count and the size of the Fermi surface. While this theorem is crucial for understanding electronic behavior in solid-state materials, its application presents distinctive challenges, especially in one-dimensional systems [3–6]. This thesis focuses on the one-dimensional Kondo lattice model (1D KLM), a system that continuously reveals new and sometimes contradictory phenomena through theoretical and numerical investigations, eluding full comprehension [7–12].

The numerical analyses offer fresh insights into the behavior of the Fermi wave vector within the 1D KLM. The thesis employs Density Matrix Renormalization Group (DMRG) as computational method to unravel these complexities. Through the dissection of correlations into spin and charge sectors, the work sheds light on how the Fermi wave vector and oscillates evolve with changing parameters: the conduction electron density n_c and the Kondo coupling strength J .

We analyze correlation functions, illustrating short-range oscillations with small Fermi wave vectors rapidly decay. By contrast, long-range correlations display distinct behaviors, a significant finding is the validation of a non-trivial transient phase within the 1D KLM phase diagram, where multiple wave vectors coexist. The charge density oscillation validates key parameters, including the Luttinger parameter K_ρ , with a notable inflexion point signalling the transient phases in charge sector and the transition in spin sector.

In the end of thesis, we highlight several potential avenues for future research.

Acknowledgments

I am very grateful to my supervisor, Prof. Dr. Jan von Delft, who introduced me to the world of tensor network algorithms and emphasised that a deep understanding of algorithms is intrinsically linked to a deep grasp of physics. He embodies the ideal mentor, combining enthusiasm with rigorous guidance. Working under his guidance was a truly fulfilling experience.

I am sincerely grateful to Andreas Gleis and Dr. Oleg Yevtushenko for their unwavering support throughout the project. The countless discussions between us not only deepened my understanding of the research but were also a source of inspiration. It has been a great honour to work with them.

I would also like to extend my special thanks to Dr. Andreas Weichselbaum for providing the QSpace tensor library, which played a key role in the success of this project. Additionally, my gratitude goes to Dr. Jeongmin Shim for the valuable discussions and insights.

Finally, I would like to express my sincere gratitude to my family and friends. Their unwavering support has been a source of strength during my long master's studies. Everyone has been challenged over the years, and we find ourselves in a world undergoing profound but invisible change. Despite these trials, I hope that we can all continue to muster the courage and enthusiasm to complete this struggle.

Contents

Contents	v
1 Introduction	1
2 1D Kondo Lattice Model	3
2.1 The Competition between the Kondo effect and the RKKY interaction	4
2.2 Localized Spin Order in 1D KLM	8
2.3 Luttinger's Theorem in 1D KLM	11
3 Method: Density Matrix Renormalization Group	15
3.1 The Important Concepts of Tensor Network	16
3.1.1 Matrix Product State	16
3.1.2 Matrix Product Operator	17
3.1.3 Symmetry	19
3.2 Density Matrix Renormalization Group	20
3.2.1 Controlled Bond Expansion DMRG	22
4 Numerical Results	25
4.1 Correlation Function of 1D KLM	25
4.2 Fermi Wave Vector Behaviors	27
4.2.1 For $n_c = 0.8, N = 200$	29
4.2.2 For $n_c = 0.56, N = 200$	37
4.3 Luttinger Parameter K_ρ	41
4.4 Phenomenological Explanation Of Numerical Results	48
5 Summary and outlook	51
A Appendix 1: Tensor Network Basics and Notations	55
A.1 Tensor Network Basics	55
A.2 DMRG: Iterative ground state search	66

Contents

B Appendix 2: Shrewd Selection	71
C Appendix 3: Extrapolations and Error Analysis	75
Selbständigkeitserklärung	81

Introduction

In the realm of condensed matter physics, understanding the intricate behavior of electrons in strongly correlated systems stands as a central challenge. These systems, where electron-electron interactions wield profound influence, give rise to phenomena that often defy conventional comprehension. Unraveling these enigmas is pivotal in modern condensed matter physics, and efficient computational methods are paramount.

The Luttinger's Theorem [1, 2], a cornerstone of condensed matter physics, links electron count to the Fermi surface's extent. It dictates that, the volume enclosed by the Fermi surface of a system of interacting fermions at zero temperature is independent of the strength of the interaction.

The Luttinger's theorem is most commonly applied to three-dimensional systems. In lower-dimensional systems and strong correlated systems, it may not hold due to the enhanced role of correlations and interactions [13–15].

In some regions of the phase diagram of two or three-dimensional Kondo lattice systems, the behavior is believed to belong to the Fermi liquid phase [16]. In the case of the one-dimensional Kondo lattice model (1D KLM), the Fermi liquid theory is not guaranteed to hold. The prevalence of strong interactions gives rise to distinctive phenomena, notably the emergence of Tomonaga-Luttinger liquid behavior [10].

In 1997, A proof for the Luttinger's Theorem in a 1D system was proposed by Blagoev and Bedell. However, this proof was limited to a simplified model with a linearized dispersion relation, and it neglects the umklapp and backward scattering processes [3].

In the same year, Yamanaka, Oshikawa, and Affleck applied the Lieb-Schultz-Mattis theorem, originally formulated for spin chains, to the 1D Kondo-Heisenberg lattice model with certain symmetries. This model incorporates the Kondo coupling J_K and a direct coupling J_H between localized spins [6]. Through this approach, they demonstrated that the ground state of this model corresponds to a large Fermi momentum $k_F^* \propto n + 1$, where n is the density of conduction electrons, with any $J_K \neq 0$, with or without J_H .

1. Introduction

In 2000, a non-perturbative confirmation of Luttinger’s theorem exists for Kondo lattice models in arbitrary dimensions, as long as they can be described as Fermi liquids [4].

In 2004, Pivovarov and Si demonstrated that a continuous transition from small to large Fermi momentum can occur in one-dimensional Kondo lattice models away from half-filling, particularly with nearest-neighbor (NN) and next-nearest-neighbor (NNN) interactions of local spins [5].

It is showed by Heath and Bedell in 2020, that the applicability of Luttinger’s theorem in a D -dimensional system is directly dependent on the existence of a $(D - 1)$ -dimensional manifold of gapless chiral excitations at the Fermi level, regardless of whether the system exhibits Luttinger or Fermi surfaces [17].

In numerical perspective, several numerical studies of 1D KLM have highlighted the existence of the large Fermi momentum [9–11]. However, there remains some controversy regarding the presence of small or large Fermi momentum. Some numerical results suggest the existence of a small Fermi momentum $k_F \propto n$ in regions of small J_K [7, 8, 12].

Despite numerous analytical and numerical investigations into the Luttinger’s theorem within the context of the 1D KLM, new and often contradictory phenomena continue to emerge. Our understanding remains far from complete.

Chapter. 2 delves into the 1D KLM, providing a comprehensive description. The model’s intricacies arise from the interplay between itinerant conduction electrons and localized spins, resulting in diverse interaction patterns. This competition engenders a rich array of ground states and phenomena, as detailed in the phase diagram of the 1D KLM. The Luttinger’s Theorem and its implications in the realm of 1D KLM form a pivotal component of this chapter.

Chapter. 3 delves into our computational tools, beginning with a primer on tensor networks. We provide a concise guide to the Density Matrix Renormalization Group (DMRG) method, a foundational technique in our project. Additionally, we introduce the controlled bond expansion DMRG, an efficient variant that plays a central role in our endeavors.

In Chapter 4, we present our numerical investigations, meticulously revisit the behaviors of the Fermi wave vector, parsing correlations into spin and charge sectors. The findings compellingly illustrate the evolution of the Fermi wave vector and its associated oscillations as parameters undergo changes. Of particular significance is the evolution as an evidence for the existence of a non-trivial transient phase within the 1D KLM phase diagram, where multiple wave vectors coexist.

1D Kondo Lattice Model

The Kondo model, also known as the Kondo impurity model, explains the behavior of a single magnetic impurity or localized magnetic moment, which interacts antiferromagnetically with conduction electrons in a solid. These localized magnetic moments originate from atoms or ions with unpaired electrons, creating local magnetic moments [18]. The Kondo effect arises from this interaction, causing the screening and quenching of the magnetic moments by conduction electrons at low temperatures and displaying a minimum in electrical resistance [19].

In the 1970s, the discovery of heavy-electron compounds in rare earth and actinide metals prompted proposals by Mott [20] and Doniach [16], suggesting that these systems could be effectively described using a Kondo lattice model. Heavy-electron systems feature ions with f -electrons, such as Ce ions with $4f$ -electrons or U and Np ions with $5f$ -electrons [18]. In the Kondo lattice model, a vast array of local magnetic moments from the f -electrons interacts antiferromagnetically with a conduction electron reservoir, which includes delocalized electrons referred to as c -electrons. The strength of this interaction is typically denoted as J .

The Hamiltonian for the SU(2)-symmetric Kondo lattice model is:

$$\hat{\mathcal{H}} = -t \sum_{\langle i,j \rangle, s} (\hat{c}_{i,s}^\dagger \hat{c}_{j,s} + h.c.) + J \sum_i \hat{\mathbf{S}}_i^f \cdot \hat{\mathbf{S}}_i^c \quad (2.1)$$

Here, the notation $\langle i, j \rangle$ denotes that we are considering nearest-neighbor hopping of conduction electrons, and $t > 0$ represents the hopping energy amplitude. The operators $\hat{c}_{i,s}^\dagger$ and $\hat{c}_{i,s}$ are responsible for creating and annihilating conduction electrons with spin s at site i , respectively.

The conduction electron spin operator is defined as $\hat{\mathbf{S}}_i^c = \frac{1}{2} \sum_{ss'} \hat{c}_{i,s}^\dagger \boldsymbol{\sigma}_{ss'} \hat{c}_{i,s'}$, $\boldsymbol{\sigma} = (\sigma_x \ \sigma_y \ \sigma_z)$ represents the Pauli matrices. The local f -spin operators of f -electrons at site i are represented by $\hat{\mathbf{S}}_i^f$, and they are often associated with the localized magnetic moments. The parameter $J > 0$ indicates an antiferromagnetic on-site coupling.

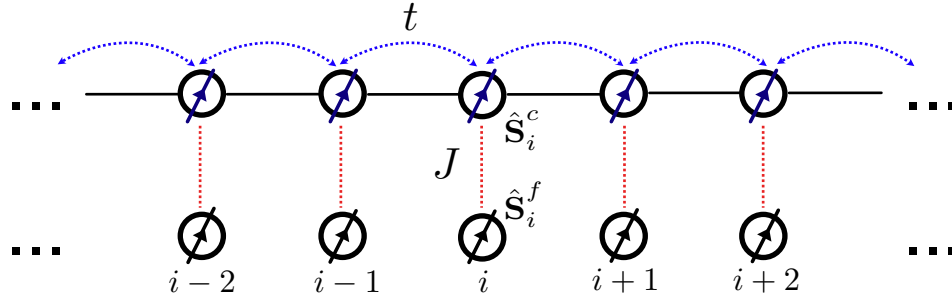


Figure 2.1: The sketch of the one-dimensional Kondo lattice model, it involves a scenario where conduction electrons navigate through a lattice, concurrently engaging in interactions with local spins.

2.1 The Competition between the Kondo effect and the RKKY interaction

The Kondo Effect

The strength of the coupling in the Kondo model, denoted as J , reflects the tendency of localized magnetic moments and conduction electrons to form singlets, when $J > 0$. At low temperatures, these conduction electrons tend to screen the localized moments by forming Kondo singlets, giving rise to the Kondo effect [21].

Numerous methodologies have been developed to tackle the Kondo problem. One notable technique is the Poor Man's Scaling, a perturbative renormalization method introduced by Philip Anderson in 1970 [22].

This practical approach provides an indication of the Kondo temperature T_K , a characteristic energy scale at which the Kondo effect becomes significant and observable. The effective coupling between spin and energy band J_{eff} diverges with the decreasing temperature, and this method breaks down as $J_{eff} \rightarrow \infty$, which is so called strong coupling limit, here the Kondo singlet is formed and the localized moment is screened. Below the Kondo temperature, the resistivity of the material typically exhibits a logarithmic increase with decreasing temperature, which is a hallmark of the Kondo effect.

The Kondo temperature is given by:

$$T_K \propto D e^{-\frac{1}{\rho_0 J}} \quad (2.2)$$

where D is the half-bandwidth of the conduction electrons' energy band, and ρ_0 is the density of state (DoS) of conduction electrons at the Fermi level.

A solution of the Kondo problem was achieved by Kenneth Wilson in 1975 through the application of the numerical renormalization group method [23].

2.1. The Competition between the Kondo effect and the RKKY interaction

In heavy-electron systems featuring a lattice of local moments, the Kondo effect exhibits coherence. In a single impurity, a Kondo singlet scatters electrons without conserving momentum, resulting in a significant increase in resistivity at low temperatures. However, within a lattice possessing translational symmetry, this elastic scattering now conserves momentum, leading to coherent scattering off the Kondo singlets. In the simplest heavy-fermion metals, this phenomenon leads to a notable reduction in resistivity at temperatures below the Kondo temperature [24].

The RKKY Interaction

Amidst the intricate interplay between localized magnetic moments and itinerant conduction electrons, a consequential phenomenon emerges known as the Ruderman-Kittel-Kasuya-Yosida (RKKY) interaction [25].

When a localized moment influences the spins of nearby conduction electrons, these electrons orient themselves in particular directions, giving rise to what is known as Friedel oscillations in the spin density [24]. This phenomenon can be quantified as

$$\langle \mathbf{M}(i) \rangle = -J\chi(i-j)\langle \mathbf{S}_j^f \rangle \quad (2.3)$$

where χ represents the non-local susceptibility of the lattice system.

$$\chi(\mathbf{x}) = \int_{\mathbf{q}} \chi(\mathbf{q}) e^{i\mathbf{q}\cdot\mathbf{x}} \quad (2.4)$$

$$\chi(\mathbf{q}) = 2 \int_{\mathbf{k}} \frac{f(\epsilon_{\mathbf{k}}) - f(\epsilon_{\mathbf{k}+\mathbf{q}})}{\epsilon_{\mathbf{k}+\mathbf{q}} - \epsilon_{\mathbf{k}}} \quad (2.5)$$

here $f(\epsilon_{\mathbf{k}})$ is the Fermi function, $\epsilon_{\mathbf{k}}$ is the energy at momentum \mathbf{k} . This spin alignment extends its influence to neighboring localized moments. As a collective outcome, a compelling stabilization effect materializes—a proclivity for the localized moments to assume antiparallel orientations. This intricate response culminates in a substantial decrease in the system's overall energy:

$$\hat{\mathcal{H}}_{\text{RKKY}} = J_{\text{RKKY}}\chi(i-j)\mathbf{S}_i^f \cdot \mathbf{S}_j^f = -J^2\chi(i-j)\mathbf{S}_i^f \cdot \mathbf{S}_j^f \quad (2.6)$$

In Fermi liquid, due to the shape edge of Fermi surface, Friedel oscillations slowly decays with power law and $q = 2k_F$ oscillation [24] :

$$J_{\text{RKKY}}(r) \sim -J^2\rho_0 \frac{\cos(2k_F r)}{|k_F r|^3} \quad (2.7)$$

where ρ_0 is the conduction electron density of states at Fermi energy level and $r = |i-j|$ is the distance of the two impurities. So the approximate energy scale of the RKKY interactions is

$$E_{\text{RKKY}} \propto J^2\rho_0 \quad (2.8)$$

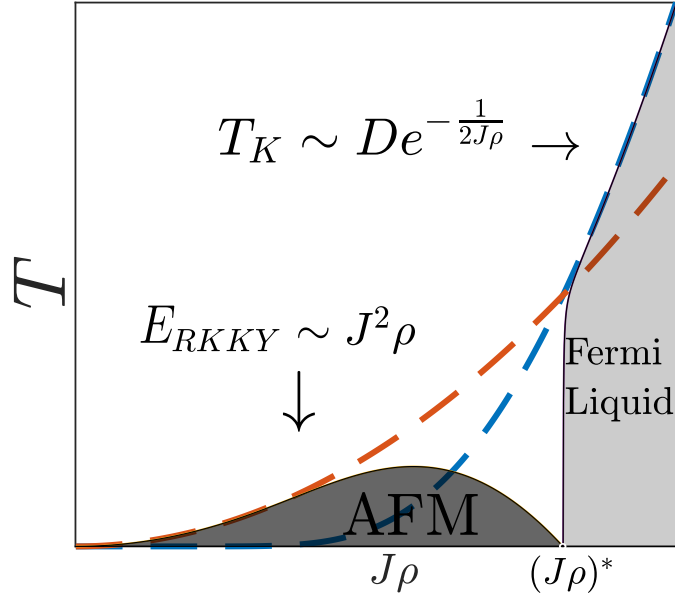


Figure 2.2: Doniach Phase Diagram from Ref. [16, 26]. When the $E_{RKKY} \gg T_K$, the system adopts an AFM state. Conversely, when $T_K \gg E_{RKKY}$, the system embraces a dense Kondo lattice ground state (Fermi Liquid Phase). $(J\rho)^*$ is the quantum critical point.

The Competition between two interactions

Mott and Doniach [16] pointed out that there are two energy scales in the Kondo lattice: the Kondo temperature T_K , (Eq. (2.2)) and the RKKY energy scale E_{RKKY} (Eq. (2.8)).

For small $J\rho$, $E_{RKKY} \gg T_K$, thermal fluctuations disrupt the formation of Kondo singlets, compelling the system to adopt an antiferromagnetic ground state

In an intermediate parameter range, a delicate equilibrium materializes, characterized by a subtle interplay between the RKKY interaction, which promotes magnetic ordering, and the Kondo effect, which leans toward the screening of localized moments. This competition between these interactions can give rise to quantum criticality. Within this regime, the system experiences a continuous phase transition that oscillates between magnetic and non-magnetic phases [16].

In the regime where $J\rho$ takes on large values, the Kondo effect becomes the dominant force, giving rise to the formation of Kondo singlets and the emergence of non-magnetic behavior. Consequently, the system's resistivity follows a logarithmic increase as temperature decreases. This particular phase in the Kondo lattice model is heavy Fermi liquid regime. In this phase, each lattice site resonantly scatters electrons. Importantly, Bloch's theorem ensures

2.1. The Competition between the Kondo effect and the RKKY interaction

that this resonant elastic scattering at every site generates a renormalized f -band, which possesses a width on the order of $\sim T_K$. The scattering at each site acts coherently, setting it apart from the behavior of the Kondo impurity model. As a result, as the heavy-electron metal forms at low temperatures, its resistivity decreases, eventually approaching zero [24].

2.2 Localized Spin Order in 1D KLM

As discussed in Section 2.1, the competition between the Kondo effect and the RKKY interaction plays a crucial role in determining the magnetic behavior of itinerant electrons and localized spins within the Kondo lattice model. This interplay significantly influences the arrangement of phases observed in the model's phase diagram.

The Doniach phase diagram, Fig. 2.2, which evolves based on the system's response to varying Kondo coupling $J\rho$, encompasses a range of distinct phases, including antiferromagnetic and heavy Fermi liquid phases. These phases emerge as a result of the complex competition and cooperation between the Kondo effect and the RKKY interaction.

However, when considering a one-dimensional scenario, the interplay between these two interactions can result in distinct behaviors.

The ground-state phase diagram in this context reveals three distinct phases: the ferromagnetic metallic phase and the paramagnetic metallic phase (characterized as the Heavy Tomonaga-Luttinger Liquid) at partial conduction band filling, and the insulating Kondo spin-liquid phase at half-filling [27].

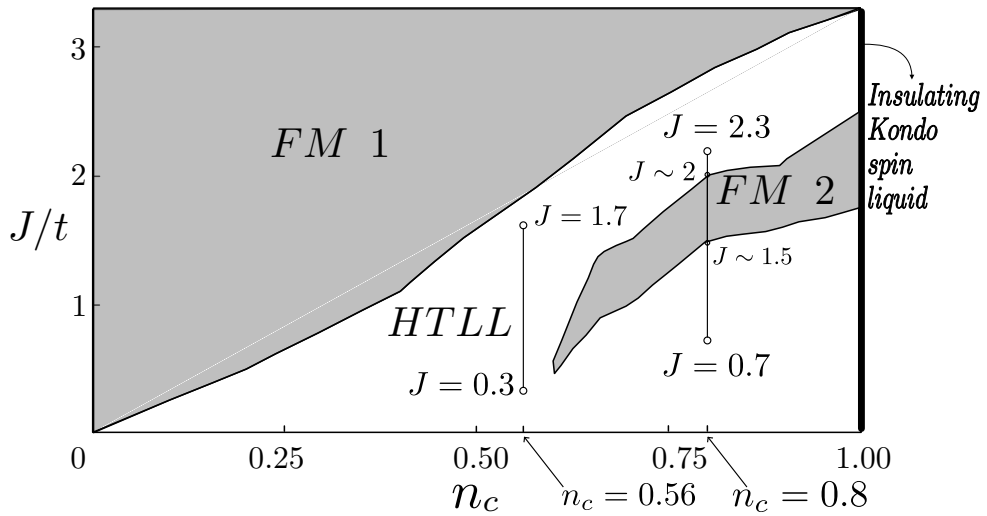


Figure 2.3: Schematic phase diagram of the 1D KLM from Ref. [28], n_c is the conduction electron density, J/t is the Kondo coupling over hopping energy. *FM1* and *FM2* denote the ferromagnetic states, and *HTLL* denotes the Luttinger liquid states. The two vertical lines [$n_c = 0.8, 0.7 \leq J \leq 2.3$] and [$n_c = 0.56, 0.3 \leq J \leq 1.7$] denote the parameters chosen for this project. The boundaries of *FM2*-phase and *HTLL*-phase at $n_c = 0.8$ are around $J = 1.5$ and $J = 2$.

In situations where the conduction-band filling is incommensurate, the emergence of a ferromagnetic phase can be attributed to the phenomenon known as the double exchange interaction.

The concept of double exchange was originally introduced by Zener [29] as an explanation for ferromagnetic (FM) ordering observed in mixed-valency manganites. The fundamental condition for a system to exhibit double exchange ordering is that the number of electrons must be fewer than the number of localized spins ($N > N_c$), and the presence of non-vanishing electron hopping is essential.

Considering the case of infinitely strong coupling ($J = \infty$), each electron forms a perfect localized spin singlet (or triplet for $J < 0$) with the localized spin at the same site. The remaining unpaired localized spins ($N - N_c$) remain free. Upon activating conduction electron hopping, electrons gain energy by moving to unoccupied sites. This energy gain arises from both the screening of unpaired localized spins and an increase in kinetic energy.

Electrons with specific spin orientations tend to maintain this orientation as they hop, a phenomenon referred to as coherent hopping. This behavior promotes the alignment of the localized spins with the spins of the hopping electrons [30, 31].

This alignment mechanism is termed "double-exchange" and is propelled by both the kinetic energy of conduction electrons and the diagonal component of the on-site interaction between electrons and localized spins. Double-exchange consistently results in ferromagnetic behavior and becomes more pronounced at stronger couplings.

This principle of FM behavior serves as the foundational basis for the rigorously established FM phase within the 1D Kondo lattice model by Sigrist et al. [32, 33].

Utilizing bosonization techniques, the mechanisms governing the ordering of localized spins in this context can be analytically unraveled [27, 34].

It is worth emphasizing that within the realm of the 1D Kondo lattice model, the conduction band can be effectively treated using bosonization techniques. However, the application of bosonization to localized spins is not straightforward due to their absence of a Fermi velocity. In tackling the treatment of localized spins, a direct strategy involves implementing a unitary transformation. This transformation shifts the system into a state basis where the spin degrees of freedom of conduction electrons are directly linked to the localized spins. This approach facilitates an investigation into how the ordering of electrons impacts the behavior of localized spins.

In the resulting effective Hamiltonian, a significant new term arises, representing a nonperturbative effective interaction among the localized spins. This term yields a length scale known as α , originating from bosonization, and it signifies the minimum wavelength for density fluctuations complying with bosonic commutation relations. The appearance of Kondo singlets is indirectly inferred from the implications of this effective length scale.

The domains of localized spins exhibiting double-exchange ordering gradually disintegrate as the coupling to the conduction electrons weakens. In the

2. 1D Kondo Lattice Model

regime of weak coupling strength J , the system transitions into a paramagnetic metallic phase. This phase can be characterized as a RKKY-like liquid, influenced by the RKKY interaction.

In 2019 and 2020, Tsvetlik and Yevtushenko have developed a unified theory specifically tailored for the 1D isotropic KLM, assuming a scenario with a small Kondo coupling ($|J| \ll E_F$) [35, 36]. Their work has illuminated the governing factors in the physics of the Kondo lattice, emphasizing the dominant role of the RKKY indirect spin interaction while the Kondo physics becomes less influential and all properties are determined by the patterns of spin ordering.

In their investigation, three distinct phases have been identified:

(1) Insulating Phase: This phase emerges at special commensurate band fillings. In this phase, the spin configurations remain collinear;

(2) Spinful Interacting Metals (Collinear Metal Phase): These phases are present in the vicinity of commensurate band fillings. Similar to the insulating phase, the spin configurations are collinear. However, electron-spin interactions can transform this phase into heavy Tomonaga-Luttinger liquids;

(3) Helical Metallic Phase with $4k_F$ Charge-Density Wave: This phase occurs at generic band fillings. In this intriguing phase, the local spins exhibit slow spatial and temporal spirals. This leads to the formation of a local helical gap.

Multiple numerical methods were employed in calculation of 1D KLM phase diagram:

The quantum Monte Carlo method (1993, Troyer and Würtz) [37], the exact diagonalization (1993, Tsunetsugu, Sigrist and Ueda) [38], the DMRG and infinite size DMRG (1995, Moukouri and Caron, 1997, Caprara and Rosengren) [39, 40] respectively verified the boundary of the first ferromagnetic phase and the paramagnetic phase.

Importantly, it's worth noting that the appearance of the second ferromagnetic region in Fig. 2.3 is not predicted by the bosonization method.

The discovery of this second ferromagnetic region was made through the application of the non-Abelian density matrix renormalization group method. McCulloch, Juozapavicius, Rosengren, and Gulacsi employed this method to directly measure the magnetization of the ground state, revealing the existence of the second FM region in the 1D KLM phase diagram [8]. Their hypothesis is grounded in the idea that, for a majority of dopings, this FM2 region serves as a boundary between the domains of large and small Fermi momenta. This hypothesis is based on the understanding that Fermi points are unlikely to remain unchanged during a phase transition.

The FM2 region is numerically checked by further work and widely accepted and quoted [7, 28, 41, 42].

2.3 Luttinger's Theorem in 1D KLM

Luttinger's theorem [1, 2] states that, the volume enclosed by a material's Fermi surface is directly proportional to the particle density. Even when electron-electron interactions are considered, the size and shape of the Fermi surface remain constant as long as the total electron density is conserved. The Luttinger's theorem is most commonly applied to Fermi liquid system. In lower-dimensional systems and strong correlated systems, it may not hold due to the enhanced role of correlations and interactions [13–15].

The Kondo lattice model can be seen as an extension of the periodic Anderson model, achieved through the Schrieffer-Wolff transformation [43, 44] with an extended Kondo limit:

$$\epsilon_f \equiv -\frac{U}{2}, U \rightarrow \infty, V \rightarrow \infty \text{ with } \frac{V^2}{U} \rightarrow \text{const.} \quad (2.9)$$

ϵ_f is the localized electron energy, U is the on-site Coulomb repulsion and V gives the hybridization of conduction electron and spin. In this transform can obtain any finite Kondo coupling:

$$J \sim \mathcal{O}\left(\frac{V^2}{U}\right) \quad (2.10)$$

When U surpasses a certain threshold, the Fermi surface volume \mathcal{V}_{FS} will extend from only include conduction electrons to encompass localized electrons and their associated local spins [13, 45]:

$$2 \frac{\mathcal{V}_{FS}^S}{(2\pi)^3} = n_e \rightarrow 2 \frac{\mathcal{V}_{FS}^L}{(2\pi)^3} = n_e + n_{spins} \quad (2.11)$$

The Fermi wave vector defines the boundary in momentum space that separates occupied from unoccupied electron energy levels in a material's electronic band structure, crucial for a material's electrical and thermal properties.

In strongly correlated electron systems, Fermi wave vectors offer insights into correlation effects like the Mott transition [46]. Materials with Fermi surface instabilities can exhibit unconventional behaviors, like high-temperature superconductivity [47], making the accurate determination of Fermi wave vectors vital for identifying and characterizing these unique material states.

Furthermore, the changes in the Fermi wave vector, known as Fermi surface reconstruction, can unveil different electronic orders or phases like charge density waves (CDW) or spin density waves (SDW) [48, 49]. This phenomenon, often linked to unconventional quantum criticality, has been experimentally observed in heavy Fermion compounds such as $\text{CeCu}_{6-x}\text{Au}_x$ and YbRh_2Si_2 [50, 51].

In certain regions of the phase diagram for two or three-dimensional Kondo lattice systems, it is believed that the system's behavior can be described by

2. 1D Kondo Lattice Model

the Fermi liquid phase [16] (see Fig. 2.2). By applying the real-space dynamical mean-field theory to the Kondo lattice model on a square lattice, the existence of metallic SDW and Fermi surface reconstruction has been demonstrated [52].

In the case of the one-dimensional Kondo lattice model (1D KLM), the Fermi liquid theory is not guaranteed to hold. The prevalence of strong interactions gives rise to distinctive phenomena, notably the emergence of Tomonaga-Luttinger liquid behavior [10]. In contrast to the non-interacting-quasiparticles found in Fermi liquids, collective excitations in Luttinger liquids manifest as density waves, which exhibit an entirely different nature.

A proof of the Luttinger Theorem in a 1D system was proposed by Blagoev and Bedell. However, it's important to note that this proof was confined to a simplified model with a linearized dispersion relation, and it did not consider umklapp and backward scattering processes [3].

Furthermore, utilizing the bosonization method, it has been demonstrated that the Kondo chain, when away from half-filling, exhibits a spin gap when an additional direct Heisenberg coupling between localized spins is introduced [53].

In 1997, Yamanaka, Oshikawa, and Affleck applied the Lieb-Schultz-Mattis theorem (LSM theorem) to the 1D Kondo-Heisenberg lattice model [6]. The LSM theorem, originally developed for spin chains, establishes that a spin system characterized by specific symmetries, including translation and spin rotation symmetry, and having half-integer spin per unit cell, cannot have a gapped symmetric ground state without the presence of fractionalized excitations. [54].

In a chain of length L system with periodic boundary conditions, the Hamiltonian is the Hamiltonian of KLM with additional Heisenberg interaction term:

$$\hat{H} = -t \sum_{i,s} (\hat{c}_{i,s}^\dagger \hat{c}_{i+1,s} + h.c.) + J \sum_i \hat{\mathbf{S}}_i^f \cdot \hat{\mathbf{S}}_i^c + J_H \sum_i \hat{\mathbf{S}}_i^f \cdot \hat{\mathbf{S}}_i^f \quad (2.12)$$

J_H is the Heisenberg interaction between localized spins. There is at least one low-energy state $|\psi_1\rangle$ above the ground state $|\psi_0\rangle$ with $\Delta E \sim \mathcal{O}(1/L)$ by LSM theorem. Define a "twist" operator \hat{U}

$$\hat{U}_\pm \equiv \exp[2\pi i \sum_j \frac{J}{L} (n_{\pm,j} \pm S_j^{f,z})] \quad (2.13)$$

where n is the conduction electron number per site and \pm represents the electron spin.

The "twist" operator satisfies $\hat{U}_\pm |\psi_0\rangle = |\psi_1\rangle$. When interaction terms involve only the local density and are invariant under the transformation by \hat{U} , and with the condition that the Hamiltonian is invariant under parity or time reversal, $\langle \psi_1 | \hat{H} | \psi_1 \rangle - \langle \psi_0 | \hat{H} | \psi_0 \rangle \sim \mathcal{O}(1/L)$.

This indicates that the energy difference becomes increasingly negligible as the system size grows larger.

Then we can use a translation operator \hat{T} to prove $|\psi_1\rangle$ is orthogonal to $|\psi_0\rangle$. The operator \hat{T} is related to the total crystal momentum \mathbf{P} by $\hat{T} = e^{i\mathbf{P}}$ (set lattice space equal to 1) and commute to \hat{H} according to the translation invariant of system, which means $|\psi_0\rangle$ is an eigenstate of \hat{T} .

We obtain the

$$\hat{U}^{-1}\hat{T}\hat{U} = \hat{T}e^{\pi i(n \pm 2m + 1)} \quad (2.14)$$

where m is the magnetization per unit cell including both the conduction electrons and the localized spin. It is easy to prove that $|\psi_1\rangle$ is another eigenstate of \hat{T} .

The Eq. (2.14) means that the low-energy state $|\psi_1\rangle = \hat{U}_\pm|\psi_0\rangle$ has crystal momentum $\pi(n \pm 2m + 1)$ relative to ground state $|\psi_0\rangle$. In particular, the low-energy state has the momentum $\pm\pi(n + 1)$ for zero magnetic field, which consistent with large Fermi wave vector.

Their analysis revealed that the ground state of this model corresponds to a large Fermi momentum $k_F^* \propto n + 1$. This result holds true for any nonvanishing Kondo coupling J , regardless whether the direct Heisenberg exchange J_H is present.

However, it's important to note that this proof relies on certain assumptions, including system translational invariance and the conservation of total particle number and parity or time reversal symmetry. Therefore, it may not be valid in cases where conditions like charge density waves (CDW) are present, as is the situation in this project.

In 2000, A non-perturbative confirmation of Luttinger's theorem exists for Kondo lattice models in arbitrary dimensions, as long as they can be described as Fermi liquids [4].

In 2004, Pivovarov and Si demonstrated that a continuous transition from small to large Fermi momentum can occur in 1D KLM away from half-filling, particularly with nearest-neighbor (NN) and next-nearest-neighbor (NNN) interactions of local spins [5].

It is showed by Heath and Bedell in 2020, that the applicability of Luttinger's theorem in a D -dimensional system is directly dependent on the existence of a $(D - 1)$ -dimensional manifold of gapless chiral excitations at the Fermi level, regardless of whether the system exhibits Luttinger or Fermi surfaces [17].

Several numerical studies have highlighted the existence of the large Fermi momentum [9–11]. However, there remains some controversy regarding the presence of small or large Fermi momentum. Some numerical results suggest the existence of a small Fermi momentum $k_F \propto n$ in regions of small J [7, 8, 12].

Another recent DMRG study in a variant of 1D KLM are done by Nikolaenko and Zhang in 2023, the system includes a $t - J$ model with onsite Kondo coupling J and nearest neighbour Kondo interaction J_{cs} . In this paper, the authors confirm the presence of a large Fermi wave vector in the case of a large

2. 1D Kondo Lattice Model

Kondo coupling J , which corresponds to the expected conventional Luttinger liquid phase. On the other hand, they observe a small Fermi wave vector when the Kondo coupling J is negative, indicating the presence of a fractional Luttinger liquid phase. Notably, this fractional Luttinger liquid phase becomes unstable and undergoes a transition to a spin-gapped Luther-Emery liquid phase when the Kondo coupling J is slightly positive [55].

While the models explored in the aforementioned paper may not be identical to the one under examination in our study, their findings offer valuable insights that can enhance our understanding.

From a more superficial perspective, when the Kondo coupling is extremely small, the system can be equated to a free electron gas. In this scenario, the Fermi wave vector is naturally related only to the conduction electrons, yielding $k_F \propto n_c$. As the Kondo coupling approaches infinity, the conduction electrons and the local spins form Kondo singlets. The density of unpaired localized spins, which behave as free holes, is $1 - n_c$, leading to the emergence of a large Fermi wave vector. In between, the transition between small and large Fermi wave vectors occurs, but the precise mechanisms behind this transition in the original 1D KLM remain an open area of investigation.

Method: Density Matrix Renormalization Group

Density Matrix Renormalization Group (DMRG) is a powerful numerical technique widely used in condensed matter physics and quantum chemistry to investigate strongly correlated quantum systems. It was first introduced by Steven R. White in 1992, primarily for one-dimensional lattice systems [56, 57].

DMRG is designed to efficiently determine the ground state and low-lying excited states of complex quantum many-body systems. While it initially gained prominence in one-dimensional systems like spin chains and quantum wires, it has since been adapted for use in higher dimensions, making it a versatile tool in the study of various quantum systems.

This technique has been also progressively expanded to investigate dynamic properties [58], finite-temperature phenomena [59], and non-equilibrium time-evolutions [60] over subsequent years.

DMRG stands as a potent numerical strategy designed to dissect strongly correlated systems, particularly in one-dimensional contexts. Its effectiveness in capturing extensive-range correlations and adeptly navigating entanglement complexities has led to its application across a spectrum of systems, ranging from spin chains to Hubbard models. Notably, DMRG has significantly informed the analysis of the Kondo lattice model, as evidenced by the numerous references in this paper.

In this study, DMRG is employed due to its efficiency in computing ground states, correlations, and expectation values. It operates through an iterative optimization of the quantum state representation using a variational approach, retaining crucial information while discarding less pertinent details. This iterative search mechanism enables the determination of the ground state for a given Hamiltonian.

The basic concepts and notations of tensor network can be found in Appendix A.

This chapter will start with the important concepts of tensor network: MPS and MPO, provide a concise introduction to DMRG technique, followed by an exploration of its more efficient variant we used in this project: Controlled Bond Expansion DMRG [61].

3.1 The Important Concepts of Tensor Network

3.1.1 Matrix Product State

The Matrix Product State (MPS) is a tensor network representation primarily employed to describe quantum states, especially in one-dimensional systems [62–64].

In the Matrix Product State (MPS) framework, a quantum state is encoded as a series of tensors, with each tensor describing the correlations between adjacent sites in the system.

Consider a quantum state denoted as $|\Psi\rangle$ residing in a one-dimensional system with \mathcal{L} sites, Each of these lattice sites accommodates a local state space of dimension d . The quantum state can be expanded using the Fock space basis $|\sigma_1\rangle, |\sigma_2\rangle, \dots, |\sigma_{\mathcal{L}}\rangle$ as follows:

$$|\psi\rangle = \sum_{\sigma_1, \sigma_2, \dots, \sigma_{\mathcal{L}}} \Psi^{\sigma_1 \sigma_2 \dots \sigma_{\mathcal{L}}} |\sigma_1\rangle |\sigma_2\rangle \dots |\sigma_{\mathcal{L}}\rangle \quad (3.1)$$

The wave function $\Psi^{\sigma_1 \sigma_2 \dots \sigma_{\mathcal{L}}}$ can be conceived as a tensor of rank \mathcal{L} . Tensor network techniques are precisely the methodologies employed to construct and analyze this tensor. The MPS involves breaking down the substantial tensor into a product ensemble of rank-3 tensors, as follows:

$$\Psi^{\sigma_1 \sigma_2 \dots \sigma_{\mathcal{L}}} = \sum_{\alpha, \beta, \dots, \mu} A_{\alpha}^{\sigma_1} A_{\alpha\beta}^{\sigma_2} A_{\beta\gamma}^{\sigma_3} \dots A_{\mu}^{\sigma_{\mathcal{L}}} \quad (3.2)$$

To enhance clarity, we designate all unphysical bonds as lower indices.

However, representing such a lengthy mathematical formula isn't practical and lacks sufficient informativeness. Hence, we resort to the diagrammatic notation from Ref. [65].

In diagram form, the aforementioned formula can be restated as depicted in Fig. 3.1.

This construction creates an exact MPS representation of the wave function without any approximation. However, it's evident that the dimension of the virtual bond at site i grows exponentially as d^i . To manage this, additional strategies are required to limit the bond dimension. Our current approach involves the Singular Value Decomposition (SVD), which has been extensively used in data compression, as discussed in the Appendix (Sec. A.1).

Consequently, the SVD operation can be sequentially executed from left to right (or right to left), yielding tensors that are left-normalized (or right-normalized), thereby ensuring that the bond dimensions remain within the limit of D .

$$\Psi^{\sigma_1 \sigma_2 \dots \sigma_{\mathcal{L}}} = \begin{array}{cccccccc} & A & & A & & A & & A & & A & & A & & A \\ & \circ & \xrightarrow{\alpha} & \circ & \xrightarrow{\beta} & \circ & \xrightarrow{\gamma} & \circ & \xrightarrow{\dots} & \circ & \xrightarrow{\mu} & \circ & & \circ \\ \uparrow & & & \uparrow \\ \sigma_1 & & & \sigma_2 & & \sigma_3 & & \dots & & \dots & & \sigma_{\mathcal{L}} & & \end{array}$$

Figure 3.1: Matrix Product State (MPS) is a representation of many-body wave functions, where each element of the tensor Ψ is obtained through a sequence of matrix products.

The matrix products in tensor network have gauge freedom, which means any matrix product can be expressed in infinitely many ways without changing the product:

$$MM' = M(UU^{-1})M' = \tilde{M}\tilde{M}' \quad (3.3)$$

Gauge freedom can be exploited to reshape MPSs into particularly convenient, canonical forms: Left-canonical, right-canonical, site-canonical and bond-canonical.

3.1.2 Matrix Product Operator

MPO representation:

Any operator for a Hilbert space of \mathcal{L} sites can be expressed in the form:

$$\hat{O} = |\vec{\sigma}'\rangle O_{\vec{\sigma}}^{\vec{\sigma}'} \langle \vec{\sigma} | \quad (3.4)$$

Applying the same concept used for the MPS, operators can also be represented in a matrix product form:

$$\begin{aligned} \hat{O} &= |\vec{\sigma}'\rangle [W_1]_{\mu\sigma_1}^{1\sigma'_1} [W_2]_{\nu\sigma_2}^{\mu\sigma'_1} \dots [W_{\mathcal{L}}]_{1\sigma_{\mathcal{L}}}^{\lambda\sigma'_{\mathcal{L}}} \langle \vec{\sigma} | \\ &= |\vec{\sigma}'\rangle \left\{ \prod_{l=1}^{\mathcal{L}} W_l \right\}_{\vec{\sigma}}^{\vec{\sigma}'} \langle \vec{\sigma} | \end{aligned} \quad (3.5)$$

This can be systematically achieved through a sequence of QR decomposition:

When singular values are not a concern, a matrix $M \in \text{mat}(D, D'; \mathbb{C})$ can undergo a "full QR decomposition" denoted as $M = QR$. In this setup, $Q \in \text{mat}(D, D; \mathbb{C})$ is a unitary matrix, and $R \in \text{mat}(D, D'; \mathbb{C})$ is an upper triangular matrix. It's worth noting that $R_{\alpha\beta}$ is zero when $\alpha > \beta$.

In this context, each W_i takes the form of a rank-4 tensor. Interestingly, a vast majority of significant physical operators (such as the Hamiltonian and its constituents) can be precisely depicted as a matrix product operator (MPO) featuring a modest dimension D_W , which signifies the dimension of W_i . This attribute renders the MPO framework exceptionally valuable for a wide range of applications.

3. Method: Density Matrix Renormalization Group

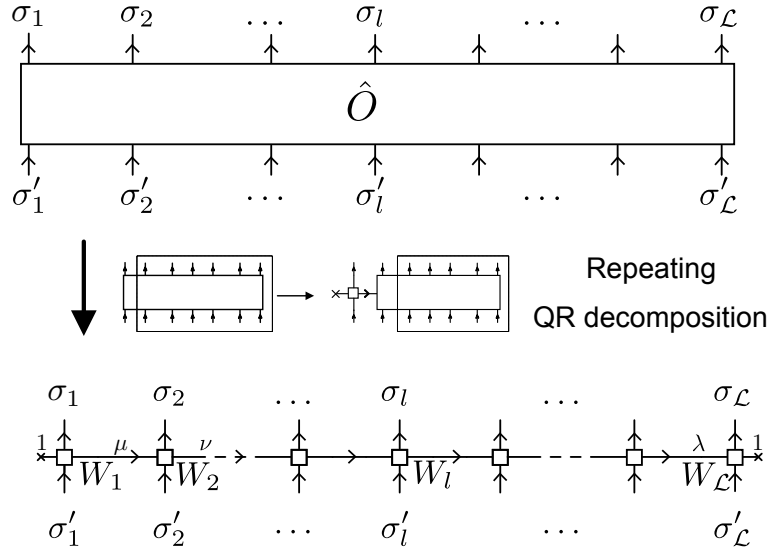


Figure 3.2: From operator to MPO, by applying QR decomposition iteratively.

Observables

MPOs proficiently encapsulate the inherent local interactions and correlations of a specific operator. Each tensor within an MPO corresponds to a localized operator that affects either an individual site or a neighboring pair of sites. By leveraging the inherent multiplication and addition rules of MPOs, it becomes possible to compute correlation observables, illustrated by expressions like $\langle \psi | \hat{O}_i \hat{O}_j | \psi \rangle$.

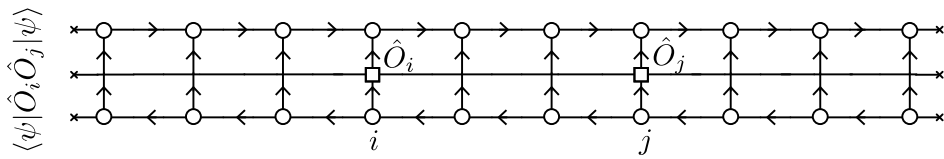


Figure 3.3: The diagrammatic representation of Correlation function $\langle \psi | \hat{O}_i \hat{O}_j | \psi \rangle$.

Construct the MPOs for 1D KLM

The Hamiltonian of the 1D Kondo lattice model as given in Eq. (2.1) can be expressed in the MPO representation through a straightforward construction [63] and [66].

$$\begin{aligned}
 \hat{\mathcal{H}} &= -t \sum_{\langle i,j \rangle, s} (\hat{c}_{i,s}^\dagger \hat{c}_{j,s} + h.c.) + J \sum_i \hat{\mathbf{S}}_i^f \cdot \hat{\mathbf{S}}_i^c \\
 &= \sum_{\vec{\sigma}, \vec{\sigma}'} [\hat{W}_1 \hat{W}_2 \dots \hat{W}_{\mathcal{L}}]_{\vec{\sigma}}^{\vec{\sigma}'} |\vec{\sigma}\rangle \langle \vec{\sigma}'|
 \end{aligned} \tag{3.6}$$

To ensure proper connectivity of the right operators, the matrices \hat{W}_i need to be constructed accordingly. This construction is particularly relevant for local operators $\hat{X}_i = J \hat{\mathbf{S}}_i^f \cdot \hat{\mathbf{S}}_i^c$:

$$\hat{W}_1 = \begin{pmatrix} \hat{X}_1 & \mathbb{I} \end{pmatrix}, \hat{W}_i = \begin{pmatrix} \mathbb{I} & 0 \\ \hat{X}_i & \mathbb{I} \end{pmatrix}, \hat{W}_{\mathcal{L}} = \begin{pmatrix} \mathbb{I} \\ \hat{X}_{\mathcal{L}} \end{pmatrix} \tag{3.7}$$

This readily leads to a tensor product of single local operators. Adding the nearest neighbor interaction $\hat{A}_i \otimes \hat{B}_i = -t(\hat{c}_i^\dagger \hat{c}_{i+1} + \hat{c}_i \hat{c}_{i+1}^\dagger)$, \hat{A}_i and \hat{B}_i are the local operators like \hat{X}_i , the total MPOs are given by:

$$\hat{W}_1 = \begin{pmatrix} \hat{X}_1 & \hat{A}_1 & \mathbb{I} \end{pmatrix}, \hat{W}_i = \begin{pmatrix} \mathbb{I} & 0 & 0 \\ \hat{B}_i & 0 & 0 \\ \hat{X}_i & \hat{A}_i & \mathbb{I} \end{pmatrix}, \hat{W}_{\mathcal{L}} = \begin{pmatrix} \mathbb{I} \\ \hat{B}_{\mathcal{L}} \\ \hat{X}_{\mathcal{L}} \end{pmatrix} \tag{3.8}$$

3.1.3 Symmetry

Symmetry stands as a cornerstone in physics, offering crucial indicators for distinct quantum states and quantum phase transitions are often accompanied by a switch of symmetries.

Symmetry's consequences include the commutation of Hamiltonian H and symmetry group generators T_i : $[H, T_i] = 0$, leading to a block-diagonal Hamiltonian structure. This structural simplification reduces computational load by eliminating unnecessary zero elements. In tensor networks, the impact of symmetries is profound. Symmetry's existence implies tensor sparsity, facilitating compression for significant numerical efficiency gains. Employing diverse symmetries also enables the exploration of symmetry-breaking phenomena.

This thesis delegates the task of symmetry tracking to the QSpace tensor library [67]. This library offers an efficient framework for matrix product state (MPS) computations, enabling the integration of discrete, abelian, and non-Abelian symmetries.

3.2 Density Matrix Renormalization Group

In this section we are going to give a detailed introduction of Density Matrix Renormalization Group (DMRG) method [65].

Here we start with the on-site algorithm. The process begins by optimizing the M -matrix on the initial site. Moving forward, we proceed to optimize matrices on subsequent sites, iteratively reducing the energy of $|\Psi\rangle$ with each refined M -matrix update.

$$E = \frac{\langle \Psi | \hat{\mathcal{H}} | \Psi \rangle}{\langle \Psi | \Psi \rangle} \quad (3.9)$$

The optimization of $|\Psi\rangle$ can be formulated as a Lagrangian optimization problem, we aim for minimizing $\langle \Psi | \hat{\mathcal{H}} | \Psi \rangle$ under the condition $\langle \Psi | \Psi \rangle = 1$.

We find the Lagrange equation for site- l optimization to be

$$\frac{\partial}{\partial M_l^\dagger} [\langle \Psi | \hat{\mathcal{H}} | \Psi \rangle - \lambda \langle \Psi | \Psi \rangle] = 0 \quad (3.10)$$

where we can find a simple eigenvalue equation:

$$H_l^{(1)} \psi_l^{(1)} = \lambda \psi_l^{(1)} \quad (3.11)$$

where $\psi_l^{(1)} = M_l$ with normalization $[\psi_l^{(1)}]^\dagger \psi_l^{(1)} = 1$.

Solving Eq. (3.11) using an eigensolver will yield a new matrix \tilde{M}_l along with the corresponding eigenvalue λ , which approximates the ground state energy. This new \tilde{M}_l is then employed to update the MPS as $M_l \rightarrow \tilde{M}_l$. Moving to the next site, the SVD is applied to \tilde{M}_l to shift the orthogonality center to site $l + 1$. This entire process is repeated for the subsequent site (as shown in Fig. 3.4).

The optimization of the MPS can commence from an arbitrary state that may be distant from the actual ground state initially. By iteratively optimizing the MPS and performing sweeps back and forth, convergence is achieved when the ground state energy remains unchanged with respect to a fixed bond dimension D .

The matrix dimensions of $H_l^{(1)}$ are typically of the order $D^2 d \times D^2 d$, which can be large. Consequently, a numerical technique like the Lanczos iterative solver, which targets the lowest eigenvalue of the system, is employed [68–71].

However, a potential challenge lies in the risk of encountering a local minimum during the ground state search. This situation arises when an eigenstate that is not the actual ground state is found.

An alternative strategy to evade local minima is provided by the two-site DMRG technique [63, 72, 73], this method involves treating pairs of sites concurrently, it naturally introduces bond expansion, although it entails significantly greater computational demands. The computational cost of one-site

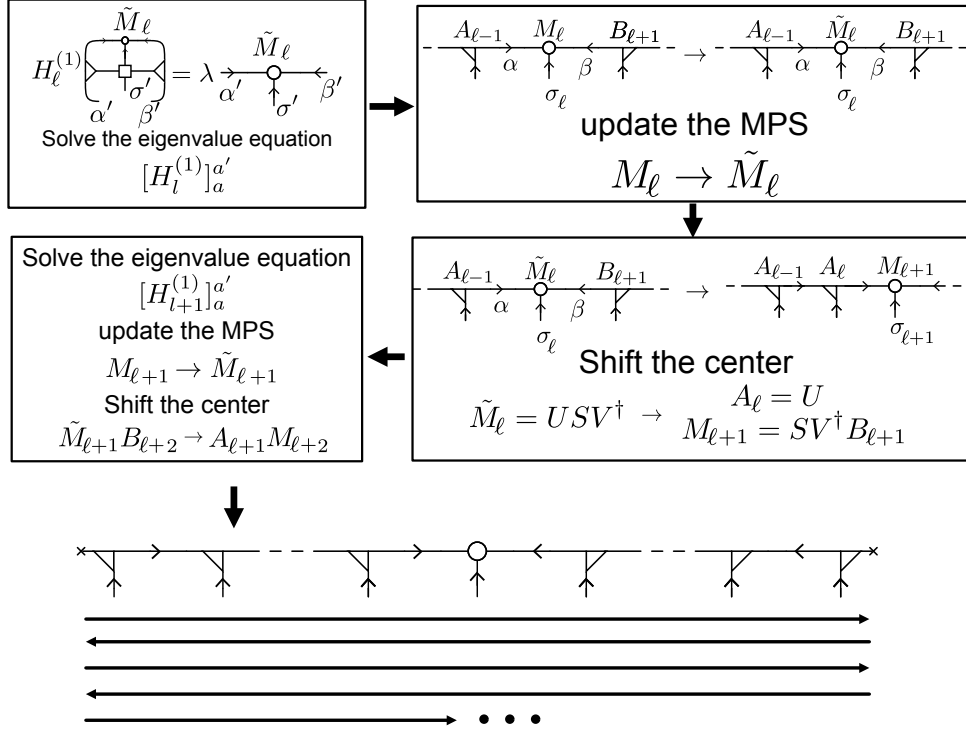


Figure 3.4: The diagrammatic representation of DMRG process, iteratively optimize the MPS to the ground state. The technical details can be seen in Appendix. A.2.

DMRG is $\mathcal{O}(D^3 dw + D^2 d^2 w^2)$, while the cost of two-site DMRG is substantially higher: $\mathcal{O}(D^3 d^3 + D^3 d^2 w)$.

As efforts to enhance the computational efficiency of DMRG ground state search algorithms are of great value, alternative methods like density matrix perturbation [74], the center matrix wave function formalism [66], and subspace expansion [75] have been proposed for 1-site DMRG procedures involving symmetries. In 2023, an algorithm named "controlled bond expansion," introduced by Andreas Gleis, Jheng-Wei Li, and Jan von Delft, has made significant strides. This innovative approach achieves considerable energy reduction in each iteration, ensuring two-site DMRG accuracy and sweep convergence. Notably, it achieves these improvements while maintaining a computational cost equivalent to that of a one-site algorithm [61].

3.2.1 Controlled Bond Expansion DMRG

In the context of one-site optimization, the state's representation follows the form given in equation:

$$|\Psi\rangle = |\alpha\rangle|\sigma_l\rangle|\beta\rangle[M_l]^{\alpha\sigma_l\beta} \quad (3.12)$$

This representation is constrained to a variational space defined by the outgoing state space $|\alpha\rangle|\beta\rangle$. If the range of quantum numbers Q_α and Q_β for these spaces is too limited to accurately capture the ground state, one-site DMRG lacks the capability to effectively expand them.

In contrast, the two-site DMRG approach does not encounter this problem. The action of the effective Hamiltonian between two sites allows for an enlargement of the bond dimension. This addition encompasses the full range of required quantum numbers on that bond. Thus, the two-site optimization can introduce missing quantum numbers if necessary.

However, this advantage comes at the cost of increased complexity. The effective two-site Hamiltonian has a dimension of $D^2d^2 \times D^2d^2$, while the effective one-site Hamiltonian is smaller with a dimension of $D^2d \times D^2d$.

The Hilbert space of $H_l^{(1)}$ and $H_l^{(2)}$

Here, we are adopting the diagrammatic conventions outlined in Ref. [76]. During the truncation process in DMRG, we introduce orthogonal complements of the kept states (A_l and B_l), referred to as the discarded states (\bar{A}_l and \bar{B}_l). The dimensions of A_l and B_l are denoted as D , and their complements \bar{A}_l and \bar{B}_l have dimensions \bar{D} . We also define the parent state (P):

$$A_l^{\mathbb{I}} = A_l + \bar{A}_l, B_l^{\mathbb{I}} = B_l + \bar{B}_l, D + \bar{D} = Dd \quad (3.13)$$

$$\frac{A_l}{D \begin{array}{|c} \diagdown \\ \diagup \end{array} D} \oplus \frac{\bar{A}_l}{D \begin{array}{|c} \diagup \\ \diagdown \end{array} \bar{D}} = \frac{A_l^{\mathbb{I}}}{D \begin{array}{|c} \diagdown \\ \diagup \end{array} Dd}, \quad \frac{B_l^{\mathbb{I}}}{Dd \begin{array}{|c} \diagup \\ \diagdown \end{array} D} = \frac{B_l}{D \begin{array}{|c} \diagdown \\ \diagup \end{array} D} \oplus \frac{\bar{B}_l}{\bar{D} \begin{array}{|c} \diagup \\ \diagdown \end{array} \bar{D}}$$

Figure 3.5: The diagrammatic representation of the kept states A_l (left-isometry) and B_l (right-isometry), discarded states \bar{A}_l , \bar{B}_l , and the parent states $A_l^{\mathbb{I}}$, $B_l^{\mathbb{I}}$. Taken from Ref. [61]

By comparing the terms in Fig. 3.6, it becomes evident that the first three terms (KK, DK, KD) from the third line also appear in the first two lines. However, the fourth term (DD) is unique to the third line and doesn't appear in the first two lines. This implies that the Hilbert space represented by DD contains information that is not encompassed by one-site DMRG at sites l and $l + 1$, but is explored by two-site DMRG.

The DD subspace should contain information that is orthogonal to the relevant Hilbert spaces of one-site DMRG at sites l and $l + 1$. It's important

$$\begin{aligned}
 H_l^{1s} \psi_l^{1s} &\rightarrow \text{Diagram 1} = \text{Diagram 2} = \text{Diagram 3} \oplus \text{Diagram 4}, \\
 H_{l+1}^{1s} \psi_{l+1}^{1s} &\rightarrow \text{Diagram 5} = \text{Diagram 6} = \text{Diagram 7} \oplus \text{Diagram 8}, \\
 H_l^{2s} \psi_l^{2s} &\rightarrow \text{Diagram 9} \oplus \text{Diagram 10} \oplus \text{Diagram 11} \oplus \text{Diagram 12}.
 \end{aligned}$$

Figure 3.6: The diagrammatic representation of $H_l^{1s} \psi_l^{1s}$, $H_{l+1}^{1s} \psi_{l+1}^{1s}$ and $H_l^{2s} \psi_l^{2s}$, notice that all the final MPS are in bond-canonical. Taken from Ref. [61]

to note that the dimension of the DD subspace is $\tilde{D}^2 = D^2(d-1)^2$, which is significantly larger than any other subspace within one-site DMRG.

The crucial realization to eliminate the misleading term involves selecting the appropriate subspace within DD, referred to as the "relevant DD". This technique is known as "Shrewd selection."

The details of shrewd selection can be seen in Appendix. B, it is the first step of the entire CBE-DMRG.

Here, the updated bond dimension becomes $D + \tilde{D}$, leading to the expanded isometry $A_l^{ex} = A_l \oplus A_l^{tr}$. In the context of a sweep progressing from right to left, the second step involves updating the site: $C_{l+1} \rightarrow C_{l+1}^{ex,i}$. This update is defined as $A_l^{ex} C_{l+1}^{ex,i} = A_l C_{l+1}$, ensuring the overall isometry of the entire MPS remains consistent:

$$\frac{A_l}{D \begin{array}{|c} \diagdown \\ d \\ \diagup \end{array} D} \oplus \frac{\tilde{A}_l^{tr}}{D \begin{array}{|c} \diagdown \\ d \\ \diagup \end{array} \tilde{D}} = \frac{A_l^{ex}}{D \begin{array}{|c} \diagdown \\ d \\ \diagup \end{array} (D + \tilde{D})} \frac{C_{l+1}^{ex}}{d \begin{array}{|c} \diagdown \\ d \\ \diagup \end{array} D} = \text{Diagram 13}$$

Figure 3.7: The diagrammatic representation of A_l and C_{l+1} expansion. Taken from Ref. [61]

Additionally, an expanded one-site Hamiltonian is constructed within a variational space of dimension $D(D + \tilde{D})d$:

In the third step, we solve the equation $(H_{l+1}^{1s,ex} - E)C_{l+1}^{ex}$ just as in the standard DMRG procedure. However, with the crucial information of H_l^{2s} available, we are empowered to shift the center from site $l + 1$ back to site l through truncation. This results in the bond dimension reverting to D , and it signifies the commencement of the subsequent bond expansion.

The discarded weight ξ can serve as a measure of error, providing insights into the quality of the approximation.

3. Method: Density Matrix Renormalization Group

$$H_{l+1}^{1s,ex} = \left[\begin{array}{c} \text{Diagram 1} \\ \text{Diagram 2} \end{array} \right]_{l+1} = \left[\begin{array}{c} D + \tilde{D} \\ d \\ \text{Diagram 3} \end{array} \right]_{l+1}^D$$

Figure 3.8: The diagrammatic representation of expanded Hamiltonian. Taken from Ref. [61]

Each step in this process incurs a maximum cost equivalent to that of one-site DMRG, $\mathcal{O}(D^3 dw)$. Furthermore, the Controlled Bond Expansion (CBE) DMRG method effectively captures the most pertinent contributions originating from H_l^{2s} .

Numerical Results

4.1 Correlation Function of 1D KLM

In one dimension, it's well-established that various interacting metallic systems, including the Hubbard model and the $t - J$ model, fall under the universality class of Tomonaga-Luttinger liquids (TLL), and the Kondo lattice model also belongs to this class [10].

In Tomonaga-Luttinger liquids, electron density oscillations in response to a local perturbation play a crucial role in understanding the electronic states of a system. The response to an impurity potential is a well-known phenomenon called Friedel oscillations. Similarly, magnetic impurities induce spin density oscillations. The period of these oscillations is determined by the diameter of the Fermi surface, which, in one-dimensional systems, is referred to as the Fermi wave vector [11].

In the half-spin TL liquids, there are gapless charge and spin excitations. These can be characterized by certain parameters.

For the charge excitations, the key parameter is the Luttinger parameter, denoted as K_ρ . The Spin excitations in the same system are also characterized by a Luttinger parameter, but in this case, it is fixed by the SU(2) symmetry, meaning $K_\sigma = 1$. Due to the gapless nature of these excitations, the correlation functions in TL liquid exhibit power-law decays, which are determined by the Luttinger parameter for charge excitation, K_ρ .

According to the bosonization method and other numerical studies [11][77], the asymptotic expressions for the single-particle excitations and the spin-spin correlation are as follows:

$$\mathcal{C}_{GS}(x) = \langle \hat{c}_i^\dagger \hat{c}_j \rangle = A_1 \frac{\cos(k_F x)}{|x|^\alpha} \quad (4.1)$$

$$\mathcal{S}_{GS}(x) = \langle \hat{\mathbf{S}}_i \hat{\mathbf{S}}_j \rangle = \frac{1}{(\pi x)^2} + B_1 \frac{\cos(2k_F x) \log^\beta(x)}{|x|^{1+K_\rho}} \quad (4.2)$$

4. Numerical Results

where $\langle \hat{O} \rangle = \langle GS | \hat{A} | GS \rangle$ and $|GS\rangle$ is the ground states of typical one-dimensional heavy Fermion system; k_F is the Fermi wave vector of system; $x = |i-j|$; α is an unknown coefficient; β arises from the logarithmic correction for one-dimensional quantum system [78].

The charge density oscillation has a form like:

$$\mathcal{N}_{GS}(x) = \langle \delta \hat{n}(x) \rangle = \langle \delta(\hat{c}_i^\dagger \hat{c}_i) \rangle \sim C_1 \frac{\cos(2k_F x)}{|x|^{(1+K_\rho)/2}} + C_2 \frac{\cos(4k_F x)}{|x|^{2K_\rho}} \quad (4.3)$$

here x represents the distance from the impurity. In the system considered in this project, it signifies the distance from site i to the boundary of the system.

In principle, we can extract the necessary properties such as the Fermi wave vector k_F , the Luttinger parameter K_ρ , and the coefficients α and β from the numerical results. However, it's crucial to account for finite system size effects, especially in specific calculations

Finite System Size and Bond Dimension Correction For a finite size system, due to the boundaries, an exponential decay will appear in relative distance $x = |i-j|$ correlation with a finite value λ : $e^{-\frac{x}{\lambda}}$.

So as the practical numerical results, the single-particle excitation Eq. (4.1) and the spin-spin correlation Eq. (4.2) becomes:

$$\mathcal{C}(x) = \langle \hat{c}_i^\dagger \hat{c}_j \rangle = A_1 \frac{\cos(k_F x) e^{-\frac{x}{\lambda}}}{|x|^\alpha} \quad (4.4)$$

$$\mathcal{S}(x) = \langle \langle \hat{\mathbf{S}}_i \hat{\mathbf{S}}_j \rangle \rangle = \left(\frac{1}{(\pi x)^2} + B_1 \frac{\cos(2k_F x) \log^\beta(x)}{|x|^{1+K_\rho}} \right) e^{-\frac{x}{\lambda}} \quad (4.5)$$

In numerical method point of view, the DMRG approximates the true ground state of a MPS, the correlation length are expected $\lambda \rightarrow \infty$ when $D \rightarrow \infty$, or equivalently when $\xi \rightarrow 0$.

And for the charge density oscillation Eq. (4.3), a standard conformal transformation [77] for a finite chain of length N is:

$$\mathcal{N}(x) = \langle \delta \hat{n}(x) \rangle \sim C_1 \frac{\cos(2k_F x)}{\left(\frac{N}{\pi} \sin\left(\frac{x}{N+1}\pi\right) \right)^{(1+K_\rho)/2}} + C_2 \frac{\cos(4k_F x)}{\left(\frac{N}{\pi} \sin\left(\frac{x}{N+1}\pi\right) \right)^{2K_\rho}} \quad (4.6)$$

The extrapolation checks for finite system size correction are in Appendix C, and related coefficients λ will be omitted in this chapter for sake of brevity.

4.2 Fermi Wave Vector Behaviors

The one-dimensional Kondo lattice model is examined using the CBD-DMRG approach. We generate paramagnetic states, denoted as $|PM\rangle$, by varying two key parameters: the conduction electron density n_c and the Kondo couplings J .

$$n_c = 0.8, 0.7 \leq J \leq 2.3$$

$$n_c = 0.56, 0.3 \leq J \leq 1.7$$

These parameters are depicted in Fig. 2.3.

It's noteworthy that in the region $[n_c = 0.8, 1.5 \lesssim J \lesssim 2]^1$, we are situated within the *FM2* region. During this phase, we impose the constraint that the total spin of the states are both equal to 0. However, it's important to note that these states are not the ground states.

As we mentioned in Sec. 3.1.2, the observables $\langle \psi | \hat{O}_i \hat{O}_j | \psi \rangle$ can be computed easily from MPS and MPOs.

For a N -site Kondo chain, the correlators of $|PM\rangle$ can be illustrated as a $N \times N$ matrix, e.g.:

$$\rho(i, j) = \langle \hat{c}_i^\dagger \hat{c}_j \rangle \quad (4.7)$$

$$\sigma(i, j) = \langle \hat{\mathbf{S}}_i \hat{\mathbf{S}}_j \rangle \quad (4.8)$$

Here $\langle \hat{O} \rangle = \langle PM | \hat{O} | PM \rangle$, and 1D Kondo lattice system we have $\hat{\mathbf{S}}_i = \hat{\mathbf{S}}_i^f + \hat{\mathbf{S}}_i^c$.

It is easy to find that the density oscillation is just the diagonal term of matrix $\rho(i, j)$:

$$\mathcal{N}(x) = \langle \delta \hat{n}(x) \rangle = \langle \hat{n}(x) - n_c \rangle = \rho(x, x) - n_c \quad (4.9)$$

Since we use open boundary conditions, translational invariance is lost. $\rho(i, j)$ and $\sigma(i, j)$ depends on both i and j . For avoiding such boundary effect, we averaged over all pairs of sites separated by the distance $x = |i - j|$ from $\rho(i, j)$ and $\sigma(i, j)$:

$$\mathcal{C}(x) = \langle \rho(j + x, j) \rangle_j \quad (4.10)$$

$$\mathcal{S}(x) = \langle \sigma(j + x, j) \rangle_j \quad (4.11)$$

$j \in [1, N - x]$ and $\langle \cdot \rangle$ means taking the mean value for all possible j .

In this project, $k_F = \frac{\pi}{2} n_c$ denotes small Fermi wave vector and $k_F^* = \frac{\pi}{2}(n_c + 1)$ represents large Fermi wave vector. The parameter we use in calculations are:

For $n_c = 0.8$,

$$k_F = 0.4\pi, \quad 2k_F = 0.8\pi, \quad (4.12)$$

$$k_F^* = 0.9\pi, \quad 2k_F^* = 1.8\pi \sim 0.2\pi. \quad (4.13)$$

¹Here we use \lesssim since the boundaries between *FM2*-phase and *HTLL*-phase are not exactly solved.

4. Numerical Results

For $n_c = 0.56$,

$$k_F = 0.28\pi, \quad 2k_F = 0.56\pi, \quad (4.14)$$

$$k_F^* = 0.78\pi, \quad 2k_F^* = 1.56\pi \sim 0.44\pi. \quad (4.15)$$

To analyze numerically obtained correlation functions, we compare their Fourier transform with fitting curves. The curves, as expected, should have the properties of Eq. (4.1) and Eq. (4.2). Remarkably, from the numerically results, the correlation functions in the momentum space can have peaks at one-, two-, or even three wave vectors, the fitting has been done with the help of Eq. (4.16) and Eq. (4.17) :

$$\mathcal{C}(x) \sim c^{(n)}(x) = \sum_n a_n \frac{\cos(k_n^{(c)} x)}{x^{\alpha_n}}, n = 1, 2, 3 \quad (4.16)$$

$$\mathcal{S}(x) \sim s^{(n)}(x) = \frac{1}{(\pi x)^2} + \sum_n b_n \frac{\cos(2k_n^{(s)} x) \log^{\beta_n}(x)}{x^{1+K_\rho}}, n = 1, 2 \quad (4.17)$$

4.2.1 For $n_c = 0.8, N = 200$

Short/Long Range Oscillation

Due to the different decay modes for the short/long range correlation behaviors (exponential decay for short range and algebraic decay for long range), it makes distinctions in Fourier transform: the Fourier transform results of $\mathcal{C}(x)$ are almost the same when we choose $x \in [1, N - 1]$ and $x \in [1, N/10]$, but the results for $x \in [N/10, N - 1]$ are totally different in some J s.

Additionally, all correlation function results are displayed as absolute values in logarithmic scale to enhance visibility and clarity.

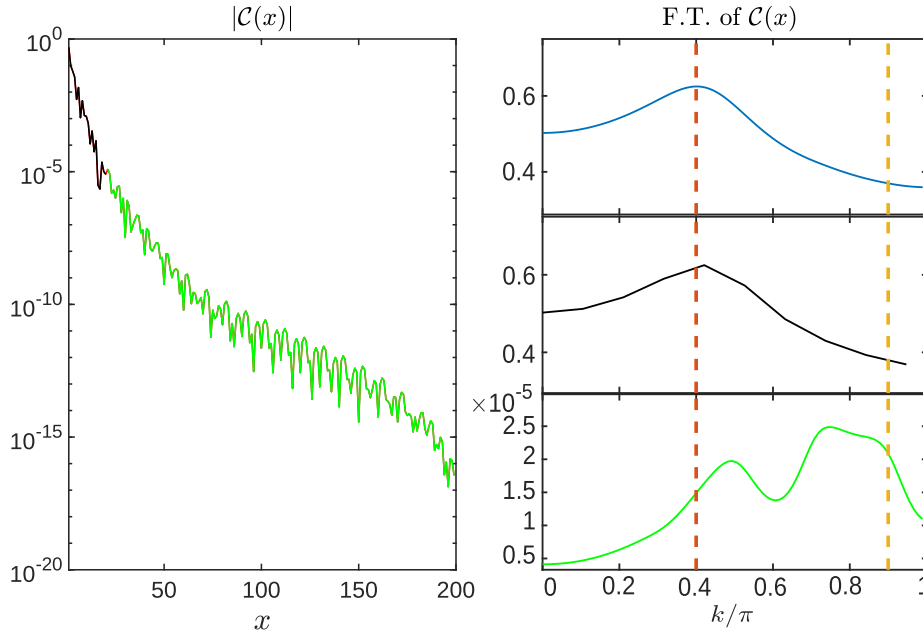


Figure 4.1: The Fourier transform of $\mathcal{C}(x)$ with different part of x for $N = 200, n_c = 0.8, J = 1.3$. In the left panel are $\mathcal{C}(x)$ with different range of x : $x \in [1, N - 1]$, $x \in [1, N/10]$ (black) and $x \in [N/10, N - 1]$ (green). In the right panel are the related Fourier transform result of $\mathcal{C}(x)$ for each x -region. Red and yellow dashed lines in the right columns correspond to the small, k_F , and large, k_F^* , Fermi vectors. The information of $x \in [N/10, N - 1]$ is almost covered by the oscillation of $x \in [1, N/10]$ in Fourier transform results, since their absolute values are in totally different order of magnitude.

From the Fourier transform results, we found that for small distance correlation ($x < 0.1N$), the oscillation behaviors are always associated with k_F . And the long-range behaviors can be fitted by Eq. (4.16) and Eq. (4.17).

In spin sector, such short/long range oscillation separation also appears, as it shows in Fig. 4.2.

4. Numerical Results

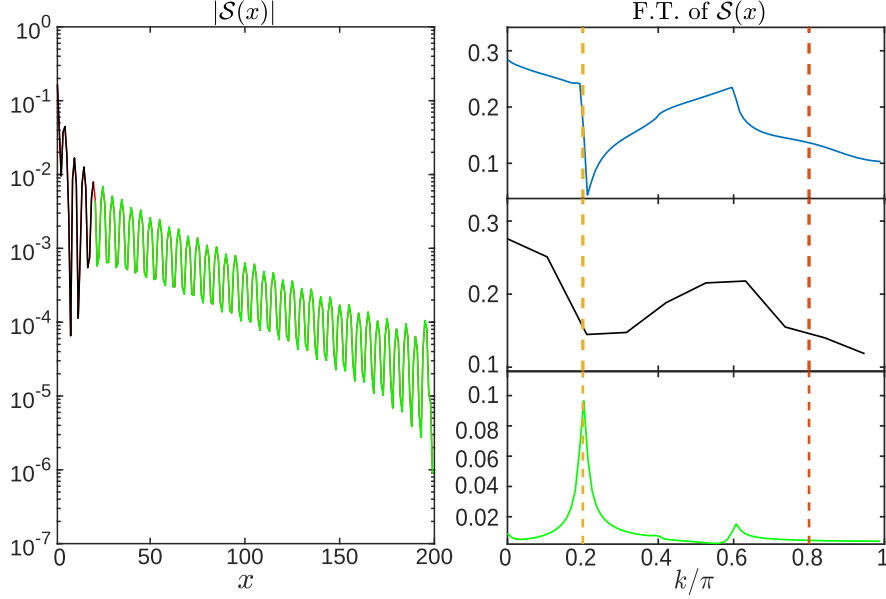


Figure 4.2: The Fourier transform of $\mathcal{S}(x)$ with different part of x for $N = 200, n_c = 0.8, J = 1.3$. In the left panel are $\mathcal{S}(x)$ with different range of x : $x \in [1, N - 1]$, $x \in [1, N/10]$ (black) and $x \in [N/10, N - 1]$ (green). In the right panel are the related Fourier transform result of $\mathcal{C}(x)$ for each x -region. Red and yellow dashed lines in the right columns correspond to the $2k_F$ and $2k_F^*$. The same as in Fig. 4.1, the long range oscillation is covered by short range oscillation in Fourier transform results.

A possible reason is, a correlation function of 1D KLM $\mathcal{F}(x)$ has two components: short range oscillation $\mathcal{F}^S(x)$ and long range oscillation $\mathcal{F}^L(x)$.

$\mathcal{F}^S(x)$ always has k_F related oscillation, the amplitude is large in the beginning but decays rapidly with x . For the $\mathcal{F}^L(x)$, it oscillates with k , such oscillation decays so slow that it can pronounce in large x .

$$\mathcal{F}^S(x) \sim A_1 \cos(nk_F x) e^{-\frac{x}{m_S}} \quad (4.18)$$

$$\mathcal{F}^L(x) \sim A_2 \frac{\cos(nkx)}{|x|^{m_L}} \quad (4.19)$$

where n is an integer, k changes with J , $A_1 \gg A_2$, m_S and m_L are constants. $|\mathcal{F}^L(x)| \gg |\mathcal{F}^S(x)|$ in large x so that influence of $\mathcal{F}^S(x)$ is negligible in long range interaction.

In this project we focus on $\mathcal{F}^L(x)$ part, since the most interesting large-small Fermi wave vector transient happens here.

Small/Large Fermi Wave Vector Transient

We mark the peaks in charge sector by $k_n^{(c)}$, the peaks in spin sector by $k_n^{(s)}$.

- $J = 0.7$, there is only one peak in both correlation function of charge sector $\mathcal{C}(x)$ and spin sector $\mathcal{S}(x)$ which correspond to the small Fermi wave vector, $k_1^{(c)} = k_1^{(s)} = k_F$. As shown in Fig. 4.3

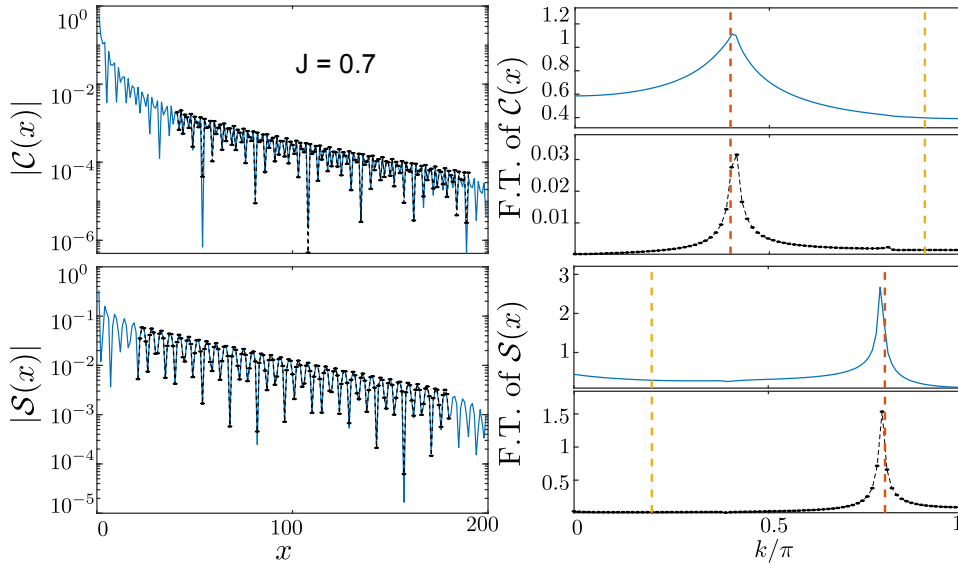


Figure 4.3: The correlation function $\mathcal{C}(x)$ (top, left) and $\mathcal{S}(x)$ (bottom, left), and their Fourier transform results (right column) for $J = 0.7$. Blue solid lines in the left column shows the absolute values of empirical data in log scale derived from DMRG simulations while black dashed lines represent the outcome of curve fitting obtained by using Equation (4.16) and (4.17), respectively. Blue lines in the right columns are Fourier transforms of the corresponding correlation functions. And the black dashed lines in the right column correspond to the black dashed line in left column, represent the oscillation behaviors in relative long range ($x > 0.1N$) and where the finite size effects are excluded (exclude the points $x \sim N$). Red and yellow dashed lines in the top of right columns correspond to the small, k_F , and large, k_F^* , Fermi vectors while these lines in spin sector denote the values of $2k_F$ (red) and $2k_F^*$ (yellow). This result was obtained for the coupling constant: $J = 0.7$.

4. Numerical Results

- $0.8 \leq J \leq 1$, the second peak $k_2^{(c)} = 0.8\pi$ appears in charge sector.

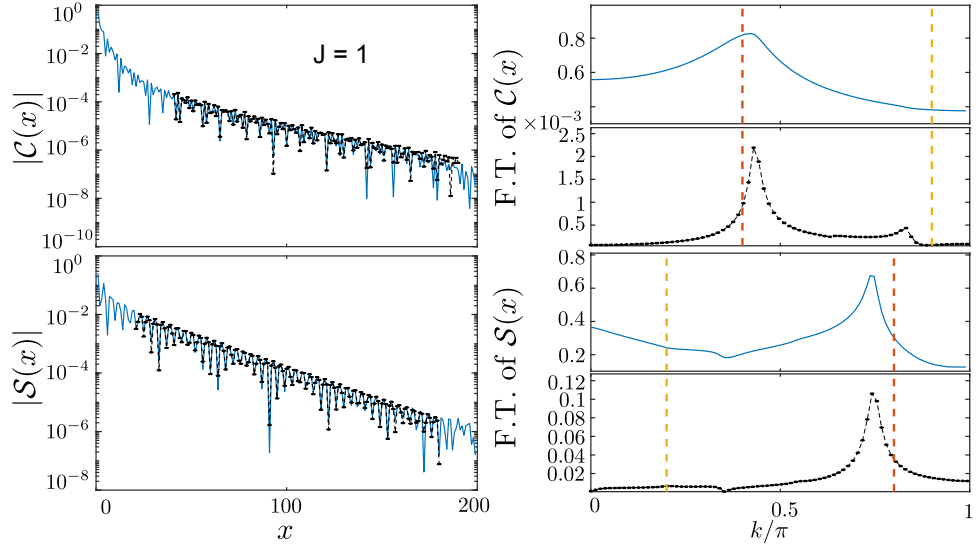


Figure 4.4: The correlation function $\mathcal{C}(x)$ (top, left) and $\mathcal{S}(x)$ (bottom, left), and their Fourier transform results (right column) for $J = 1$. Blue solid lines in the left column shows the absolute values of empirical data in log scale derived from DMRG simulations while black dashed lines represent the outcome of curve fitting obtained by using Equation (4.16) and (4.17), respectively. Blue lines in the right columns are Fourier transforms of the corresponding correlation functions. And the black dashed lines in the right column correspond to the black dashed line in left column, represent the oscillation behaviors in relative long range ($x > 0.1N$) and where the finite size effects are excluded (exclude the points $x \sim N$). Red and yellow dashed lines in the top of right columns correspond to the small, k_F , and large, k_F^* , Fermi vectors while these lines in spin sector denote the values of $2k_F$ (red) and $2k_F^*$ (yellow).

- $1.1 \leq J \leq 1.5$, there are now three peaks in charge sector and two peaks in spin sector. The dominant peak changed in spin sector from k_F to k_F^* at $J = 1.2$

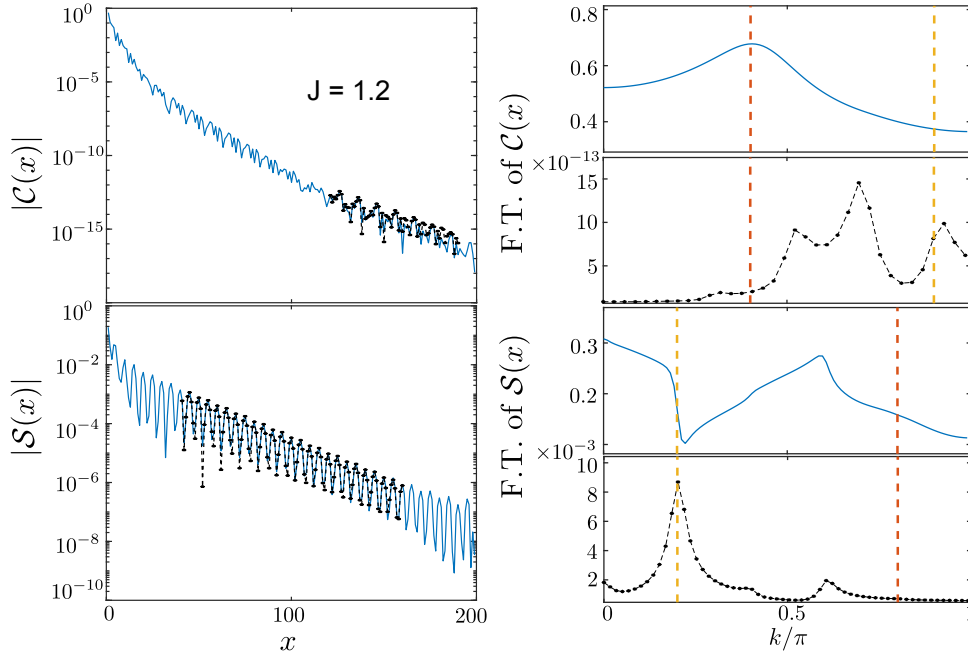


Figure 4.5: The correlation function $\mathcal{C}(x)$ (top, left) and $\mathcal{S}(x)$ (bottom, left), and their Fourier transform results (right column) for $J = 1.2$. Blue solid lines in the left column shows the absolute values of empirical data in log scale derived from DMRG simulations while black dashed lines represent the outcome of curve fitting obtained by using Equation (4.16) and (4.17), respectively. Blue lines in the right columns are Fourier transforms of the corresponding correlation functions. And the black dashed lines in the right column correspond to the black dashed line in left column, represent the oscillation behaviors in relative long range ($x > 0.1N$) and where the finite size effects are excluded (exclude the points $x \sim N$). Red and yellow dashed lines in the top of right columns correspond to the small, k_F , and large, k_F^* , Fermi vectors while these lines in spin sector denote the values of $2k_F$ (red) and $2k_F^*$ (yellow).

4. Numerical Results

- $2 \leq J \leq 2.3$, only two peaks remain in $\mathcal{C}(x)$, one is at large Fermi wave vector $k_2^{(c)} \approx k_F^*$, another one is far away from small Fermi wave vector k_F .
And there is only one peak in $\mathcal{S}(x)$, at large Fermi wave vector k_F^* .

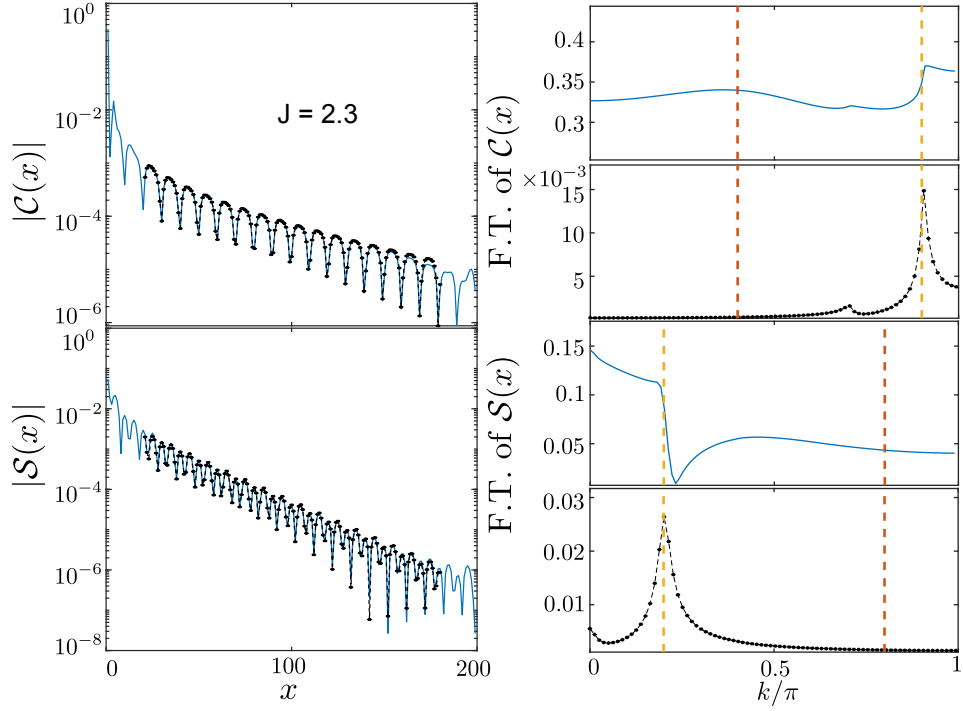


Figure 4.6: The correlation function $\mathcal{C}(x)$ (top, left) and $\mathcal{S}(x)$ (bottom, left), and their Fourier transform results (right column) for $J = 2.3$. Blue solid lines in the left column shows the absolute values of empirical data in log scale derived from DMRG simulations while black dashed lines represent the outcome of curve fitting obtained by using Equation (4.16) and (4.17), respectively. Blue lines in the right columns are Fourier transforms of the corresponding correlation functions. And the black dashed lines in the right column correspond to the black dashed line in left column, represent the oscillation behaviors in relative long range ($x > 0.1N$) and where the finite size effects are excluded (exclude the points $x \sim N$). Red and yellow dashed lines in the top of right columns correspond to the small, k_F , and large, k_F^* , Fermi vectors while these lines in spin sector denote the values of $2k_F$ (red) and $2k_F^*$ (yellow).

4.2. Fermi Wave Vector Behaviors

The long range oscillation behaviors of $n_c = 0.8$ are summarized in Table. 4.1.

	$\mathcal{C}(x)$	$\mathcal{S}(x)$	k
$J = 0.7$	$c^{(1)}(x)$	$s^{(1)}(x)$	$k_1^{(c)} = k_1^{(s)} \approx k_F$
$0.8 \leq J \leq 1$	$c^{(2)}(x)$		$k_1^{(c)} = k_1^{(s)} \approx k_F, k_2^{(c)} \approx 0.8\pi$
$J = 1.1$	$c^{(3)}(x)$	$s^{(2)}(x)$	$k_1^{(c)} \approx 0.5\pi, k_2^{(c)} \approx 0.7\pi, k_3^{(c)} \approx k_F^*$ $k_1^{(s)} \approx 0.15\pi$ or $0.85\pi, k_2^{(s)} \approx k_F$
$1.2 \leq J \leq 1.5$			$k_1^{(c)} \approx 0.5\pi, k_2^{(c)} \approx 0.7\pi, k_3^{(c)} \approx k_F^*$ $k_1^{(s)} \approx k_F^*, k_2^{(s)} \approx 0.3\pi$ or 0.7π
$2 \leq J \leq 2.3$	$c^{(2)}(x)$	$s^{(1)}(x)$	$k_1^{(c)} \approx 0.7\pi, k_2^{(c)} \approx k_F^*$ $k_1^{(s)} \approx k_F^*$

Table 4.1: Summary of results for $n_c = 0.8$. In $c^{(3)}(x)$ region, a wave vector $k_2^{(c)}$ appears, which is neither k_F nor k_F^* .

Additionally, the Fourier transform of both correlation functions are shown in Fig. 4.7, we come across a crossover from the small- to large Fermi surface. Various regimes in the charge and spin sector present.

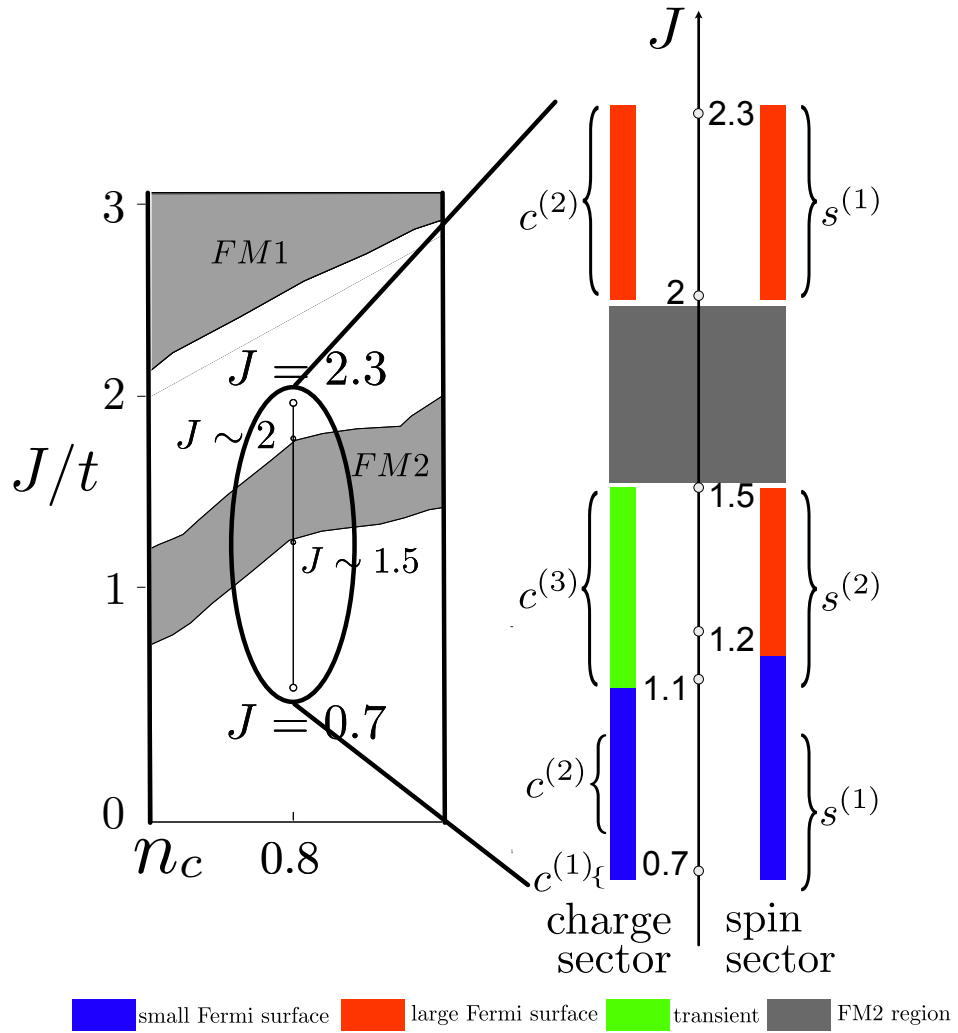


Figure 4.7: The schematic phase diagram for according to the long range oscillations for $\mathcal{C}(x)$ and $\mathcal{S}(x)$ for $n_c = 0.8$, $0.7 \leq J \leq 2.3$.

4.2.2 For $n_c = 0.56, N = 200$

The same as what showed in Sec. 4.2.1, at $n_c = 0.56$, the short/long range oscillation separation also exists. In the similar way we analyze the $\mathcal{S}(x)$ and $\mathcal{C}(x)$:

- $0.3 \leq J \leq 0.7$, only one peak on $\mathcal{C}(x)$ and $\mathcal{S}(x)$, located in k_F . $k_1^{(c)} = k_1^{(s)} \approx k_F$

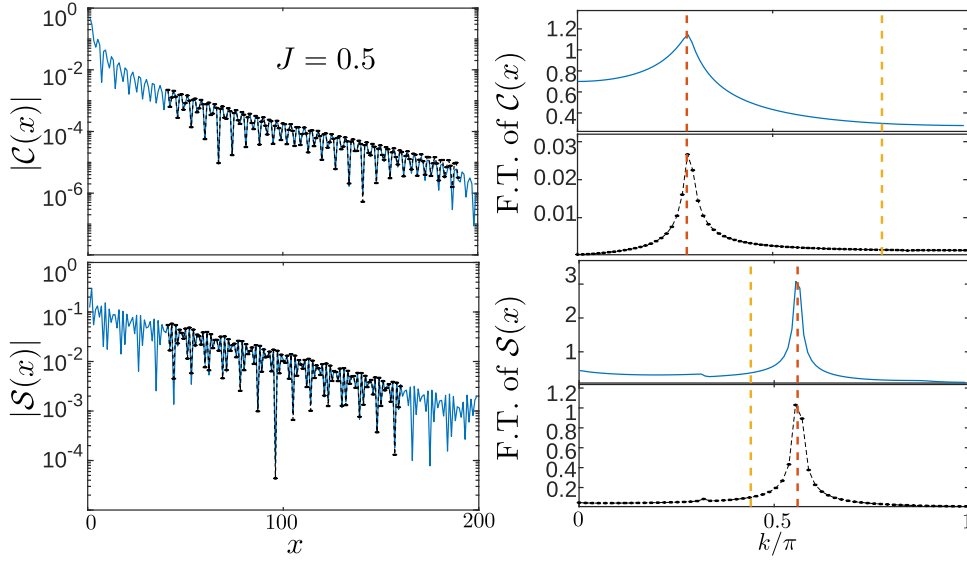


Figure 4.8: The correlation function $\mathcal{C}(x)$ (top, left) and $\mathcal{S}(x)$ (bottom, left), and their Fourier transform results (right column) for $J = 0.5$. Blue solid lines in the left column shows the absolute values of empirical data in log scale derived from DMRG simulations while black dashed lines represent the outcome of curve fitting obtained by using Equation (4.16) and (4.17), respectively. Blue lines in the right columns are Fourier transforms of the corresponding correlation functions. And the black dashed lines in the right column correspond to the black dashed line in left column, represent the oscillation behaviors in relative long range ($x > 0.1N$) and where the finite size effects are excluded (exclude the points $x \sim N$). Red and yellow dashed lines in the top of right columns correspond to the small, k_F , and large, k_F^* , Fermi vectors while these lines in spin sector denote the values of $2k_F$ (red) and $2k_F^*$ (yellow).

4. Numerical Results

- $J = 0.9$, in charge sector the second peak around k_F^* appears, in spin sector, the form of $s(x)$ remains the same, but the peak jumps to the large Fermi wave vector.

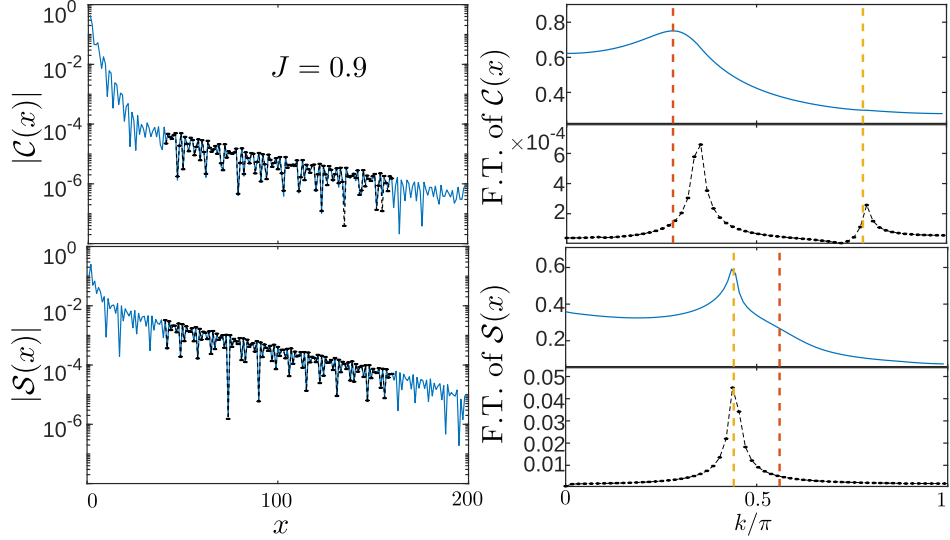


Figure 4.9: The correlation function $\mathcal{C}(x)$ (top, left) and $\mathcal{S}(x)$ (bottom, left), and their Fourier transform results (right column) for $J = 0.9$. Blue solid lines in the left column shows the absolute values of empirical data in log scale derived from DMRG simulations while black dashed lines represent the outcome of curve fitting obtained by using Equation (4.16) and (4.17), respectively. Blue lines in the right columns are Fourier transforms of the corresponding correlation functions. And the black dashed lines in the right column correspond to the black dashed line in left column, represent the oscillation behaviors in relative long range ($x > 0.1N$) and where the finite size effects are excluded (exclude the points $x \sim N$). Red and yellow dashed lines in the top of right columns correspond to the small, k_F , and large, k_F^* , Fermi vectors while these lines in spin sector denote the values of $2k_F$ (red) and $2k_F^*$ (yellow).

- $1 \leq J \leq 1.7$, in $\mathcal{C}(x)$ the peak ratio $\frac{A(k_1^{(c)})}{A(k_2^{(c)})}$ keeps decreasing, and there is no third peak in $\mathcal{C}(x)$ and no second peak in $\mathcal{S}(x)$ for all J at $n_c = 0.56$.

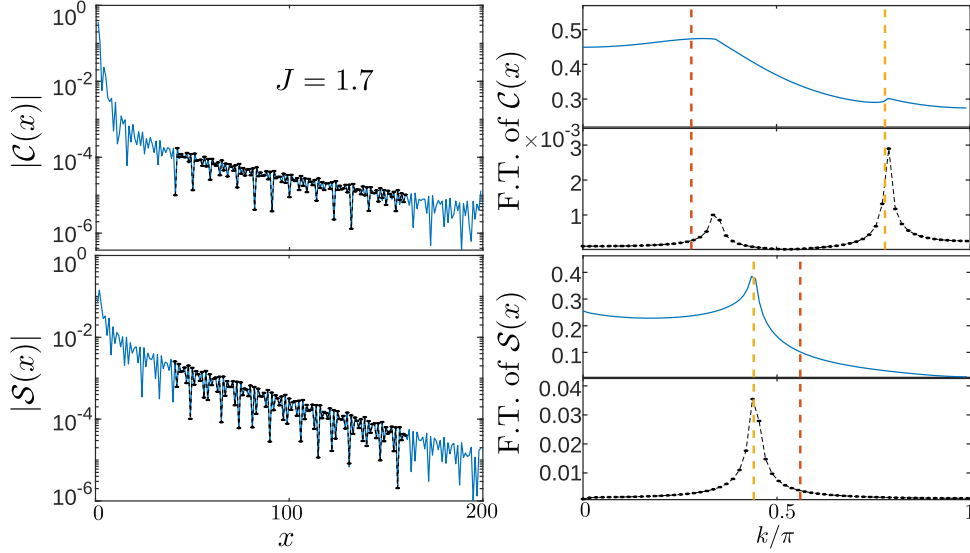


Figure 4.10: The correlation function $\mathcal{C}(x)$ (top, left) and $\mathcal{S}(x)$ (bottom, left), and their Fourier transform results (right column) for $J = 1.7$. Blue solid lines in the left column shows the absolute values of empirical data in log scale derived from DMRG simulations while black dashed lines represent the outcome of curve fitting obtained by using Equation (4.16) and (4.17), respectively. Blue lines in the right columns are Fourier transforms of the corresponding correlation functions. And the black dashed lines in the right column correspond to the black dashed line in left column, represent the oscillation behaviors in relative long range ($x > 0.1N$) and where the finite size effects are excluded (exclude the points $x \sim N$). Red and yellow dashed lines in the top of right columns correspond to the small, k_F , and large, k_F^* , Fermi vectors while these lines in spin sector denote the values of $2k_F$ (red) and $2k_F^*$ (yellow).

The long range oscillation behaviors of $n_c = 0.56$ are summarized in Table. 4.2.

Compares with the results of $n_c = 0.8$, there is no third peak in charge sector and in the transient phase only exists the competition of k_F and k_F^* .

4. Numerical Results

	$\mathcal{C}(x)$	$\mathcal{S}(x)$	k
$0.3 \leq J \leq 0.7$	$c^{(1)}(x)$	$s^{(1)}(x)$	$k_1^{(c)} = k_1^{(s)} \approx k_F$
$J = 0.9$	$c^{(2)}(x)$		$k_1^{(c)} \approx k_F, k_2^{(c)} = k_1^{(s)} \approx k_F^*$
$1 \leq J \leq 1.7$			

Table 4.2: Summary of results for $n_c = 0.56$.

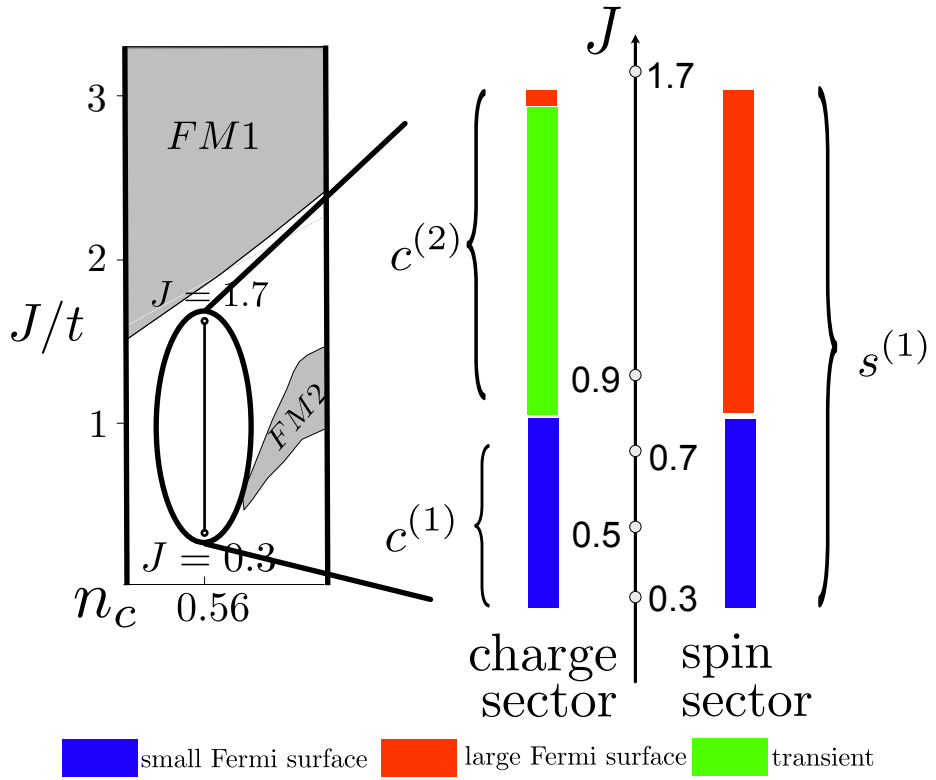


Figure 4.11: The schematic phase diagram for according to the long range oscillations for $\mathcal{C}(x)$ and $\mathcal{S}(x)$ for $\mathcal{C}(x)$ and $\mathcal{S}(x)$ for $n_c = 0.56$, $0.3 \leq J \leq 1.7$.

4.3 Luttinger Parameter K_ρ

Recalling the form of the charge density oscillation in Eq. (4.3):

$$\mathcal{N}_{GS}(x) = \langle \delta \hat{n}(x) \rangle = \langle \delta(\hat{c}_i^\dagger \hat{c}_i) \rangle \sim C_1 \frac{\cos(2k_F x)}{|x|^{(1+K_\rho)/2}} + C_2 \frac{\cos(4k_F x)}{|x|^{2K_\rho}}$$

It's important to note that it's not possible to distinguish the peak at $4k_F = 2\pi n_c$ from the peak at $4k_F^* = 2\pi(1 + n_c)$. Moreover, from the numerical results, it appears that C_2 is significantly greater than C_1 . For these reasons, using $\mathcal{N}(x)$ to determine the length of the Fermi wave vector is challenging.

However, through the curve-fitting process, it is still possible to extract the Luttinger parameter K_ρ from $\rho(i, i)$ and compare the results obtained from the curve fitting of $\mathcal{S}(x)$.

As the system is symmetric, only half of the chain is presented for all $|\mathcal{N}(x)|$.

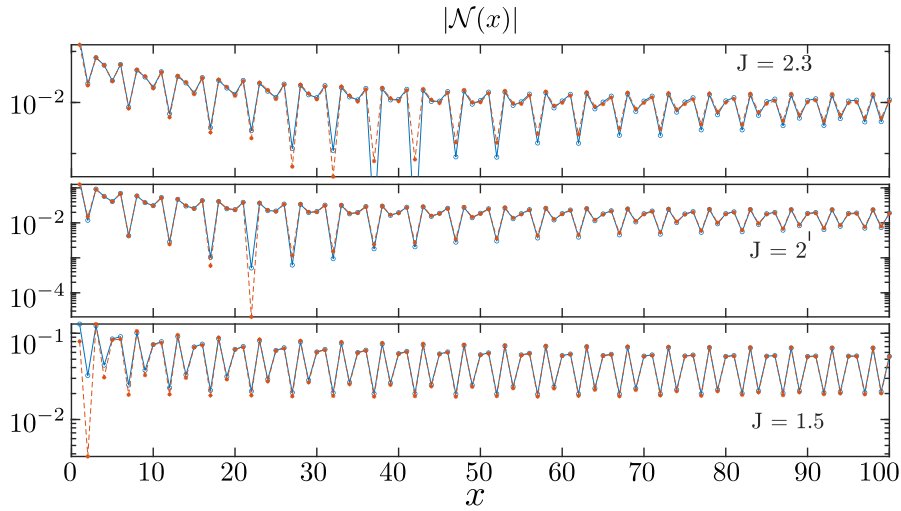


Figure 4.12: The curve fitting results for $\mathcal{N}(x)$ are shown for three different values of J : $J = 2.3$ (top), $J = 2$ (middle), and $J = 1.5$ (bottom) at $n_c = 0.8$, $N = 200$. The red stars represent the empirical data, while the blue points indicate the results of the fitting.

4. Numerical Results

At $n_c = 0.8$ the curve-fitting results for $\mathcal{N}(x)$ show a clear dependency on the coupling strength J . When J is relatively large, the fitting using Eq.(4.3) closely aligns with the data.

However, as we decrease the value of J , an unexpected decay pattern starts to emerge at the chain's end, even though the middle part of the chain can still be accurately described by Eq.(4.3).

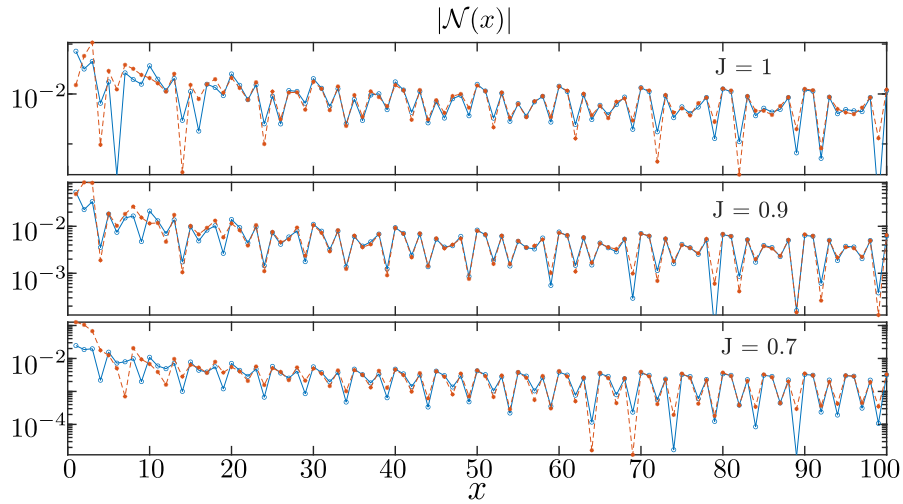


Figure 4.13: The curve fitting results for $\mathcal{N}(x)$ are displayed for three different values of J : $J = 1$ (top), $J = 0.9$ (middle), and $J = 0.7$ (bottom) at $n_c = 0.8$, $N = 200$. In these plots, the red stars represent the empirical data, while the blue points depict the results of the fitting procedure. It's evident that the fitting results in the middle of the chain match well with the data. However, as J decreases, particularly for $J = 0.7$, the fitting results at the end of the chain gradually deviate from the data.

The presence of this unusual decay can also be illustrated using the Fourier transform method. Similar to how we handled short and long-range oscillations for $\mathcal{C}(x)$, we apply Fourier transforms to different segments of $\mathcal{N}(x)$:

- (1) The full chain, where x ranges from 1 to N .
- (2) The partial chain, where we exclude the chain's ends, with x ranging from $0.1N$ to $0.9N$.

For a large coupling strength J , as depicted in Fig. 4.14, the shapes of the Fourier transform results for the full and partial chains are nearly identical. This suggests that the oscillation behaviors in the middle and at the end of the chain are universal and consistent.

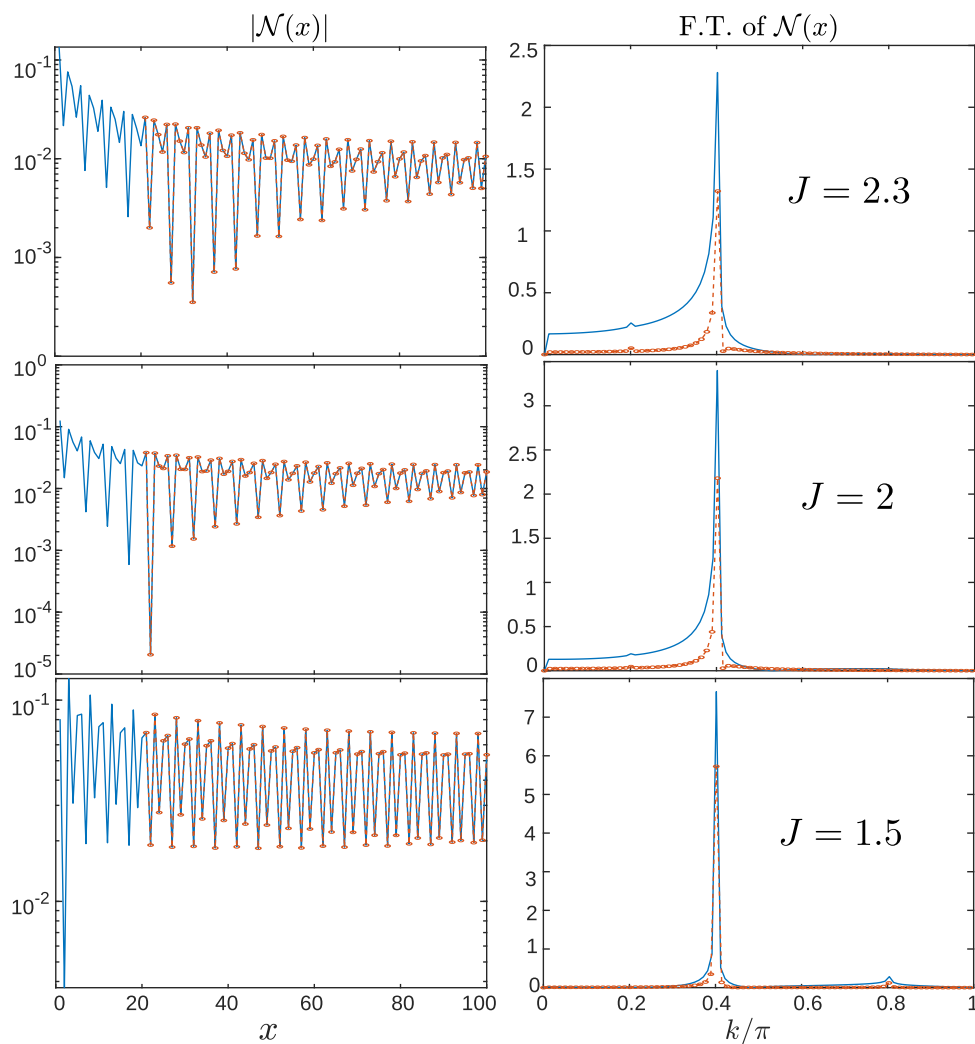


Figure 4.14: In the left panel are the $\mathcal{N}(x)$ for $J = 2.3$ (top), $J = 2$, (middle) and $J = 1.5$ (bottom) at $n_c = 0.8, N = 200$. The blue solid line represents the full chain, $x \in [1, N]$, the red dashed lines are the partial chain, $x \in [0.1N, 0.9N]$. In the right panel are their Fourier transform results for each J and the blue solid/red dashed lines depict the Fourier transform of the full/partial chain, respectively.

4. Numerical Results

As we decrease the value of J , as shown in Fig. 4.15, the shapes of the Fourier transforms for the full chain and the chain with the ends excluded become noticeably different. In the full chain Fourier transform, peaks appear at $k = 0.6\pi$ and $k = 0.8\pi$. To match this behavior, K_ρ would have to be larger than 1, which is an unphysical solution for a TL liquid.

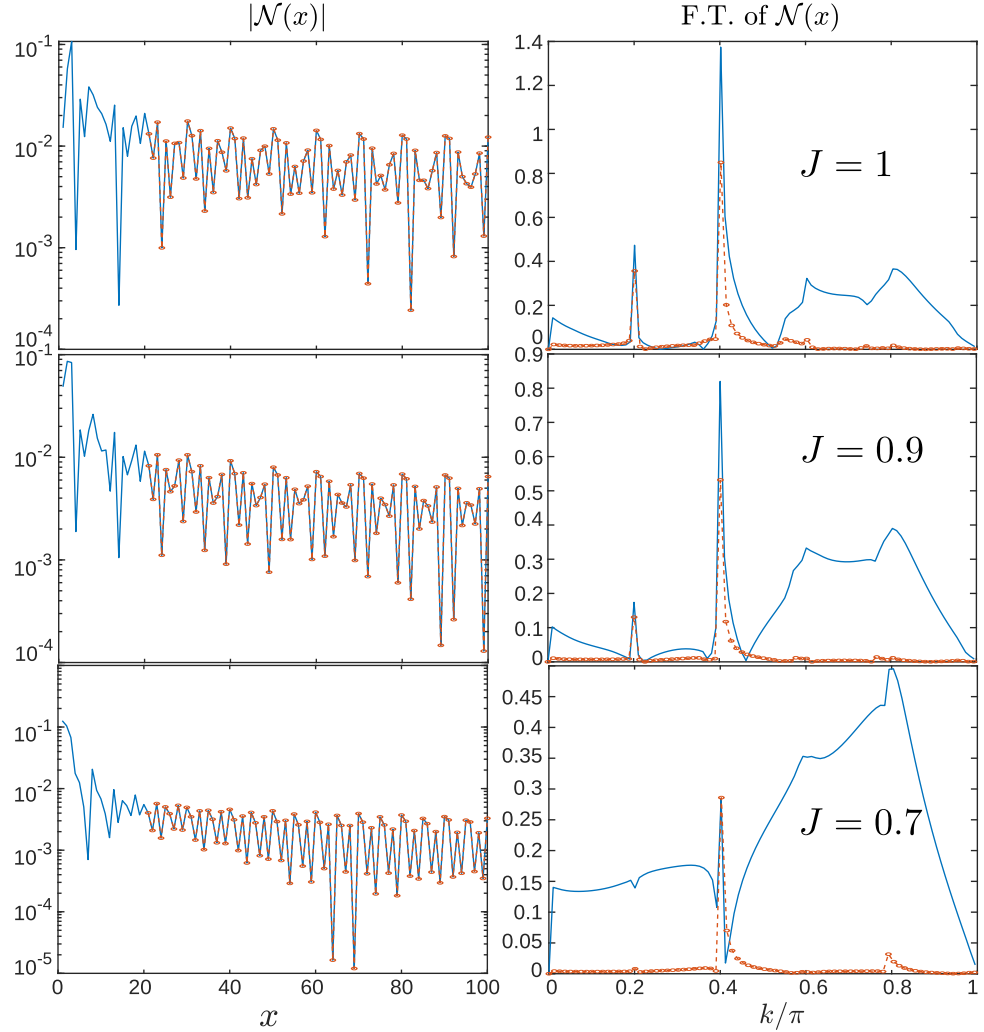


Figure 4.15: In the left panel are the $\mathcal{N}(x)$ for $J = 1$ (top), $J = 0.9$ (middle) and $J = 0.7$ (bottom) at $n_c = 0.8, N = 200$. The blue solid line represents the full chain, $x \in [1, N]$, the red dashed lines are the partial chain, $x \in [0.1N, 0.9N]$. In the right panel are their Fourier transform results for each J and the blue solid/red dashed lines depict the Fourier transform of the full/partial chain, respectively.

This unusual decay pattern, particularly evident with smaller coupling strengths, seems to indicate that open boundary effects become more pronounced in this regime. Furthermore, from Fig. 4.16, it's apparent that this effect persists even as the system size increases.

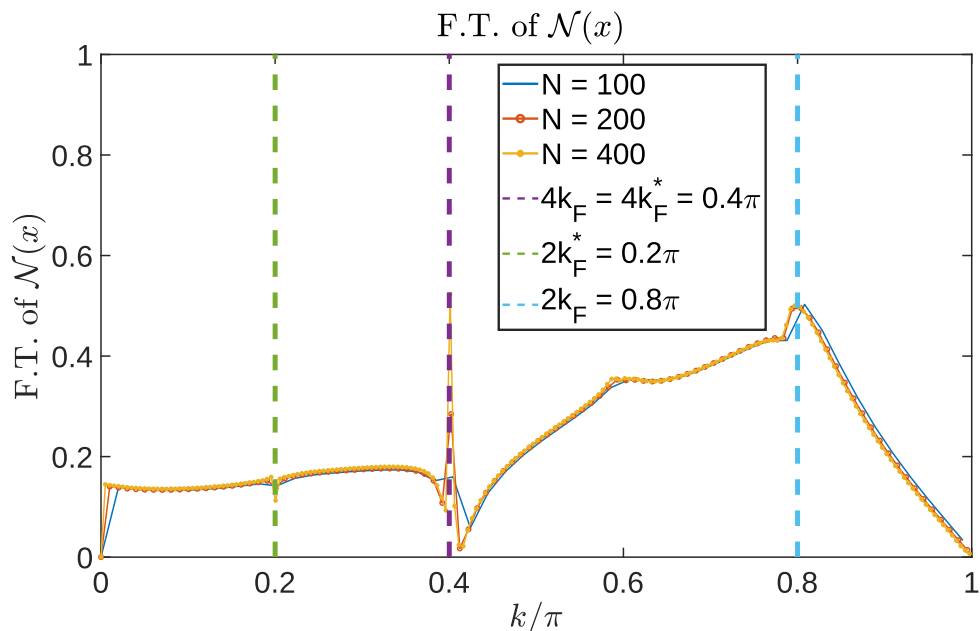


Figure 4.16: The Fourier transform results for the full chain at $J = 0.7$ and $n_c = 0.8$, with system sizes of $N = 100$ (blue curve), 200 (red curve), and 400 (orange curve), are presented in the figure. The vertical dashed lines represent $2k_F^*$ (left), $4k_F = 4k_F^*$ (middle), and $2k_F$ (right). As the system size increases, the $4k_F$ peak becomes more pronounced, while the strength of the boundary decay remains consistent. This indicates that boundary effects persist and do not diminish with increasing system size.

4. Numerical Results

At $n_c = 0.56$, the influence of boundary effects remains substantial, at low values of the coupling strength J . The exact cause of the decay at $k \neq 2k_F^*$ or $4k_F^*$ still presents a puzzle.

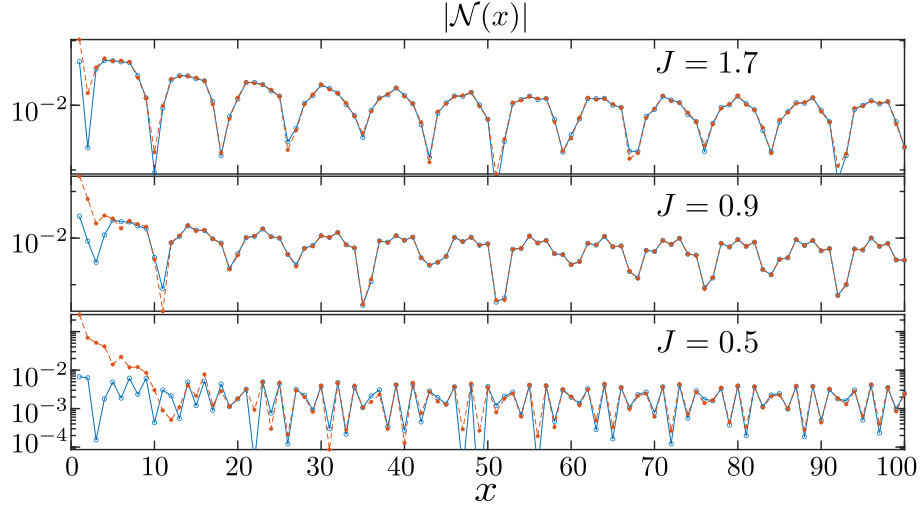


Figure 4.17: The curve fitting results for $\mathcal{N}(x)$ are displayed for three different values of J : $J = 1.7$ (top), $J = 0.9$ (middle), and $J = 0.5$ (bottom) at $n_c = 0.56$, $N = 200$. In these plots, the red stars represent the empirical data, while the blue points depict the results of the fitting procedure. Similar decay patterns as Fig. 4.14 are observed in the low J region.

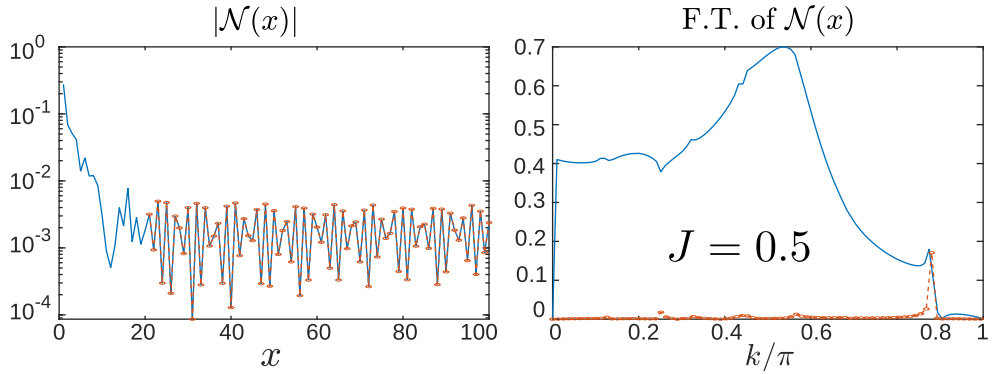


Figure 4.18: The full/partial Chains and their Fourier transforms for $J = 0.5$ at $n_c = 0.56$, $N = 200$.

$K_\rho - J$ curve When extracting the value of K_ρ from the curve-fitting results of $\mathcal{N}(x)$, the most effective approach is to exclude the chain ends to avoid boundary effects. Additionally, cross-validating these results with the curve-fitting of $\mathcal{S}(x)$ is advisable, as K_ρ also significantly influences its decay behavior.

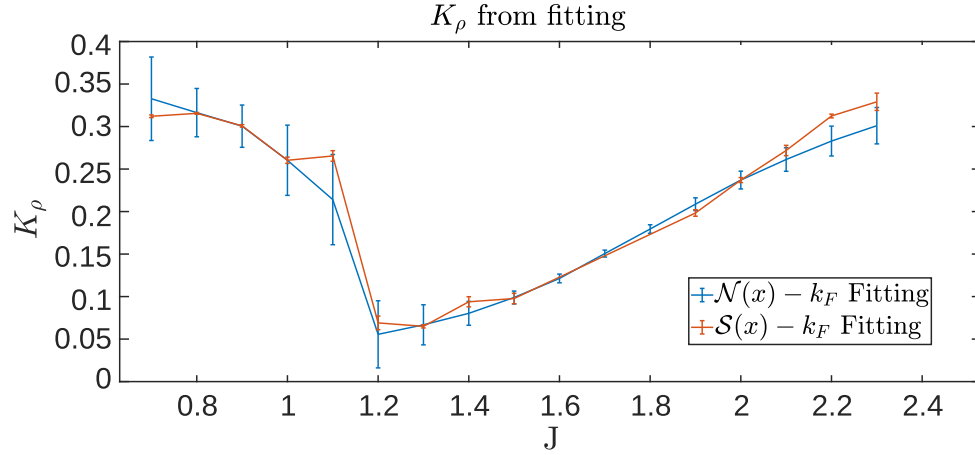


Figure 4.19: The $K_\rho - J$ from the fitting results of $\mathcal{N}(x)$ (blue) and $\mathcal{S}(x)$ (red), at $n_c = 0.8$ and $N = 200$. $J = 1.2$ is also the point where $k_F \leftrightarrow k_F^*$ happens.

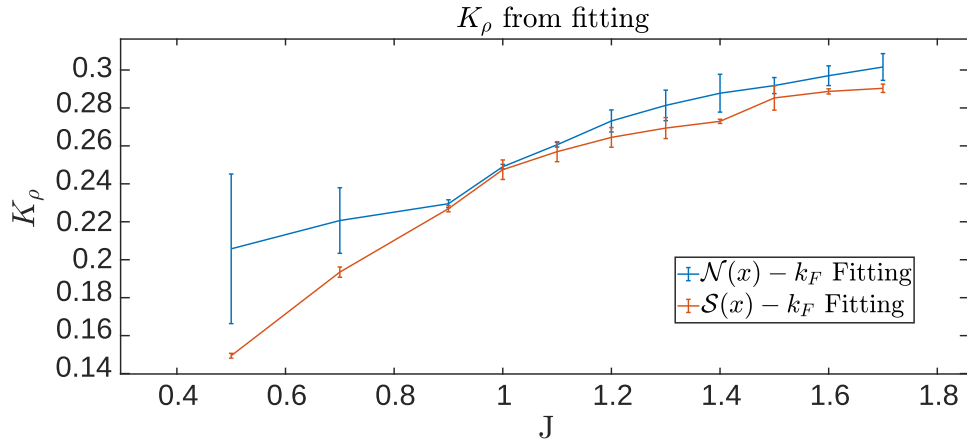


Figure 4.20: The $K_\rho - J$ from the fitting results of $\mathcal{N}(x)$ (blue) and $\mathcal{S}(x)$ (red), at $n_c = 0.56$ and $N = 200$. K_ρ decreased monotonically with decreasing J

4.4 Phenomenological Explanation Of Numerical Results

The discussion in Section 2.3 highlights the complexity of the Fermi wave vector in 1D KLM. In the large J limit, the Fermi wave vector is associated with a large filled Fermi sea picture. However, as we move away from this limit, the situation becomes less clear.

A possible resolution to this ambiguity is presented in the case where $|J| \ll E_F$. In this scenario, near commensurate band filling, a collinear metal phase emerges. This metallic phase is characterized by its electronic behavior being influenced by a spin configuration that is close to a collinear arrangement, which is connected to the heavy Tomonaga-Luttinger liquid (HTLL) phase through electron-spin interactions. At generic band fillings, a helical metal phase characterized by a $4k_F$ charge-density wave appears, and a local helical gap becomes evident [35, 36].

Numerical investigations have also contributed to our understanding. For instance, various numerical results have shown that in the small J region, a small Fermi wave vector is observed [7, 8, 12]. It's important to note that there is no readily available analytical solution for the case where J is on the order of the hopping amplitude t , and there have been no prior studies on the transition from k_F to k_F^* in this context.

In reference to Gulácsi et al. (Ref. [79]), they divided the paramagnetic phase into two distinct regions, which are separated by the FM2 region. The upper part, characterized by larger J , is described as a weakly disordered polaronic liquid with an assumed large Fermi wave vector. In contrast, the lower part, associated with smaller J values, is labeled as a strongly disordered conventional paramagnet with an assumed small Fermi wave vector.

In Ref. [8], the second FM region is noted to serve as a boundary distinguishing regions with large and small Fermi surfaces. However, the results of this project indicate something intriguing. At $n_c = 0.8$, as the value of J decreases, the Fermi wave vector continues to include the local spin even after crossing the FM2 region. Simultaneously, changes in the Fermi wave vector are observed in regions with a smaller density of conduction electrons ($n_c = 0.56$) that do not cross the FM2 region. This suggests that the changes in the Fermi wave vector are not solely dependent on the presence of the FM2 region and related phase transition, but are influenced by other factors.

An important factor that might be influencing these observations is the presence of $4k_F$ charge-density waves (CDW), which have been observed in regions with both large and small Fermi wave vectors.

In the case of commensurate band filling, the CDW is associated with a finite energy gap when the electron density $n_c = 0.75$ and $J \sim 1$ [41]. Interestingly, this is close to the transient point observed in our system.

To gain a deeper understanding, further investigation is needed, including system size extrapolation, to determine whether the CDW arises due to the

open boundary conditions or if it is an intrinsic property of the system at that parameters.

Regarding the behavior of the Luttinger parameter K_ρ in the TLL of the 1D Kondo lattice model, it has been observed to exhibit a monotonic decrease as the coupling constant J decreases while keeping the electron density fixed, as shown in Ref.[10, 28]. This decrease indicates a strong repulsive interaction between electrons in the weak-coupling region.

However, in the calculations of this thesis, an unusual inflexion point in K_ρ is observed at $J = 1.2, n_c = 0.8$. One possible explanation for this discrepancy is related to the limit as J approaches zero: in this limit, the system should ideally revert to a free 1D electron gas with $k_\rho = 1$. Therefore, the critical point which identified at $n_c = 0.8$ and $J = 1.2$ might represent such special case. But the monotonic decrease of K_ρ at $n_c = 0.56$ need further investigation.

The theorem discussed in Ref. [6] predicts the presence of a large Fermi wave vector in translation-invariant systems. However, the emergence of a CDW can break translational symmetry, potentially challenging the applicability of this theorem. Enlarging the system to infinity offers a way to mitigate CDW effects and approach a more translation-invariant scenario. This approach might make the theorem applicable and provide valuable insights into the system's behavior.

In analyzing single-particle excitation $\langle \hat{c}_i^\dagger \hat{c}_j \rangle$, we encounter a interplay of multiple oscillations, which presents a perplexing challenge. Within this region, distinguishing the distinct influences of the Kondo effect, RKKY interaction, and double exchange interaction becomes intricate. To shed light on these intertwined factors, a potential strategy involves reducing the density of local spins, thereby mitigating the impact of the RKKY interaction in this particular domain. The hypothesis is that by modulating the transient region as we alter parameters, a clearer and more discernible configuration may emerge.

Summary and outlook

Summary

In this thesis, we utilized Density Matrix Renormalization Group (DMRG) to investigate the one-dimensional Kondo lattice model, harnessed the QS-space tensor library to control quantum numbers within specific sectors and employed the controlled bond expansion DMRG method for efficient ground state determination.

Our exploration of the phase diagram of the 1D Kondo lattice model has unveiled many new and novel phenomena. We focused on two parameter sets: (1) $n_c = 0.8, 0.7 \leq J \leq 2.3$, (2) $n_c = 0.56, 0.3 \leq J \leq 1.7$, as shown in phase diagram Fig. 2.3.

The Fermi wave vector change $k_F^* \propto n_c + 1 \leftrightarrow k_F \propto n_c$, is assumed to associate with the $PM - FM - PM$ transition in (1) in Ref. [8]. This assumption is disproved by the numerical results of this thesis, by confirming that the point the Fermi wave vector change J_c is actually lower than ferromagnetic phase region.

We obtained the paramagnetic state $|PM\rangle$ for parameters (1) and (2), and subsequently computed the correlation functions (a) $\langle c_i^\dagger c_i \rangle$, (b) $\langle c_i^\dagger c_j \rangle$ and (c) $\langle \mathbf{S}_i \mathbf{S}_j \rangle$. The curve fitting and Fourier transform techniques are employed to analyze the decay and oscillations within these correlations, mutually validating our results.

The short-range oscillations in correlations ($|i - j| \approx 1 \sim 20$), consistently involve a small Fermi wave vector, regardless of J . These oscillations decay rapidly. In contrast, long-range correlations exhibit distinct behaviors, serving as the focal point for the physics explored in this thesis.

The correlation functions (b) and (c) are described by Eq. (4.16) and Eq. (4.17), respectively. These equations differ from the general Luttinger liquid solutions Eq. (4.1) and Eq. (4.2), which typically involve only a single oscillation term with $k = k_F^*$ or $k = k_F$. The results revealed, the coexistence of several oscillation terms represented by n wave vectors $k_n^{(c)}$ and $k_n^{(s)}$ ($n \leq 3$).

Analyzing these results through Fourier transform, in the charge sector we observe that at low J , a single peak is located at k_F . As J increases, the single peak transforms into a sequence of peaks in single-particle excitation (b). The details are shown in Tab. 4.1 for parameters (1) and Tab. 4.2 for parameters (2). An ambiguous transient phase region emerges between the domains of large and small Fermi wave vectors, as graphical representations provided in Fig.4.7 and Fig.4.11.

In the spin sector, a clear transition between large and small Fermi wave vectors is evident in both parameter sets, contrasting with the charge sector.

The charge density oscillation (a) provides a means to validate the K_ρ obtained from the curve fitting of (c), as K_ρ is crucial in both cases. The comparison of these two fitting results is depicted in Fig. 4.19. Both results indicate a kink at $J = 1.2, n_c = 0.8$, which corresponds to the onset of the ambiguous region in the charge sector and the transition between small and large Fermi wave vectors in the spin sector.

Outlook

This thesis has laid the foundation for several intriguing research directions:

- Oshikawa’s Theorem [6] and Localized Spins: As mentioned in Sec. 2.3, through the LSM theorem, a large Fermi surface in 1D KLM is promised for system with certain symmetries. Expanding system size and addressing finite size effects or employing methods like variational uniform matrix product states (VUMPS) [80] for infinite systems may clarify the phenomena.
- Unexplained Peaks and Coexistence of k_F and k_F^* : Peaks not aligning with k_F or k_F^* and the coexistence of these wave vectors pose intriguing questions. To explore Fermi surface intricacies further, varying local spin density as a potential avenue for investigation may offer insights into how localized spins behave within the Kondo lattice model,
- Interpreting Coefficients α and β : Coefficients α and β remain enigmatic. Understanding their physical meaning and their role in identifying phases or transitions requires further theoretical work.
- Differences Between $n_c = 0.8$ and $n_c = 0.56$: While the outcomes for these two conduction electron densities exhibit notable distinctions, their universality is suggested by the phase diagram. Further calculations are necessary to bridge the gap between these parameter sets and elucidate how the crucial coefficients evolve.
- Boundary Effects: We’ve observed an unexpected decay in charge density oscillation at low J , primarily at the chain’s ends. This suggests boundary effects, and the specific oscillation wave vectors need further investigation.
- Long/Short Range Oscillation: The short-range oscillations with respect to k_F are system size-independent, as ensured by our methodology

for averaging correlations, although these patterns bear resemblance to boundary effects. They potentially represent an intrinsic property of correlations. Further explanation and analytical analysis are required to understand this phenomenon.

- Possible gap: The characteristic length of convergence, denoted as λ , should ideally exceed the system size if the system is gapless under certain parameters. However, based on the extrapolation results, it appears that this condition is not met. Therefore, conducting an additional check for energy could be valuable and may provide further insights.

Appendix 1: Tensor Network Basics and Notations

This section is largely quoted from the tensor network lecture notes from Prof. Jan von Delft [65], aims to clarify the visual representation of tensors and the process of tensor contraction, illustrate the basic idea of Matrix Product States (MPS), Matrix Product Operator (MPO) and the process of Density Matrix Renormalization Group (DMRG).

Tensor network methods often involve intricate manipulations of multidimensional tensors. Representing these operations using traditional mathematical equations can lead to lengthy formulas crowded with numerous tensor indices. Furthermore, the interpretation of certain two-dimensional tensor expressions might become less clear when written linearly. To address this challenge, similar to the use of Feynman diagrams in perturbation theories, diagrammatic notations are adopted for tensor networks. These graphical representations effectively alleviate the complexity of traditional equations, providing a more intuitive approach for comprehending and working with intricate tensor operations.

A.1 Tensor Network Basics

Tensor, Contraction and the Cost

Tensor network diagrams are typically composed of geometric shapes like circles or rectangles, connected by lines. In these diagrams, each circle represents a tensor, and the lines extending from the circle correspond to the tensor's indices. For instance, in Fig. A.1, examples of rank-1 tensor (vector), rank-2 tensor (matrix), and rank-3 tensor are illustrated.

Within tensor network diagrams, index positions on tensors are often indicated by arrows. These arrows serve to distinguish different types of indices and their positions. Specifically, incoming arrows usually signify contravariant indices, while outgoing arrows indicate covariant indices.

A. Appendix 1: Tensor Network Basics and Notations

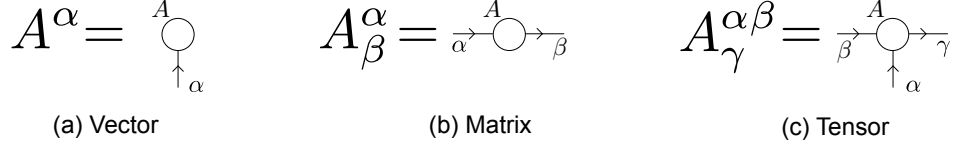


Figure A.1: The diagrammatic representation of vectors, matrices, and rank-3 tensors involves circles symbolizing tensors. Each external line, often referred to as a "leg" or "bond", corresponds to an index of the tensor.

Graphically, tensor contraction is achieved by connecting lines in the tensor network diagrams that correspond to the same index. This linking of lines represents the mathematical operation of summation or contraction over those indices.

$$\sum_{\beta} A_{\beta}^{\alpha} B_{\gamma}^{\beta} = \begin{array}{c} \text{A} \\ \circ \\ \xrightarrow{\alpha} \quad \xrightarrow{\beta} \quad \xrightarrow{\gamma} \end{array} = \begin{array}{c} \text{A} \\ \circ \\ \xrightarrow{\alpha} \quad \xrightarrow{\beta} \quad \xrightarrow{\gamma} \end{array} = \begin{array}{c} \text{C} \\ \circ \\ \xrightarrow{\alpha} \quad \xrightarrow{\gamma} \end{array} = C_{\gamma}^{\alpha}$$

Figure A.2: A contraction operation on index β is graphically depicted by connecting the lines that represent this index, which signifies the contraction between tensors. While indices are labeled in the diagram for clarity, they can be omitted in practical applications, streamlining the visual representation.

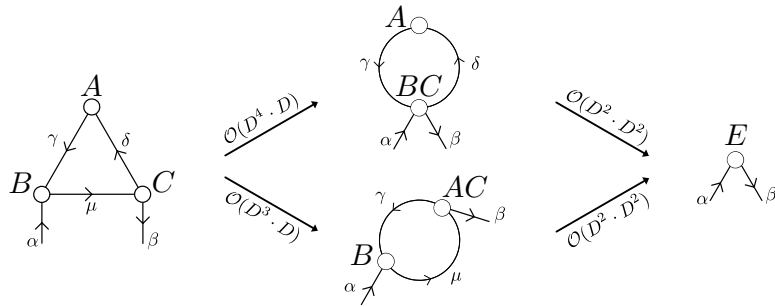


Figure A.3: Assuming uniform dimensions D for all legs, the total numerical cost varies when contracting legs in different orders. The expense of contracting μ first surpasses that of contracting δ first. In the upper approach, $A_{\gamma}^{\delta} B_{\mu}^{\gamma\alpha} C_{\beta\delta}^{\mu} \rightarrow A_{\gamma}^{\delta} (BC)_{\beta\delta}^{\gamma\alpha} \rightarrow E_{\beta}^{\alpha}$, the total cost is $\mathcal{O}(D^5)$. In the lower approach, $A_{\gamma}^{\delta} B_{\mu}^{\gamma\alpha} C_{\beta\delta}^{\mu} \rightarrow B_{\mu}^{\gamma\alpha} (AC)_{\beta\gamma}^{\mu} \rightarrow E_{\beta}^{\alpha}$ the total cost is $\mathcal{O}(D^4)$.

A tensor network can involve multiple contraction operations, and the sequence in which these contractions are performed doesn't affect the final results. However, the order of contractions does influence the computational complexity of the algorithm. This complexity is visually evident from the tensor diagrams. For example, in the contraction shown in Fig. A.2, the computational effort can be roughly estimated as $O(D[\alpha]D[\beta]D[\gamma])$, where $D[i]$ represents the dimension of index i .

Generally, the computational complexity is the product of the dimensions of all lines in the diagram. However, depending on the diagram's structure, the actual computational cost might vary based on the order in which contractions are performed.

Unitaries, Isometries and Decompositions

A square matrix $U \in \text{mat}(D, D; \mathbb{C})$ is considered unitary if it satisfies the condition

$$U^\dagger U = U U^\dagger = \mathbb{I}_D \quad (\text{A.1})$$

where \mathbb{I}_D is the identity matrix of size D . Unitary transformations denote linear transformations that uphold the inner product and vector norm.

For rectangular matrices, let $A \in \text{mat}(D, D'; \mathbb{C})$ with $D \geq D'$ be termed a "left isometry" if

$$A^\dagger A = \mathbb{I}_{D'} \text{ and } A A^\dagger \neq \mathbb{I}_D \quad (\text{A.2})$$

Correspondingly, consider a rectangular matrix $B \in \text{mat}(D, D'; \mathbb{C})$ with $D \leq D'$ as a "right isometry" if

$$B B^\dagger = \mathbb{I}_D \text{ and } B^\dagger B \neq \mathbb{I}_{D'} \quad (\text{A.3})$$

In linear algebra, the concept of an isometry pertains to a linear transformation that maintains the length or norm of vectors. Within the framework of tensor networks, an isometric tensor is characterized by having fewer outgoing legs compared to incoming legs. This arrangement ensures that the tensor retains its capacity to preserve vector norms during contractions within the tensor network. This property is particularly crucial in the context of techniques like DMRG.

Furthermore, isometric tensors play a significant role in effectively representing quantum states and operators within tensor networks. They facilitate the compression and truncation of tensor network descriptions while still capturing essential characteristics of the quantum state or operator. This compression becomes especially valuable when dealing with systems that possess numerous degrees of freedom, as explicit tensor representations can quickly become computationally unwieldy.

In the context of tensor networks, any matrix can be employed to construct left or right isometric tensors through the process of singular value decomposition.

$$\begin{aligned}
U = D \begin{array}{|c|} \hline \text{---} \\ \hline \end{array} & \quad D \begin{array}{|c|} \hline \text{---} \\ \hline \end{array} \cdot D \begin{array}{|c|} \hline \text{---} \\ \hline \end{array} = D \begin{array}{|c|} \hline \text{---} \\ \hline \end{array} \cdot D \begin{array}{|c|} \hline \text{---} \\ \hline \end{array} = D \begin{array}{|c|} \hline \diagdown \\ \hline \end{array} \\
& \quad U^\dagger U = U U^\dagger = \mathbb{I}_D \\
\\
A = D \begin{array}{|c|} \hline \text{---} \\ \hline \end{array} & \quad D \begin{array}{|c|} \hline \text{---} \\ \hline \end{array} \cdot D \begin{array}{|c|} \hline \text{---} \\ \hline \end{array} = D \begin{array}{|c|} \hline \diagdown \\ \hline \end{array} \quad D \begin{array}{|c|} \hline \text{---} \\ \hline \end{array} \cdot D \begin{array}{|c|} \hline \text{---} \\ \hline \end{array} = D \begin{array}{|c|} \hline \text{---} \\ \hline \end{array} \\
& \quad A^\dagger A = \mathbb{I}_{D'} \quad AA^\dagger \neq \mathbb{I}_D \\
\\
B = D \begin{array}{|c|} \hline \text{---} \\ \hline \end{array} & \quad D \begin{array}{|c|} \hline \text{---} \\ \hline \end{array} \cdot D \begin{array}{|c|} \hline \text{---} \\ \hline \end{array} = D \begin{array}{|c|} \hline \diagdown \\ \hline \end{array} \quad D \begin{array}{|c|} \hline \text{---} \\ \hline \end{array} \cdot D \begin{array}{|c|} \hline \text{---} \\ \hline \end{array} = D \begin{array}{|c|} \hline \text{---} \\ \hline \end{array} \\
& \quad BB^\dagger = \mathbb{I}_D \quad B^\dagger B \neq \mathbb{I}_{D'}
\end{aligned}$$

Figure A.4: The diagrammatic representation of unitary and left/right isometry matrix.

Consider a matrix $M \in \text{mat}(D, D'; \mathbb{C})$, and let $\tilde{D} = \min(D, D')$, then any such M has a singular value decomposition of the form:

$$M = U S V^\dagger \tag{A.4}$$

where $U \in \text{mat}(D, \tilde{D}; \mathbb{C})$, $U^\dagger U = \mathbb{I}_{\tilde{D}}$; $V^\dagger \in \text{mat}(\tilde{D}, D'; \mathbb{C})$, $V^\dagger V = \mathbb{I}_{\tilde{D}}$.

$$\begin{aligned}
D \leq D': \quad D \begin{array}{|c|} \hline \text{---} \\ \hline \end{array} & = D \begin{array}{|c|} \hline \text{---} \\ \hline \end{array} \begin{array}{|c|} \hline \diagdown \\ \hline \end{array} \begin{array}{|c|} \hline \text{---} \\ \hline \end{array} \\
& \quad M = U \quad S \quad V^\dagger \\
\\
D \geq D': \quad D \begin{array}{|c|} \hline \text{---} \\ \hline \end{array} & = D \begin{array}{|c|} \hline \text{---} \\ \hline \end{array} \begin{array}{|c|} \hline \diagdown \\ \hline \end{array} \begin{array}{|c|} \hline \text{---} \\ \hline \end{array}
\end{aligned}$$

Figure A.5: The diagrammatic representation of SVD for matrix M .

The singular value matrix $S \in \text{mat}(\tilde{D}, \tilde{D}; \mathbb{C})$ takes on a diagonal structure, consisting solely of non-negative diagonal elements. These elements constitute

the Schmidt rank r , indicating the count of non-zero singular values. The diagonal entries can be ordered in a descending fashion:

$$s_1 \geq s_2 \geq \dots \geq s_r > 0 \rightarrow S = \text{diag}(s_1, s_2, \dots, s_r, 0, \dots, 0) \quad (\text{A.5})$$

The number of zeros within the diagonal is $\tilde{D} - r$.

SVD can be used to approximate a rank r matrix M by a rank $r' (< r)$ matrix M' :

$$\begin{aligned} M &= USV^\dagger \rightarrow M' = US'V^\dagger \\ S &= \text{diag}(s_1, s_2, \dots, s_r, 0, \dots, 0), \text{num}(0) = \tilde{D} - r \\ &\rightarrow S' = \text{diag}(s_1, s_2, \dots, s_{r'}, 0, \dots, 0), \text{num}(0) = \tilde{D} - r' \end{aligned} \quad (\text{A.6})$$

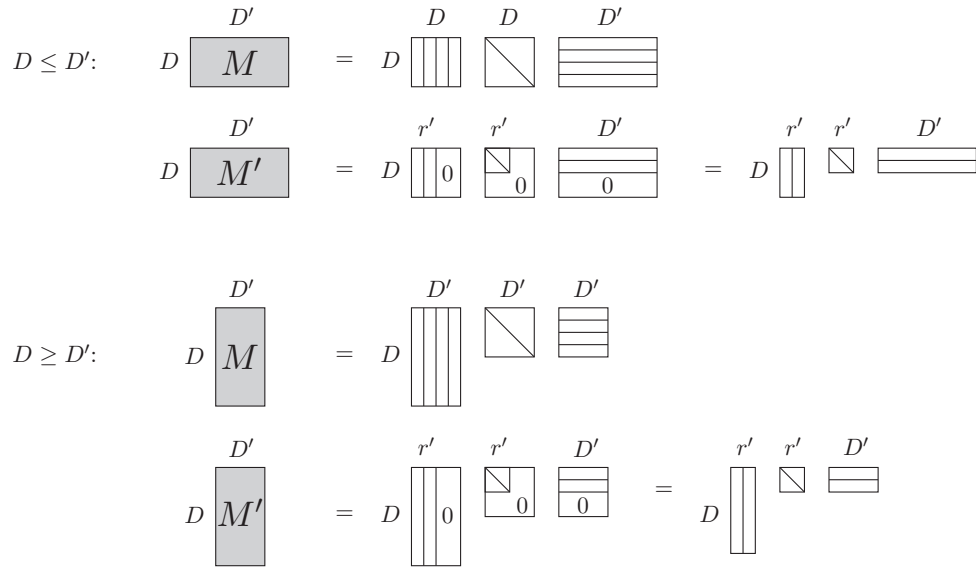


Figure A.6: The diagrammatic representation of SVD truncation process.

Applying Singular Value Decomposition (SVD) and truncation within the DMRG framework provides a practical approach to efficiently handle complex quantum states with significant entanglement. In doing so, DMRG preserves the essential aspects of these states while discarding less impactful details. This blending of techniques empowers DMRG as a versatile and powerful methodology.

The success of DMRG largely relies on the methods chosen for executing truncation, a subject which is elaborated in the Sec.3.2.

Entanglement and the Area Law

Entanglement plays a critical role in the domain of tensor networks, especially when it comes to capturing and representing complex quantum states. In the context of quantum systems, entanglement signifies the non-classical correlations that link different aspects of a composite system. In tensor networks, measures of entanglement are used to assess the degree to which information is shared among different tensors or sites within the network.

Tensor network methodologies, as demonstrated by DMRG, leverage the concept of entanglement to effectively model and manipulate quantum states. Excessive entanglement can make explicit representations of quantum states computationally challenging. However, tensor networks provide a solution by encapsulating the essential characteristics of these states while discarding less significant details. Techniques based on entanglement-driven compression and truncation enable a resource-efficient approximation of quantum states, while still maintaining their essential features.

Moreover, entanglement provides valuable insights into the behavior and properties of quantum systems. Its implications extend to phenomena such as quantum phase transitions and criticality. The distribution of entanglement across a system's degrees of freedom can reveal crucial information about the system's fundamental state and excitations.

The ground state entanglement entropy follows an area law [81–83], which is a fundamental concept in quantum physics. This law provides deep insights into the entanglement organization within many-body systems.

For a pure quantum system in pure state $|\psi\rangle$, with density matrix $\hat{\rho} = |\psi\rangle\langle\psi|$, it can be divided into two parts: A/B , the Hilbert spaces of two subsystems are:

$$\mathbb{H}_A = \text{span}\{|\vec{\sigma}_A\rangle\} \ , \ \mathbb{H}_B = \text{span}\{|\vec{\sigma}_B\rangle\} \quad (\text{A.7})$$

To obtain the reduced density matrix of A/B, we trace out B/A:

$$\hat{\rho}_A = \text{Tr}_B \hat{\rho} \ , \ \hat{\rho}_B = \text{Tr}_A \hat{\rho} \quad (\text{A.8})$$

and the entanglement entropy of A/B is

$$\mathcal{S}_A = -\text{Tr}_A \hat{\rho}_A \log_2 \hat{\rho}_A \ , \ \mathcal{S}_B = -\text{Tr}_B \hat{\rho}_B \log_2 \hat{\rho}_B \quad (\text{A.9})$$

Then the entanglement of two systems is described by the area law:

$$\mathcal{S} = \mathcal{S}_{A/B} \sim \partial V \quad (\text{A.10})$$

∂V is the boundary area of the subsystem.

The area law establishes that the entanglement entropy, which measures quantum entanglement between different parts of a system, increases proportionally to the boundary area of the analyzed region, rather than its volume. In

other words, the entanglement entropy grows with the surface area surrounding a subsystem, not its size.

This principle is pivotal within tensor network methods. Tensor networks leverage the area law to accurately model and represent quantum states, particularly those with limited entanglement. Thus, when entanglement is confined or displays low-dimensionality, tensor networks can offer precise approximations using fewer computational resources compared to alternative methods. By prioritizing entanglement across boundaries, tensor networks maintain precision while minimizing parameters needed for a comprehensive quantum state representation. This feature renders tensor networks, including Matrix Product States (MPS) as used in DMRG, highly valuable for simulating intricate quantum systems, notably in the domain of condensed matter physics.

Various Canonical MPS Forms

The matrix products in tensor network have gauge freedom, which means any matrix product can be expressed in infinitely many ways without changing the product:

$$MM' = M(UU^{-1})M' = \tilde{M}\tilde{M}' \quad (\text{A.11})$$

Gauge freedom can be exploited to reshape MPSs into particularly convenient, canonical forms.

The SVD process entails truncating the matrix S by retaining only the largest D singular values. Subsequently, the truncated version of matrix U is used as the updated form of A , and the truncated tensors S' and V^\dagger are contracted with the succeeding tensor.

Left-canonical MPS: All tensors are left normalized, denoted A ,

$$|\Psi_\alpha\rangle_{\mathcal{L}} = |\vec{\sigma}\rangle_{\mathcal{L}} [A_1^{\sigma_1} \dots A_{\mathcal{L}}^{\sigma_{\mathcal{L}}}]_\alpha^1 \quad (\text{A.12})$$

$A^\dagger A = \mathbb{I}$, and these states form an orthonormal set: in general, $\forall_l \subset \mathbb{H}^l$, ${}_l\langle\Psi^{\alpha'}|\Psi_\alpha\rangle_l = \mathbb{I}_\alpha^{\alpha'}$.

Right-canonical MPS: All tensors are right normalized, denoted B ,

$$|\Phi_\beta\rangle_{\mathcal{L}} = |\vec{\sigma}\rangle_{\mathcal{L}} [B_1^{\sigma_1} \dots B_{\mathcal{L}}^{\sigma_{\mathcal{L}}}]_\beta^1 \quad (\text{A.13})$$

$BB^\dagger = \mathbb{I}$, and these states form an orthonormal set: in general, $\forall_l \subset \mathbb{H}^l$, ${}_l\langle\Phi^{\beta'}|\Phi_\beta\rangle_l = \mathbb{I}_\beta^{\beta'}$.

A. Appendix 1: Tensor Network Basics and Notations

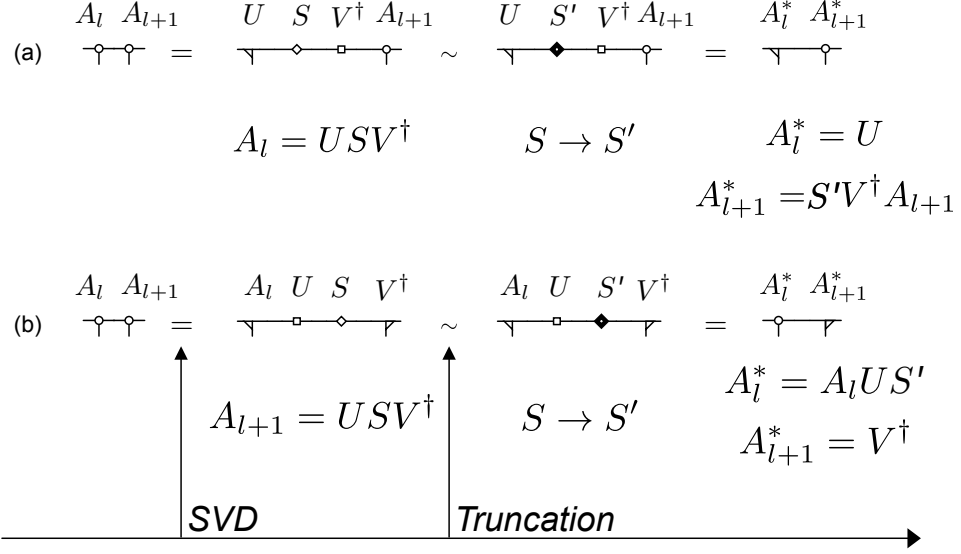


Figure A.7: The process involves truncating the MPS by applying SVD to a specific tensor and discarding unnecessary singular values.

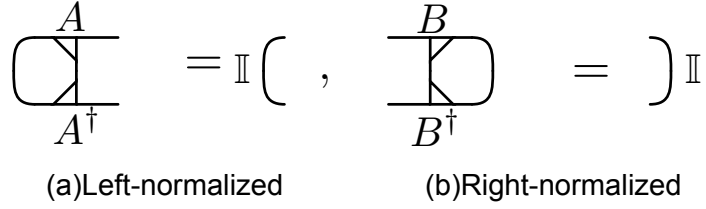


Figure A.8: Left-normalized and right-normalized tensor. Both of them are constructed by SVD, where \mathbb{I} represents the identity matrix. In the subsequent diagram, triangles are employed to represent left/right normalized tensors. And the circles are omitted.

Site-canonical MPS: The tensors are left-normalized to left of site l , and right-normalized to right of site l .

$$\begin{aligned} |\Psi\rangle &= |\vec{\sigma}\rangle_{\mathcal{L}} [A_1^{\sigma_1} \dots A_{l-1}^{\sigma_{l-1}}]_{\alpha} [M_l]^{\alpha\sigma_l\beta} [B_{l+1}^{\sigma_{l+1}} \dots B_{\mathcal{L}}^{\sigma_{\mathcal{L}}}]_{\beta}^1 \\ &= |\Psi_{\alpha}\rangle_{l-1} |\sigma_l\rangle |\Phi_{\beta}\rangle_{l+1} [M_l]^{\alpha\sigma_l\beta} \end{aligned} \quad (\text{A.14})$$

The states $|\alpha, \sigma_l, \beta\rangle := |\Psi_{\alpha}\rangle_{l-1} |\sigma_l\rangle |\Phi_{\beta}\rangle_{l+1}$ form an orthonormal set:
 $\langle \alpha', \sigma', \beta' | \alpha, \sigma, \beta \rangle = \mathbb{I}_{\alpha}^{\alpha'} \mathbb{I}_{\sigma}^{\sigma'} \mathbb{I}_{\beta}^{\beta'}$.

Mathematically, the multiplication of two MPOs \hat{O}_1 and \hat{O}_2 can be written as:

$$\begin{aligned}\hat{O} &= [\hat{O}_1]_{\vec{\sigma}}^{\vec{\sigma}} [\hat{O}_2]_{\vec{\sigma}''}^{\vec{\sigma}'} |\vec{\sigma}'\rangle \langle \vec{\sigma}| \\ &= \left\{ \prod_{l=1}^{\mathcal{L}} [W_1]_l \right\}_{\vec{\sigma}}^{\vec{\sigma}'} \left\{ \prod_{l'=1}^{\mathcal{L}} [W_2]_{l'} \right\}_{\vec{\sigma}''}^{\vec{\sigma}'} |\vec{\sigma}'\rangle \langle \vec{\sigma}| \\ &= \left\{ \prod_{l=1}^{\mathcal{L}} \tilde{W}_l \right\}_{\vec{\sigma}}^{\vec{\sigma}'} |\vec{\sigma}'\rangle \langle \vec{\sigma}| \quad (\text{A.18})\end{aligned}$$

Here, \hat{O} is the resulting MPO after multiplication, W_1 and W_2 are the individual tensors from the original MPOs, and the summation runs over all possible indices σ_i'' :

$$[\tilde{W}_l]_{\nu'\sigma}^{\mu'\sigma'} = [[W_1]_l]_{\nu\sigma''}^{\mu\sigma'} [[W_2]_l]_{\bar{\nu}\sigma}^{\bar{\mu}\sigma''} \quad (\text{A.19})$$

with composite indices $\mu' = (\mu, \bar{\mu}), \nu' = (\nu, \bar{\nu})$ of increasing dimension $w = w_1 \cdot w_2$, w_1 and w_2 are the dimension of physical bonds σ and σ' .

The addition of two MPOs follows a process analogous to multiplication. The tensors from both MPOs are combined by adding the corresponding tensors while maintaining the integrity of the physical indices. Mathematically, the addition of two MPOs \hat{O}_1 and \hat{O}_2 can be expressed as:

$$\begin{aligned}\hat{O} &= ([\hat{O}_1]_{\vec{\sigma}}^{\vec{\sigma}} + [\hat{O}_2]_{\vec{\sigma}}^{\vec{\sigma}}) |\vec{\sigma}'\rangle \langle \vec{\sigma}| \\ &= \left(\left\{ \prod_{l=1}^{\mathcal{L}} [W_1]_l \right\}_{\vec{\sigma}}^{\vec{\sigma}'} + \left\{ \prod_{l=1}^{\mathcal{L}} [W_2]_l \right\}_{\vec{\sigma}}^{\vec{\sigma}'} \right) |\vec{\sigma}'\rangle \langle \vec{\sigma}| \\ &= [Tr \begin{pmatrix} [W_1]_1 & 0 \\ 0 & [W_2]_1 \end{pmatrix} \begin{pmatrix} [W_1]_2 & 0 \\ 0 & [W_2]_2 \end{pmatrix} \cdots \begin{pmatrix} [W_1]_{\mathcal{L}} & 0 \\ 0 & [W_2]_{\mathcal{L}} \end{pmatrix}]_{\vec{\sigma}}^{\vec{\sigma}'} |\vec{\sigma}'\rangle \langle \vec{\sigma}| \quad (\text{A.20})\end{aligned}$$

Here, \hat{O} is the resulting MPO after addition, and W_1 and W_2 are the individual tensors from the original MPOs:

$$[\tilde{W}_l]_{\sigma}^{\sigma'} = \begin{pmatrix} \prod_{l=1}^{\mathcal{L}} [W_1]_l & 0 \\ 0 & \prod_{l=1}^{\mathcal{L}} [W_2]_l \end{pmatrix}_{\sigma}^{\sigma'} \quad (\text{A.21})$$

A.2 DMRG: Iterative ground state search

One Site DMRG

Assuming the site-canonical form MPS with orthogonality center at site l and the Hamiltonian MPOs:

$$|\Psi\rangle = |\alpha\rangle|\sigma_l\rangle|\beta\rangle[M_l]^{\alpha\sigma_l\beta} \quad (\text{A.22})$$

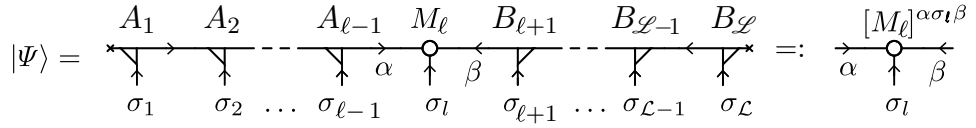


Figure A.15: The diagrammatic representation of original MPS Eq. (A.22). Assuming that this MPS has been truncated, the maximum bond dimension equals to D , the physical legs dimension is d .

$$\hat{\mathcal{H}} = |\vec{\sigma}'\rangle \left\{ \prod_{l=1}^{\mathcal{L}} W_l \right\} \frac{\vec{\sigma}'}{\vec{\sigma}} \langle \vec{\sigma} | \quad (\text{A.23})$$

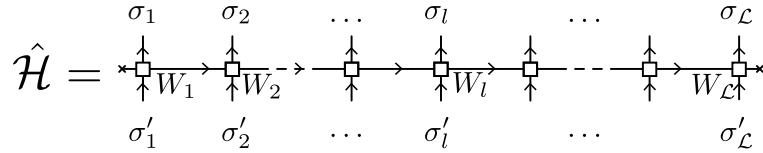


Figure A.16: The diagrammatic representation of original MPO Eq. (A.23). The virtual bond dimension of MPO is w .

In this context, our goal is to minimize the energy E of the state $|\Psi\rangle$ while satisfying the constraint of unit normalization $\langle\Psi|\Psi\rangle = 1$. The optimization of $|\Psi\rangle$ can be formulated as a Lagrangian optimization problem:

$$\min(\langle\Psi|\hat{\mathcal{H}}|\Psi\rangle - \lambda\langle\Psi|\Psi\rangle) \quad (\text{A.24})$$

where λ acts as the Lagrange multiplier.

We find the Lagrange equation to be

$$\frac{\partial}{\partial M_l^\dagger} [\langle\Psi|\hat{\mathcal{H}}|\Psi\rangle - \lambda\langle\Psi|\Psi\rangle] = 0 \quad (\text{A.25})$$

From such Lagrangian equation which can be reshaped to a linear equation system, we get the 1-site Schrödinger equation :

$$H_l^{(1)}\psi_l^{(1)} = \lambda\psi_l^{(1)} \quad (\text{A.26})$$

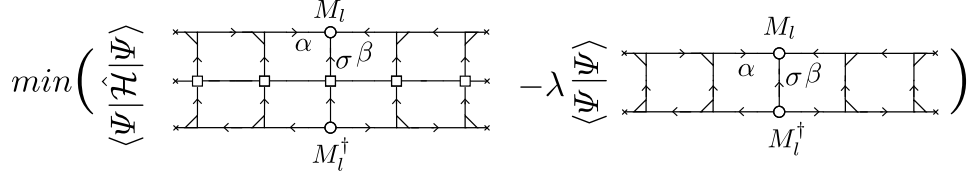


Figure A.17: The diagrammatic representation of Langrangian optimization of $|\Psi\rangle$ Eq. (A.24).

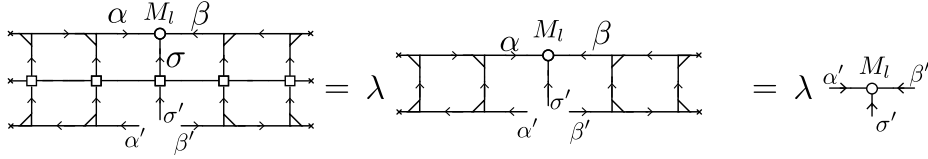


Figure A.18: The diagrammatic representation of Langrangian equation Eq. (A.25).

where $\psi_l^{(1)} = M_l$ with normalization $[\psi_l^{(1)}]^\dagger \psi_l^{(1)} = 1$.

The tensor M_l can be conceptualized as a vector, labeled by the composite index $a' = (\alpha' \sigma' \beta')$, while $H_l^{(1)}$ is considered as a matrix:

$$[H_l^{(1)}]_a^{a'} [M_l]^a = \lambda [M_l]^{a'} \quad (\text{A.27})$$

with normalization $[M_l^\dagger]_a [M_l]^a = 1$.

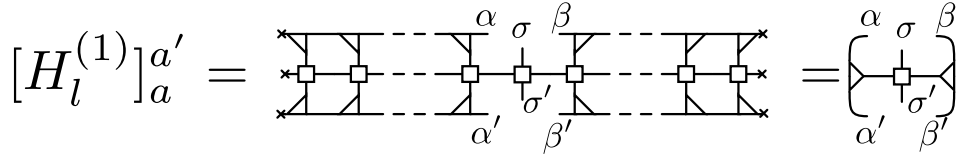


Figure A.19: The diagrammatic representation of one-site Hamiltonian.

Solving Eq. (A.27) using an eigensolver will yield a new matrix \tilde{M}_l along with the corresponding eigenvalue λ , which approximates the ground state energy. This new \tilde{M}_l is then employed to update the MPS as $M_l \rightarrow \tilde{M}_l$. Moving to the next site, the SVD is applied to \tilde{M}_l to shift the orthogonality center to site $l + 1$. This entire process is repeated for the subsequent site.

The optimization of the MPS can commence from an arbitrary state that may be distant from the actual ground state initially. By iteratively optimizing the MPS and performing sweeps back and forth, convergence is achieved when the ground state energy remains unchanged with respect to a fixed bond dimension D .

A. Appendix 1: Tensor Network Basics and Notations

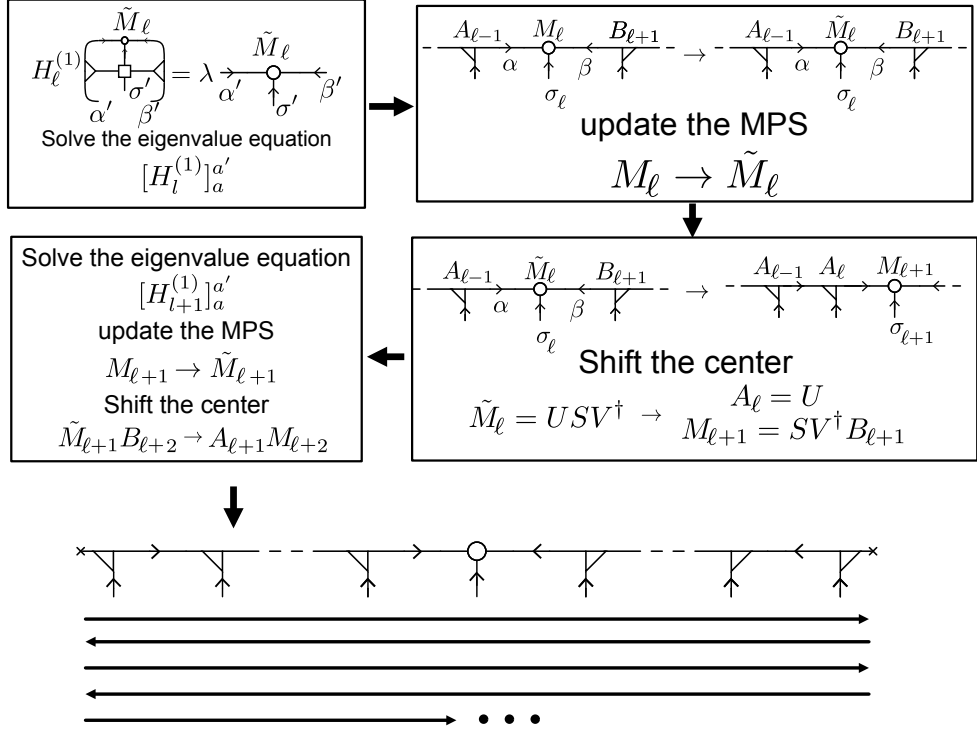


Figure A.20: The diagrammatic representation of DMRG process, iteratively optimize the MPS to the ground state.

The matrix dimensions of $H_l^{(1)}$ are typically of the order $D^2 d \times D^2 d$, which can be large. Consequently, a numerical technique like the Lanczos iterative solver [68–71], which targets the lowest eigenvalue of the system, is employed. Ensuring an efficient implementation of the eigensolver is crucial due to its frequent occurrence within a single ground state search: Number of solved eigenequations = Sweeps \times Sites.

Two Site DMRG

The MPS in site-canonical two-site basis is :

$$|\Psi\rangle = |\Psi_\alpha\rangle_{l-1} |\sigma_l\rangle |\sigma_{l+1}\rangle |\Phi_\beta\rangle_{l+2} [M_l]^{\alpha\sigma_l\gamma} [B_{L+1}]_\gamma^{\beta\sigma_{l+1}} \quad (\text{A.28})$$

The basic logic of two-site DMRG is exactly the same as one-site DMRG, starts with the Langrangian optimization for two sites:

$$\frac{\partial}{\partial B_{l+1}^\dagger} \frac{\partial}{\partial M_l^\dagger} [\langle\Psi|\hat{\mathcal{H}}|\Psi\rangle - \lambda\langle\Psi|\Psi\rangle] = 0 \quad (\text{A.29})$$

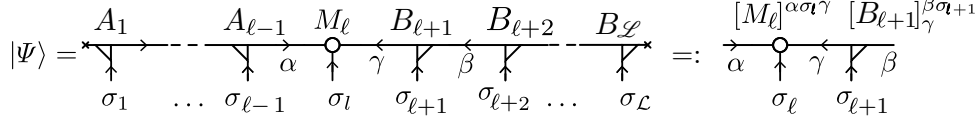


Figure A.21: The diagrammatic representation of MPS for two-site DMRG Eq. (A.28).

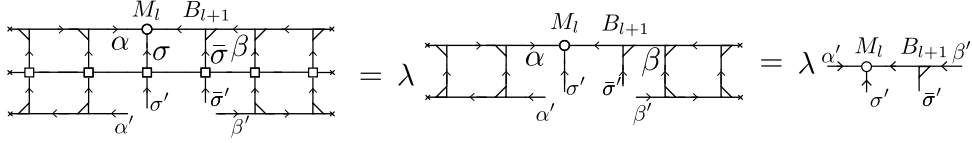


Figure A.22: The diagrammatic representation of Langrangian equation Eq. (A.29).

Here we have 2-site Schrödinger equation

$$[H_l^{(2)}]_a^{a'} [\psi_l^{(2)}]^a = \lambda [\psi_l^{(2)}]^{a'} \quad (\text{A.30})$$

where $a = (\alpha, \sigma, \bar{\sigma}, \beta)$, $\psi_l^{(2)} = M_l B_{l+1}$.

$$[H_l^{(2)}]_a^{a'} = \begin{array}{c} \alpha \quad \sigma \quad \bar{\sigma} \quad \beta \\ \begin{array}{cccc} \times & \times & \times & \times \\ \times & \times & \times & \times \\ \times & \times & \times & \times \\ \times & \times & \times & \times \end{array} \\ \alpha' \quad \sigma' \quad \bar{\sigma}' \quad \beta' \end{array} = \left(\begin{array}{ccc} \alpha & \sigma & \bar{\sigma} \\ \alpha' & \sigma' & \bar{\sigma}' \\ & \beta & \beta' \end{array} \right)$$

Figure A.23: The diagrammatic representation of two-site Hamiltonian Eq. (A.30).

Once again, we solve equation Eq. (A.30) to obtain the eigenstate $\tilde{\psi}_l^{(2)}$. By performing a SVD on it ($\tilde{\psi}_l^{(2)} = USV^\dagger$), we update $M_l \rightarrow A_l = U$ and $B_{l+1} \rightarrow M_{l+1} = SV^\dagger$. This effectively shifts the orthogonality center to the next site.

Subsequently, the process depicted in Fig. A.20 is reiterated to continue the optimization. At this stage, the diagonal matrix S consists of $D \times d$ singular values, which is notably larger than the virtual bond dimension D of M_l and B_{l+1} . This expansion explores a broader state space, encompassing more symmetry sectors. However, this expanded matrix can still be truncated down to D to exclude less relevant states.

Appendix 2: Shrewd Selection

Orthonormality The orthonormality and completeness properties of both the kept and discarded states:

$$A_l^\dagger A_l = \begin{array}{c} A_l \\ \text{---} \\ \text{---} \\ A_l^\dagger \end{array} = \left(= \mathbb{I}_l^K, B_l B_l^\dagger = \begin{array}{c} B_l \\ \text{---} \\ \text{---} \\ B_l^\dagger \end{array} = \right) = \mathbb{I}_{l-1}^K$$

$$\begin{array}{c} \text{---} \\ \text{---} \\ \text{---} \\ \text{---} \end{array} = \left(= \mathbb{I}_l^D, \begin{array}{c} \text{---} \\ \text{---} \\ \text{---} \\ \text{---} \end{array} = 0, \begin{array}{c} \text{---} \\ \text{---} \\ \text{---} \\ \text{---} \end{array} = \right) = \mathbb{I}_{l-1}^D, \begin{array}{c} \text{---} \\ \text{---} \\ \text{---} \\ \text{---} \end{array} = 0$$

$$\begin{array}{c} \text{---} \\ \text{---} \\ \text{---} \\ \text{---} \end{array} + \begin{array}{c} \text{---} \\ \text{---} \\ \text{---} \\ \text{---} \end{array} = \text{---} \Big|_l = \mathbb{I}_l^P, \quad \begin{array}{c} \text{---} \\ \text{---} \\ \text{---} \\ \text{---} \end{array} + \begin{array}{c} \text{---} \\ \text{---} \\ \text{---} \\ \text{---} \end{array} = \text{---} \Big|_l = \mathbb{I}_{l-1}^P$$

Figure B.1: The diagrammatic representation of the orthonormality and completeness of kept and discarded states. Taken from Ref. [61]

The ultimate objective of the shrewd selection process is to obtain \tilde{A}_l^{tr} , which represents the truncated complement. This result is derived from the orthogonal complement A_l . To achieve this goal, three essential cost functions are introduced: \mathcal{C}_1 , \mathcal{C}_2 , and \mathcal{C}_3 .

The core concept revolves around expanding the kept dimension of the one-site isometry A_l from D to $D + \tilde{D}$, where $\tilde{D} < D$ represents the image dimension. This expansion is achieved by appropriately truncating the full complement \bar{A}_l ($\tilde{D} = D(d-1)$).

The purpose is to minimize \mathcal{C}_1 . While SVD can lead to optimal truncation, it comes with the computational cost of two-site DMRG, i.e., $\mathcal{O}(\tilde{D}^3) = D^3(d-1)^3 \sim D^3 d^3$. However, a more cost-effective and efficient approach can be employed, involving two steps:

$$\begin{aligned}
 \mathcal{C}_1 &= \left\| \begin{array}{c} \text{Diagram 1} \\ \text{Diagram 2} \end{array} \right\| \\
 \mathcal{C}_2 &= \left\| \begin{array}{c} \text{Diagram 3} \\ \text{Diagram 4} \end{array} \right\| \\
 \mathcal{C}_3 &= \left\| \begin{array}{c} \text{Diagram 5} \\ \text{Diagram 6} \end{array} \right\|
 \end{aligned}$$

Figure B.2: The cost funtions of shrewd selection. Taken from Ref. [61]

(i) Preselection: Commence with \bar{A}_l and truncate it to minimize the cost function \mathcal{C}_2 . This yields \hat{A}_l^{pr} , termed the preselected complement, with a dimension of $\hat{D} = D$.

(ii) Final selection: Further truncate \hat{A}_l^{pr} to achieve the final result \tilde{A}_l^{tr} with $\tilde{D} < D$. This truncation aims to minimize the cost function \mathcal{C}_3 .

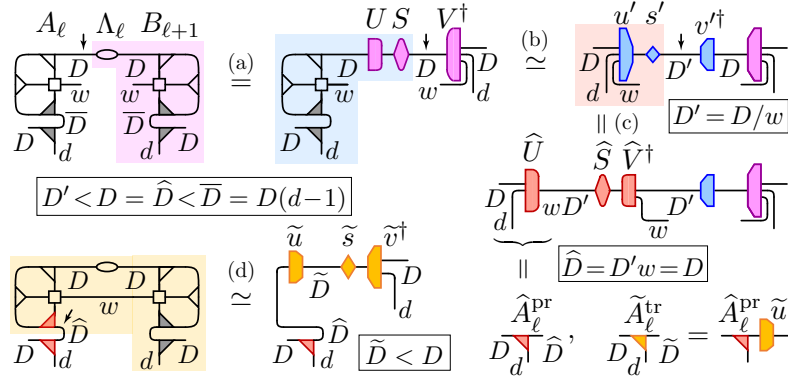


Figure B.3: The shrewd selection process : Steps (a) to (c) are the Preselection, and step (d) is the Final selection. Taken from Ref. [61]

We will now delve into the specifics of step (i) and (ii).

In this phase, the initial truncation reduces the central MPS bond from D to D' within its environment, aiming to minimize the cost function \mathcal{C}_2 . This

truncation leads to a reduced bond dimension of \bar{D} , resulting in $\hat{D} = D'w$ for the preselected complement \hat{A}_l^{pr} . As illustrated in Fig. B.3, prior to step (a), we first cut the MPO bond to alleviate numerical costs. This action divides the diagram into two distinct parts: the Left tensor (L) without Λ_l , and the Right tensor (R) including Λ_l .

(a) The initial SVD process serves to canonicalize the Right section of the diagram, redistributing its weights onto the central MPS bond. This transformation restructures the diagram as $LR \rightarrow (LUS)V^\dagger$, with the resulting V^\dagger tensor having dimensions of $D \times Ddw$.

(b) Subsequently, a second SVD operation is applied to the LUS tensor, implementing truncation to reduce the dimension of this bond. This process yields the transformation $LUS \rightarrow (u's')v^\dagger$, where v^\dagger has dimensions of $D' \times D$, with $D' = D/w$.

(c) The third SVD step involves a reorganization of indices, effectively combining the truncated MPS bond and the MPO bond to form a composite bond of modified dimensions. This step is represented by the operation $u's' \rightarrow \hat{U}\hat{S}\hat{V}^\dagger$, resulting in the total tensor $u's'$ acting as a tensor with dimensions $Dd \times D'w$. Consequently, this produces the preselected complement $\hat{A}_l^{pr} = \hat{U}$.

As we progress through steps (a), (b), and (c), the tensors V^\dagger , v^\dagger , and \hat{V}^\dagger function akin to filters, effectively sieving out the pertinent states that are of interest. In this process, the bond dimension undergoes a series of changes: from Ddw to D , then to $D' = D/w$, and finally stabilizing at $\hat{D} = D = D'w$. This sequence of transformations ensures that only the relevant states are retained.

(d) The fourth SVD, accompanied by truncation, culminates in the production of the final truncated complement, denoted as $\tilde{A}_l^{tr} = \hat{A}_l^{pr}\tilde{u}$. This step leads to a reduction in the bond dimension, transitioning from \hat{D} to \tilde{D} , where \tilde{D} is a value smaller than D .

Appendix 3: Extrapolations and Error Analysis

Extrapolation is a crucial technique in DMRG because it enables the accurate estimation of physical properties without the need to simulate exceedingly large systems or employ prohibitively high bond dimensions, which can be computationally expensive. Various extrapolation methods, including linear, quadratic, or more sophisticated fits, are employed depending on the specific characteristics of the data.

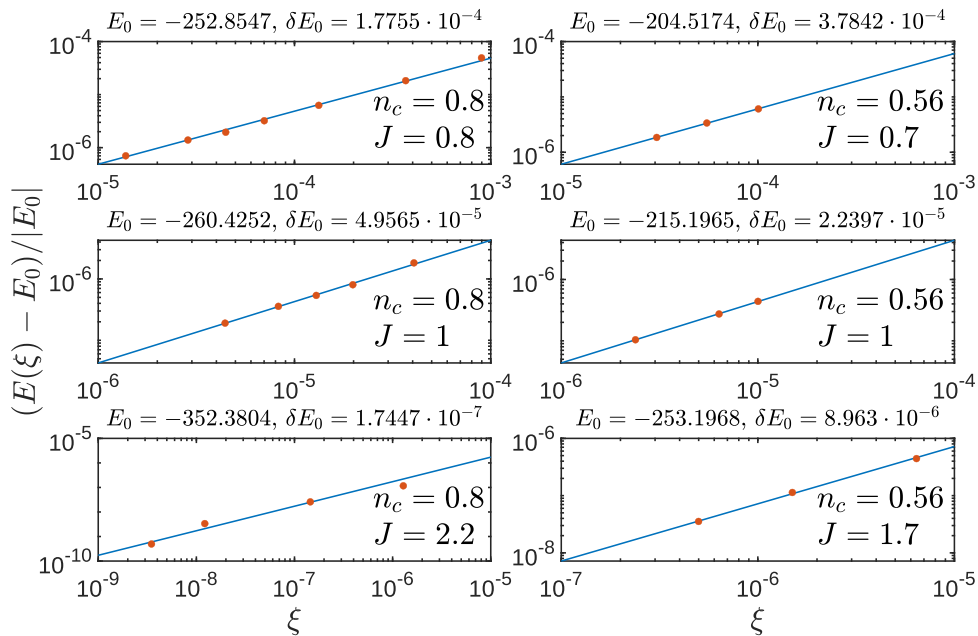


Figure C.1: Error in $|PM\rangle$ state energy vs. discarded weight ξ for $n_c = 0.8$ (left) and $n_c = 0.56$ (right), $N = 200$.

Alongside obtaining extrapolated values, it is equally crucial to assess the associated uncertainty or error in the results. This process often involves a thorough analysis of data convergence and may require the application of statistical methods to provide a reliable estimate of the uncertainties.

Extrapolations of λ

As discussed in Sec. 4.1, the finite size of the system introduces an exponential decay into the correlations. As the bond dimension D increases, the discarded weight ξ since because the MPS includes more states. The reciprocal of the correlation length $1/\lambda$ should approach 0 in a gapless system. Conversely, if $1/\lambda$ does not reach 0 eventually, it suggests the presence of energy gaps in the system.

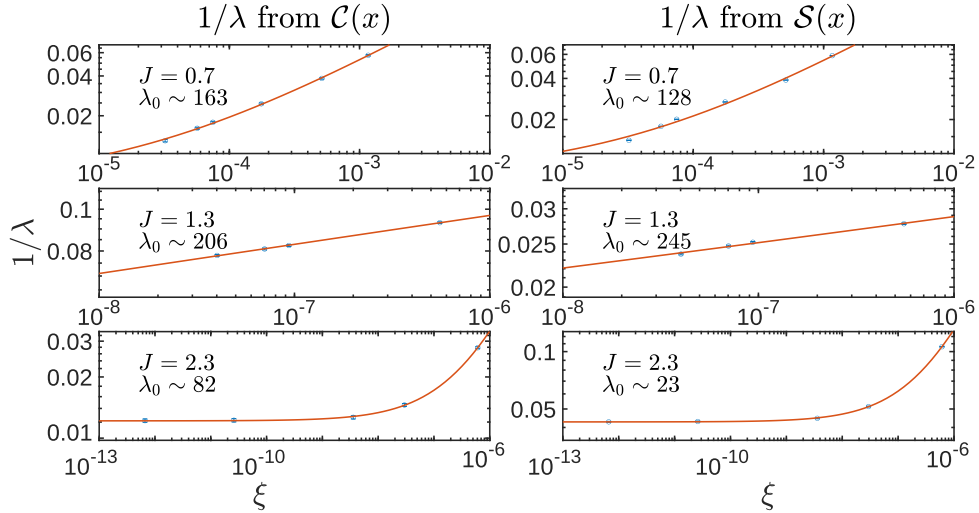


Figure C.2: The extrapolation of $\lambda - \xi$ is depicted here, derived from the curve-fitting of $\mathcal{C}(x)$ (left) and $\mathcal{S}(x)$ (right), $n_c = 0.8$. This extrapolation employs a general model of the form $y = ax^b + c$, where a , b , and c are constants. Here, we set c as λ_0 . In the case of $J = 1.3$ (middle), λ_0 surpasses the system size N , indicating that in this parameter regime, the system is gapless. However, for $J = 0.7$ (top) and $J = 2.3$ (bottom), λ_0 is less than N , suggesting a potential energy gap in these scenarios. Such energy gaps can be further checked by increasing the system size, calculate the spin/charge excitation energy and see if the $\Delta E - 1/N$ extrapolation goes to 0.

Extrapolations of α, β

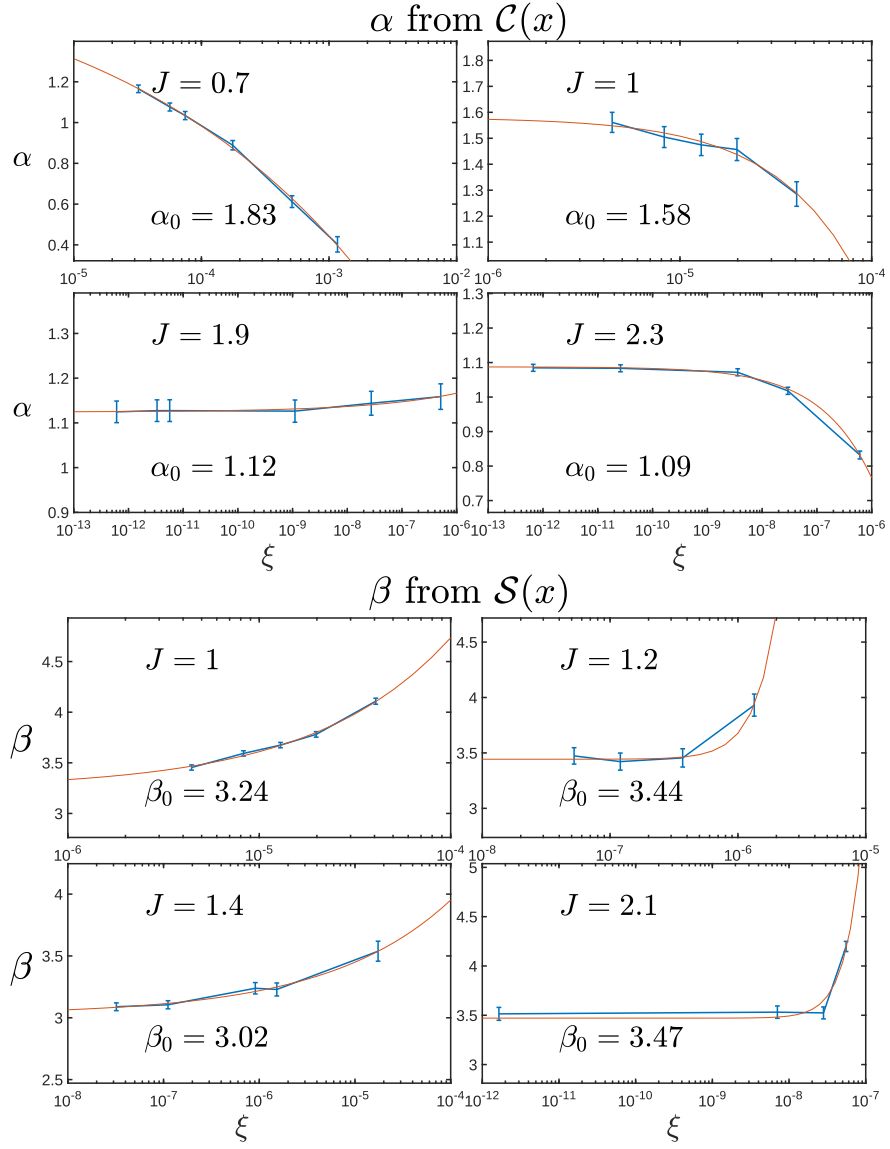


Figure C.4: The extrapolations of $\alpha - \xi$ and $\beta - \xi$, at $n_c = 0.8$. Both of them employ the general model of the form $y = ax^b + c$, here we assign c as α_0 and β_0 .

Bibliography

- [1] J. M. Luttinger, “Fermi surface and some simple equilibrium properties of a system of interacting Fermions”, *Phys. Rev.* **119**, 1153 (1960).
- [2] J. M. Luttinger and J. C. Ward, “Ground-state energy of a Many-Fermion system. ii”, *Phys. Rev.* **118**, 1417 (1960).
- [3] K. B. Blagoev and K. S. Bedell, “Luttinger theorem in one dimensional metals”, *Phys. Rev. Lett.* **79**, 1106 (1997).
- [4] M. Oshikawa, “Topological approach to Luttinger’s theorem and the Fermi surface of a Kondo lattice”, *Phys. Rev. Lett.* **84**, 3370 (2000).
- [5] E. Pivovarov and Q. Si, “Transitions from small to large Fermi momenta in a one-dimensional Kondo lattice model”, *Phys. Rev. B* **69**, 115104 (2004).
- [6] M. Yamanaka, M. Oshikawa, and I. Affleck, “Nonperturbative approach to Luttinger’s theorem in one dimension”, *Phys. Rev. Lett.* **79**, 1110 (1997).
- [7] S. A. Basylko, P. H. Lundow, and A. Rosengren, “One-dimensional Kondo lattice model studied through numerical diagonalization”, *Phys. Rev. B* **77**, 073103 (2008).
- [8] I. P. McCulloch, A. Juozapavicius, A. Rosengren, and M. Gulacsi, “Localized spin ordering in Kondo lattice models”, *Phys. Rev. B* **65**, 052410 (2002).
- [9] S. Moukouri and L. G. Caron, “Fermi surface of the one-dimensional Kondo-lattice model”, *Phys. Rev. B* **54**, 12212 (1996).
- [10] N. Shibata, A. Tsvelik, and K. Ueda, “One-dimensional Kondo lattice model as a Tomonaga-Luttinger liquid”, *Phys. Rev. B* **56**, 330 (1997).
- [11] N. Shibata, K. Ueda, T. Nishino, and C. Ishii, “Friedel oscillations in the one-dimensional Kondo lattice model”, *Phys. Rev. B* **54**, 13495 (1996).

- [12] J. C. Xavier, E. Novais, and E. Miranda, “Small Fermi surface in the one-dimensional Kondo lattice model”, *Phys. Rev. B* **65**, 214406 (2002).
- [13] P. Coleman, C. Pépin, Q. Si, and R. Ramazashvili, “How do Fermi liquids get heavy and die?”, *Journal of Physics: Condensed Matter* **13**, R723 (2001).
- [14] I. Osborne, T. Paiva, and N. Trivedi, “Broken Luttinger theorem in the two-dimensional Fermi-Hubbard model”, *Phys. Rev. B* **104**, 235122 (2021).
- [15] W. O. Putikka, M. U. Luchini, and R. R. P. Singh, “Violation of Luttinger’s theorem in the two-dimensional t-j model”, *Phys. Rev. Lett.* **81**, 2966 (1998).
- [16] S. Doniach, “The Kondo lattice and weak antiferromagnetism”, *Physica B+C* **91**, 231 (1977).
- [17] J. T. Heath and K. S. Bedell, “Necessary and sufficient conditions for the validity of Luttinger’s theorem”, *New Journal of Physics* **22**, 063011 (2020).
- [18] P. Fulde, “Introduction to the theory of heavy Fermions”, *Journal of Physics F: Metal Physics* **18**, 601 (1988).
- [19] J. Kondo, “Resistance Minimum in Dilute Magnetic Alloys”, *Progress of Theoretical Physics* **32**, 37 (1964).
- [20] N. F. Mott, “Rare-earth compounds with mixed valencies”, *The Philosophical Magazine: A Journal of Theoretical Experimental and Applied Physics* **30**, 403 (1974), eprint: <https://doi.org/10.1080/14786439808206566>.
- [21] K. Yosida, “Bound state due to the s-d exchange interaction”, *Phys. Rev.* **147**, 223 (1966).
- [22] P. W. Anderson, “A poor man’s derivation of scaling laws for the Kondo problem”, *Journal of Physics C: Solid State Physics* **3**, 2436 (1970).
- [23] K. G. Wilson, “The renormalization group: critical phenomena and the Kondo problem”, *Rev. Mod. Phys.* **47**, 773 (1975).
- [24] P. Coleman, “Heavy electrons”, *Introduction to many-body physics* (Cambridge University Press, 2015), pp. 656–719.
- [25] M. A. Ruderman and C. Kittel, “Indirect exchange coupling of nuclear magnetic moments by conduction electrons”, *Phys. Rev.* **96**, 99 (1954).
- [26] S. Doniach, “Phase diagram for the Kondo lattice”, *Valence instabilities and related narrow-band phenomena*, edited by R. D. Parks (Springer US, Boston, MA, 1977), pp. 169–176.
- [27] G. Honner and M. Gulácsi, “Ordering of localized moments in Kondo lattice models”, *Phys. Rev. B* **58**, 2662 (1998).

-
- [28] I. Khait, P. Azaria, C. Hubig, U. Schollwöck, and A. Auerbach, “Doped Kondo chain, a heavy Luttinger liquid”, *Proceedings of the National Academy of Sciences* **115**, 5140 (2018), eprint: <https://www.pnas.org/doi/pdf/10.1073/pnas.1719374115>.
- [29] C. Zener, “Interaction between the d -shells in the transition metals. ii. ferromagnetic compounds of manganese with perovskite structure”, *Phys. Rev.* **82**, 403 (1951).
- [30] P. W. Anderson and H. Hasegawa, “Considerations on double exchange”, *Phys. Rev.* **100**, 675 (1955).
- [31] J. Zang, H. Röder, A. R. Bishop, and S. A. Trugman, “Magnetic properties of the double-exchange model”, *Journal of Physics: Condensed Matter* **9**, L157 (1997).
- [32] M. Sigrist, H. Tsunetsuga, and K. Ueda, “Rigorous results for the one-electron Kondo-lattice model”, *Phys. Rev. Lett.* **67**, 2211 (1991).
- [33] M. Sigrist, H. Tsunetsugu, K. Ueda, and T. M. Rice, “Ferromagnetism in the strong-coupling regime of the one-dimensional Kondo-lattice model”, *Phys. Rev. B* **46**, 13838 (1992).
- [34] H. Tsunetsugu, M. Sigrist, and K. Ueda, “The ground-state phase diagram of the one-dimensional Kondo lattice model”, *Rev. Mod. Phys.* **69**, 809 (1997).
- [35] A. M. Tsvelik and O. M. Yevtushenko, “Transport in magnetically doped one-dimensional wires: can the helical protection emerge without the global helicity?”, *New Journal of Physics* **22**, 053013 (2020).
- [36] A. M. Tsvelik and O. M. Yevtushenko, “Physics of arbitrarily doped kondo lattices: from a commensurate insulator to a heavy luttinger liquid and a protected helical metal”, *Phys. Rev. B* **100**, 165110 (2019).
- [37] M. Troyer and D. Würtz, “Ferromagnetism of the one-dimensional Kondo-lattice model: a quantum Monte Carlo study”, *Phys. Rev. B* **47**, 2886 (1993).
- [38] H. Tsunetsugu, M. Sigrist, and K. Ueda, “Phase diagram of the one-dimensional Kondo-lattice model”, *Phys. Rev. B* **47**, 8345 (1993).
- [39] S. Caprara and A. Rosengren, “Ground-state magnetic properties of the Kondo lattice model at low electron densities”, *Europhysics Letters* **39**, 55 (1997).
- [40] S. Moukouri and L. G. Caron, “Ground-state properties of the one-dimensional Kondo lattice at partial band filling”, *Phys. Rev. B* **52**, R15723 (1995).
- [41] Y. Huang, D. N. Sheng, and C. S. Ting, “Charge density wave in a doped Kondo chain”, *Phys. Rev. B* **99**, 195109 (2019).

- [42] R. Peters and N. Kawakami, “Ferromagnetic state in the one-dimensional Kondo lattice model”, *Phys. Rev. B* **86**, 165107 (2012).
- [43] J. R. Schrieffer and P. A. Wolff, “Relation between the anderson and Kondo hamiltonians”, *Phys. Rev.* **149**, 491 (1966).
- [44] P. Sinjukow and W. Nolting, “Exact mapping of periodic anderson model to kondo lattice model”, *Phys. Rev. B* **65**, 212303 (2002).
- [45] R. M. Martin, “Fermi-surface sum rule and its consequences for periodic Kondo and mixed-valence systems”, *Phys. Rev. Lett.* **48**, 362 (1982).
- [46] M. Cyrot, “Theory of Mott transition: applications to transition metal oxides”, *Journal de Physique* **33**, 125 (1972).
- [47] D. J. Scalapino, E. Loh, and J. E. Hirsch, “Fermi-surface instabilities and superconducting d-wave pairing”, *Phys. Rev. B* **35**, 6694 (1987).
- [48] M. D. Johannes and I. I. Mazin, “Fermi surface nesting and the origin of charge density waves in metals”, *Phys. Rev. B* **77**, 165135 (2008).
- [49] S. Sachdev, E. Berg, S. Chatterjee, and Y. Schattner, “Spin density wave order, topological order, and fermi surface reconstruction”, *Phys. Rev. B* **94**, 115147 (2016).
- [50] S. Friedemann, T. Westerkamp, M. Brando, N. Oeschler, S. Wirth, P. Gegenwart, C. Krellner, C. Geibel, and F. Steglich, “Detaching the anti-ferromagnetic quantum critical point from the Fermi-surface reconstruction in YbRh₂Si₂”, *Nature Physics*, v.5, 465-469 (2009) **5**, 10.1038/nphys1299 (2009).
- [51] O. Stockert and F. Steglich, “Unconventional quantum criticality in heavy-Fermion compounds”, *Annual Review of Condensed Matter Physics* **2**, 79 (2011), eprint: <https://doi.org/10.1146/annurev-conmatphys-062910-140546>.
- [52] R. Peters and N. Kawakami, “Large and small fermi-surface spin density waves in the kondo lattice model”, *Phys. Rev. B* **92**, 075103 (2015).
- [53] A. E. Sikkema, I. Affleck, and S. R. White, “Spin gap in a doped kondo chain”, *Phys. Rev. Lett.* **79**, 929 (1997).
- [54] E. Lieb, T. Schultz, and D. Mattis, “Two soluble models of an antiferromagnetic chain”, *Annals of Physics* **16**, 407 (1961).
- [55] A. Nikolaenko and Y.-H. Zhang, “Numerical signatures of ultra-local criticality in a one dimensional Kondo lattice model”, <https://doi.org/10.48550/arXiv.2306.09402>.
- [56] S. R. White, “Density matrix formulation for quantum renormalization groups”, *Phys. Rev. Lett.* **69**, 2863 (1992).
- [57] S. R. White, “Density-matrix algorithms for quantum renormalization groups”, *Phys. Rev. B* **48**, 10345 (1993).

-
- [58] K. A. Hallberg, “Density-matrix algorithm for the calculation of dynamical properties of low-dimensional systems”, *Phys. Rev. B* **52**, R9827 (1995).
- [59] X. Wang and T. Xiang, “Transfer-matrix density-matrix renormalization-group theory for thermodynamics of one-dimensional quantum systems”, *Phys. Rev. B* **56**, 5061 (1997).
- [60] G. Vidal, “Efficient classical simulation of slightly entangled quantum computations”, *Phys. Rev. Lett.* **91**, 147902 (2003).
- [61] A. Gleis, J.-W. Li, and J. von Delft, “Controlled bond expansion for density matrix renormalization group ground state search at single-site costs”, *Phys. Rev. Lett.* **130**, 246402 (2023).
- [62] B. Derrida, M. R. Evans, V. Hakim, and V. Pasquier, “Exact solution of a 1d asymmetric exclusion model using a matrix formulation”, *Journal of Physics A: Mathematical and General* **26**, 1493 (1993).
- [63] U. Schollwöck, “The density-matrix renormalization group in the age of matrix product states”, *Annals of Physics* **326**, January 2011 Special Issue, 96 (2011).
- [64] F. Verstraete, V. Murg, and J. Cirac, “Matrix product states, projected entangled pair states, and variational renormalization group methods for quantum spin systems”, *Advances in Physics* **57**, 143 (2008), eprint: <https://doi.org/10.1080/14789940801912366>.
- [65] J. von Delft, *"tensor network" lecture notes*, 2023.
- [66] I. P. McCulloch, “From density-matrix renormalization group to matrix product states”, *Journal of Statistical Mechanics: Theory and Experiment* **2007**, P10014 (2007).
- [67] A. Weichselbaum, “Non-abelian symmetries in tensor networks: a quantum symmetry space approach”, *Annals of Physics* **327**, 2972 (2012).
- [68] E. Koch, “The Lanczos method”, *The lda+dmft approach to strongly correlated materials, forschungszentrum jülich*, edited by E. Pavarini, E. Koch, D. Vollhardt, and A. Lichtenstein (2011).
- [69] C. Lanczos, “An iteration method for the solution of the eigenvalue problem of linear differential and integral operators”, *Journal of research of the National Bureau of Standards* **45**, 255 (1950).
- [70] I. Ojalvo and M. Newman, “Vibration modes of large structures by an automatic matrix-reduction method”, *Aiaa Journal - AIAA J* **8**, 1234 (1970).
- [71] C. Paige, “Computational variants of the Lanczos method for the eigenproblem”, *J. Inst. Maths Applies* **10**, 373 (1972).
- [72] I. McCulloch, “Infinite size density matrix renormalization group, revisited”, <https://doi.org/10.48550/arXiv.0804.2509> (2008).

- [73] H. Ueda, T. Nishino, and K. Kusakabe, “Two-site shift product wave function renormalization group method applied to quantum systems”, *Journal of the Physical Society of Japan* **77**, 114002 (2008), eprint: <https://doi.org/10.1143/JPSJ.77.114002>.
- [74] S. R. White, “Density matrix renormalization group algorithms with a single center site”, *Phys. Rev. B* **72**, 180403 (2005).
- [75] C. Hubig, I. P. McCulloch, U. Schollwöck, and F. A. Wolf, “Strictly single-site DMRG algorithm with subspace expansion”, *Phys. Rev. B* **91**, 155115 (2015).
- [76] A. Gleis, J.-W. Li, and J. von Delft, “Projector formalism for kept and discarded spaces of matrix product states”, *Phys. Rev. B* **106**, 195138 (2022).
- [77] S. R. White, I. Affleck, and D. J. Scalapino, “Friedel oscillations and charge density waves in chains and ladders”, *Phys. Rev. B* **65**, 165122 (2002).
- [78] T. Giamarchi and H. J. Schulz, “Correlation functions of one-dimensional quantum systems”, *Phys. Rev. B* **39**, 4620 (1989).
- [79] M. Gulacsi, A. Bussmann-Holder, and A. R. Bishop, “Spin and lattice effects in the Kondo lattice model”, *Phys. Rev. B* **71**, 214415 (2005).
- [80] V. Zauner-Stauber, L. Vanderstraeten, M. T. Fishman, F. Verstraete, and J. Haegeman, “Variational optimization algorithms for uniform matrix product states”, *Phys. Rev. B* **97**, 045145 (2018).
- [81] J. I. Cirac, D. Pérez-García, N. Schuch, and F. Verstraete, “Matrix product states and projected entangled pair states: concepts, symmetries, theorems”, *Rev. Mod. Phys.* **93**, 045003 (2021).
- [82] J. Eisert, M. Cramer, and M. B. Plenio, “Colloquium: area laws for the entanglement entropy”, *Rev. Mod. Phys.* **82**, 277 (2010).
- [83] M. B. Hastings, “An area law for one-dimensional quantum systems”, *Journal of Statistical Mechanics: Theory and Experiment* **2007**, P08024 (2007).

Selbständigkeitserklärung

Hiermit erkläre ich, die vorliegende Arbeit selbständig verfasst und keine anderen als die angegebenen Quellen und Hilfsmittel benutzt zu haben.

München, 15. September 2023

Ming Huang
